

UNIVERSITY OF SILESIA IN KATOWICE
AUGUST CHEŁKOWSKI INSTITUTE OF PHYSICS

Tomasz Sobol

**Effect of transition metal cap layer on the electronic structure of
topological insulator Bi_2Te_3**

Supervisor: dr hab. Jerzy Michał Kubacki

Assistant supervisor: dr Katarzyna Balin

Chorzów 2024

Outline

Chapter 1 Introduction	1
1.1 Brief overview and significance of Topological Insulators	1
1.2 Key considerations and experimental findings.....	2
1.3 Scope and Objectives of the Thesis	4
Chapter 2 Theoretical and experimental aspects of topological insulators	5
2.1 Symmetry and topology.....	5
2.2 Topological Insulators theory	6
2.2.1 Band theory and insulating state	6
2.2.2 Integer Quantum Hall effect and Topological Insulators.....	7
2.2.3 Surface and edge states	9
2.3 Overview of Experimental Studies on Topological Insulators	12
2.3.1 Experimental realization of 2D and 3D Topological Insulators.....	12
2.3.2 Bandgap semiconductors of heavy elements	14
2.3.3 Crystal and electronic structure of Bismuth Telluride	15
2.3.4 Doped Bi ₂ Te ₃	18
Chapter 3 Experimental details	22
3.1 Thin films growth and structural characterization.....	22
3.1.1 Molecular Beam Epitaxy	22
3.1.2 Interface formation.....	24
3.1.3 Structural characterization by Low Energy Electron Diffraction	27
3.2 Photoemission Spectroscopy	29
3.2.1 Photoemission background	29
3.2.2 Angle Resolved Photoemission Spectroscopy	32
3.2.3 X-ray Absorption Spectroscopy	37
3.2.4 Circular Dichroism – ARPES	40
3.3 Experimental setup and Methodology	43

3.3.1 Radiation sources	43
3.3.2 Synchrotron radiation.....	43
3.3.3 Beamlines.....	45
3.3.4 PHELIX and URANOS beamlines	47
3.3.5 Sample description and preparation process	48
Chapter 4 Results and Discussion.....	50
4.1 Pristine Bi ₂ Te ₃	50
4.1.1 XPS studies	51
4.1.2 ARPES studies	59
4.1.3 CD-ARPES studies and OAM	67
4.2 Bi ₂ Te ₃ /Fe system.....	70
4.2.1 XPS studies	72
4.2.2 ARPES and CD-ARPES studies	83
4.3 Bi ₂ Te ₃ /Co system	93
4.3.1 XPS studies	93
4.3.2 ARPES and CD-ARPES studies	97
Chapter 5 Summary and perspectives.....	101
5.1 Summary.....	101
5.2 Perspectives	102
Appendix	104
List of figures	105
Bibliography	111

Podziękowania

Na pierwszym miejscu pragnę podziękować moim rodzicom oraz rodzeństwu, którzy przez cały okres moich studiów i pracy nieustannie wspierali mnie w dążeniu do upragnionego celu.

Chciałbym w szczególności podziękować Jerzemu Kubackiemu i Kasi Balin za cierpliwość i za wyrozumiałość oraz wielkie wsparcie i pomoc jakim mnie obdarzyli w trakcie trwania mojego doktoratu. Bardzo dziękuję!

Chciałbym również podziękować wszystkim pracownikom synchrotronu SOLARIS, dzięki którym codzienna praca naukowa (nie tylko) stała się czystą przyjemnością.

Specjalne podziękowania dla mojej dziewczyny Liwii, dzięki której znalazłem motywację oraz siłę na dokończenie tej pracy.

Na zakończenie pragnę wyrazić moją głęboką wdzięczność i szacunek dla śp. profesora Jacka Szade, który wprowadził mnie do projektu SOLARIS i umożliwił mi udział w tym niezwykłym przedsięwzięciu. Chciałbym, aby mógł zobaczyć, jak wspaniale rozwija się ten projekt.

Abstract

Topological insulators have been among the most intensively studied group of materials in condensed matter physics over the past twenty years. They contain theoretically predicted new quantum states of matter, characterized by unique properties that lead to the formation of metallic surface states, a key feature of these materials. The exceptional electronic structure of these materials and their potential applications in various fields have attracted the attention of numerous research groups.

The aim of this doctoral dissertation was to determine the impact of an ultra-thin layer of transition metals, iron, and cobalt, on the electronic structure of the surface states of Bi_2Te_3 . The study also explains changes in the core states of this material during the formation of an interface with the deposited transition metals. Using research techniques such as angle-resolved photoemission spectroscopy (ARPES), photoelectron spectroscopy (PES), X-ray absorption spectroscopy (XAS), and circular dichroism-ARPES (CD-ARPES) that utilize synchrotron radiation, the physicochemical structure of the created transition metal-topological insulator interface/junction was determined. ARPES and CD-ARPES studies were also conducted to illustrate the dispersion dependence of the surface states and the top of the valence band before and after the deposition of the iron and cobalt layers, as well as to determine the impact of the deposited structures on the possibility of opening an energy gap (band gap).

The results obtained through angle-resolved photoemission spectroscopy revealed band bending phenomena and the lifting of the degeneracy of the states at the top of the valence band and the bottom of the conduction band. Additionally, photoelectron spectroscopy provided information about the formation of additional phases, such as metallic Bi and compounds like FeTe and CoTe during the deposition of transition metals. Using X-ray absorption spectroscopy and circular dichroism techniques, the magnetic properties at the transition metal-topological insulator boundary were determined.

The dissertation also provides a detailed discussion of the technique of synchrotron radiation generation.

Streszczenie

Izolatory topologiczne stanowią jedno z najbardziej intensywnie badanych materiałów w fizyce materii skondensowanej w ostatnich dwudziestu latach. Zawierają one przewidziane teoretycznie nowe kwantowe stany materii, charakteryzujące się unikalnymi właściwościami prowadzącymi do powstawania metalicznych stanów powierzchniowych, stanowiących kluczową cechę tych materiałów. Wyjątkowa struktura elektronowa tych materiałów oraz ich potencjalne możliwości wykorzystania w różnych dziedzinach, przyciągnęły uwagę licznych grup badawczych.

Celem pracy doktorskiej było określenie wpływu ultra cienkiej warstwy metali przejściowych, żelaza oraz kobaltu, na strukturę elektronową stanów powierzchniowych Bi_2Te_3 . W pracy przedstawiono także wyjaśnienie zmian stanów rdzeniowych tego materiału podczas tworzenia interfejsu z naniesionymi metalami przejściowymi. Przy użyciu technik badawczych, takich jak kątowno rozdzielcza spektroskopia fotoemisyjna ARPES, spektroskopia fotoelektronów PES, spektroskopia absorpcji rentgenowskiej XAS oraz dichroizmu kołowego w ARPES, CD-ARPES, wykorzystujących promieniowanie synchrotronowe, określona została struktura fizykochemiczna utworzonego interfejsu/złącza metal przejściowy - izolator topologiczny. Przeprowadzone zostały także badania ARPES oraz CD-ARPES, dzięki którym zobrazowano zależność dyspersyjną stanów powierzchniowych oraz szczytu pasma walencyjnego przed i po osadzeniu warstwy żelaza oraz kobaltu, oraz określono wpływ naniesionych struktur na możliwość otwarcia przerwy energetycznej (szczeliny pasmowej).

Wyniki uzyskane dzięki kątowno rozdzielczej spektroskopii fotoemisyjnej, wykazały zjawiska zakrzywienia pasm oraz zniesienia degeneracji stanów szczytu pasma walencyjnego oraz dna pasma przewodnictwa. Dodatkowo, spektroskopia fotoelektronów dostarczyła informacji o formowaniu dodatkowych faz, takich jak metaliczny Bi oraz związków FeTe i CoTe w trakcie depozycji metali przejściowych. Przy zastosowaniu technik spektroskopii absorpcji rentgenowskiej oraz dichroizmu kołowego określone zostały właściwości magnetyczne na granicy metal przejściowy - izolator topologiczny.

W dysertacji szczegółowo omówiona została także technika wytwarzania promieniowania synchrotronowego.

Chapter 1 Introduction

This chapter provides a comprehensive introduction to topological insulators, presenting an overview of their fundamental properties and significance in condensed matter physics. It discusses key experimental findings in the field, with a focus on the challenges and considerations involved in combining topological insulators with magnetism, laying the groundwork for understanding magnetic topological insulators and their potential applications.

1.1 Brief overview and significance of Topological Insulators

Three-dimensional (3D) Topological Insulators (TIs), a new class of condensed matter, are characterized by a unique electronic band structure that features metallic Dirac surface states generated by spin-orbit coupling. These surface states exist within the valence and conduction band gaps alongside insulating bulk states. Protected by time-reversal symmetry, these surface states exhibit exciting properties such as spin-momentum locking and linear dispersion. Since their inception, TIs have been regarded as highly promising materials for spin-electronic and magneto-electronic applications, leading to significant scientific interest in studying and understanding how to modify the electronic structure of these materials.

To fully exploit the potential of TIs in spintronic or nanoelectronic devices, it is crucial to understand how magnetic modifications of the TI surface will impact the electronic structure. Introducing an external magnetic field to TIs can break time-reversal symmetry, potentially leading to gap opening at the Dirac point of the helical states and altering the spin texture, thereby giving rise to various physical phenomena usable in spintronics applications. One straightforward method to induce magnetic order in TIs is by incorporating magnetic atoms (e.g., transition metals) into the TI matrix. The alignment of the s and p orbitals of TI bands, contributing to metallic surface states, with the d and f orbitals of transition metals through exchange coupling interactions, makes these elements ideal candidates for introducing magnetic order into the system.

Moreover, besides achieving gap opening, another crucial consideration is the chemical potential. Ideally, the chemical potential (Fermi level) should be positioned in the middle of the gap. Tuning the Fermi level can be achieved by n- or p-doping the TI with elements that do not necessarily exhibit magnetic properties. The understanding and realization of the gap opening process are essential for achieving many unique quantum effects such as the quantum

anomalous Hall effect, axion insulators, or chiral Majorana modes. The concept and theoretical framework of TIs and the influence of magnetic fields will be further discussed in Chapter 2.

1.2 Key considerations and experimental findings

In the field of magnetic topological insulators (MTIs), several unresolved problems, crucial for advancing both fundamental understanding and practical applications, are open. These challenges primarily concern the technical aspects of material synthesis, the intrinsic properties and phenomena associated with MTIs, and the development of precise characterization techniques necessary for probing their complex electronic and magnetic behaviors. Achieving stable and well-controlled magnetic ordering in MTIs remains a key challenge, along with determining the fundamental conditions necessary for the observation of topological insulator-related phenomena. The exact nature of the topological surface states, particularly in the presence of magnetic ordering, is still not fully understood. Precise engineering of the electronic band structure in MTIs to achieve desired properties continues to be a focus of research. Additionally, understanding the interaction between spin-orbit coupling and magnetic moments is crucial for predicting and controlling MTI properties. The relationship between magnetic doping or intrinsic magnetism and the stability of the topological phase, as well as the occurrence of TI-related phenomena, also demands further exploration. The effects of disorder and defects on the realization of the quantum anomalous Hall effect (QAHE) in MTIs remain unclear, as the underlying mechanisms are not yet fully understood. Finally, more effective experimental methods for characterizing MTIs are needed to overcome the limitations of current techniques, which often struggle to resolve fine details.

Recent studies have identified two promising approaches to combine magnetism with TIs: the magnetic proximity effect and magnetic doping. Alternating stacking of TIs with ferro/antiferromagnetic materials offers a versatile method to create TI-based magnetic heterostructures and superlattices. However, realizing structures such as magnetic topological insulators is nontrivial and requires meeting several conditions. The magnetic film must possess long-range ferromagnetic properties that survive stacking with the insulator, and a perpendicular easy magnetization axis is also necessary. Additionally, precise control over the film thickness is crucial to achieve the predicted band gap while maintaining metallic surface states, ensuring it does not exceed the ferromagnetic exchange energy. Finally, the chemical potential must be tuned to match the magnetic gap of the surface states.

Fabrication of well-defined structures is challenging but achievable using techniques such as Molecular Beam Epitaxy (MBE). Magnetic doping of TIs can be realized through various methods, with the most popular and successful approaches involving the use of MBE setups. This method enables precise control over parameters such as film thickness and element stoichiometry, crucial for the electronic band structure. One approach to magnetic doping is to introduce magnetic impurities at the surface of 3D TIs. This method offers the opportunity to grow very thin "layers" on the material's surface, creating an interface at the top that will alter the electronic structure of the substrate. During the growth of the interface, various physical and chemical processes may occur, such as downward or upward band bending (via n- or p-doping), chemical reactions at the surface, or element substitution, all of which will influence the electronic band structure of TIs.

To form a TI, strong spin-orbit coupling is required to sufficiently modify the electronic band structure. Materials with such properties needed to be identified. While spin-orbit coupling strengthens with heavier elements, it alone is not enough for realizing TIs. The energy band gap must not exceed the energy of the spin-orbit coupling, as the coupling will not be able to alter the phase of the valence and conduction bands. Semiconductors with narrow band gaps made of heavy elements, such as the Sb_2Te_3 , Bi_2Se_3 , and Bi_2Te_3 materials, were found to exhibit topological insulator behavior. Bi_2Se_3 and Bi_2Te_3 are of particular interest due to their relatively simple band structures and the simplest surface states allowed. The combination of a large bulk band gap of up to more than 0.2 eV with simple surface states opens up possibilities for various experiments involving electronic band structure modification and engineering.

In Chapter 2, I will present detailed literature review of 3D TIs, especially Bi_2Te_3 , and recent progress in the field. To track and study changes in the electronic band structure of TIs, sophisticated techniques are required to map surface bands. Popular methods include Angle Resolved Photoelectron Spectroscopy (ARPES), Spin-ARPES, and Scanning Transmission Microscopy (STM). ARPES allows scientists to measure the dispersion relation of electrons in the material with very high spatial and energy resolution, which can be as high as 1.5 meV. However, sample preparation for ARPES is challenging due to the requirement for samples with well-defined crystal structures. Synchrotron radiation (SR) offers significant advantages for studying TIs, including tunable excitation energy and polarization of the light, which provide alternative ways to study electronic structure and magnetic properties. In Chapter 3, I will provide a brief overview of SR generation theory, its advantages, and the challenges associated with probing materials using this type of light.

1.3 Scope and Objectives of the Thesis

The scope of this thesis includes a detailed investigation of the electronic structure and magnetic properties of the three-dimensional topological insulator Bi_2Te_3 , particularly when capped with transition metals such as Fe and Co. The study was conducted using a single crystal of Bi_2Te_3 , fabricated via the MBE method by the external company MaTeck. The surface of the crystal was prepared for electronic structure analysis through mechanical exfoliation. This research primarily aims to elucidate the impact of transition metal deposition on the surface states and overall electronic structure of Bi_2Te_3 . Key experimental techniques employed in this study include ARPES, X-ray Photoemission Spectroscopy (XPS), X-ray Absorption Spectroscopy (XAS), and Circular Dichroism - Angle Resolved Photoemission Spectroscopy (CD-ARPES), all conducted using synchrotron radiation. The scope also extends to analyzing the challenges encountered in forming a clean transition metal interface on Bi_2Te_3 and the resultant phase formations due to chemical interactions. Explanation of the generation process of synchrotron radiation and its influence on the experimental outcomes is also within the scope of this thesis.

The main objectives of my thesis are focused on several aspects:

- First one is focused on investigation of the electronic structure of Bi_2Te_3 , particularly the behavior of its surface states when capped with transition metals like Fe and Co, and to examine potential gap openings or changes in the electronic structure induced by these magnetic layers.
- The next one refers to characterization of the interface between Bi_2Te_3 and transition metals, addressing the challenges posed by chemical reactivity that can lead to the formation of stable phases, including layers of pure elements or intermediate phases between the elements in the examined system.
- Additionally, magnetic properties of the transition metal interface will be explored using techniques like XAS and CD-ARPES.
- Advanced spectroscopic methods, including ARPES and XPS will be employed to probe the band structure and electronic states of the system, with special attention to quantized conductivity bands and valence band behavior.
- Finally, the role of synchrotron radiation in enhancing experimental measurements will be evaluated, to highlight its importance in achieving high-resolution spectroscopic data.

- These objectives aim to provide a detailed understanding of the interplay between topological insulators and transition metals, advancing knowledge in the field of condensed matter physics.

Chapter 2 Theoretical and experimental aspects of topological insulators

This Chapter provides an overview of both the theoretical and experimental aspects of topological insulators. Section 2.1 discusses the fundamental role of symmetry and topology in defining the unique properties of topological insulators. Section 2.2 delves into the theoretical framework, including band theory and the insulating state, the relation between the Integer Quantum Hall Effect and topological insulators, and the nature of surface and edge states. Section 2.3 summarizes key experimental studies, covering the realization of 2D and 3D topological insulators, the role of heavy-element bandgap semiconductors, the crystal and electronic structure of Bismuth Telluride, and the effects of doping in Bi_2Te_3 .

2.1 Symmetry and topology

Symmetry, in mathematics, is the transformation that leaves an object or system unchanged. For example, a sphere exhibits rotational symmetry – you can rotate it, change its orientation, and the sphere remains the same. The fact that objects, systems, or even the entire universe obey symmetries determines that the laws of physics remain the same under certain transformations, and each of these symmetries imposes the conservation of a quantity. Conservation of momentum corresponds to translational symmetry, angular momentum to rotational symmetry, energy to the symmetry of time, and charge to gauge symmetry. This principle is known as Noether's theorem. Understanding symmetries helps simplify the description of nature and can also be used to classify phases of matter. Landau explained that some phases of matter, such as magnets and superconductors, can essentially be understood as systems with spontaneously broken symmetries.



Figure 1 The SOLARIS mug and the Krakow pretzel are topologically indistinguishable because they share the same genus value of 1 (number of holes) and can be smoothly transformed into each other. In

contrast, the German pretzel has a genus value of 3, making it topologically distinct, meaning that neither the mug nor the Krakow pretzel can be smoothly transformed into the German pretzel in a topological sense.

Topology is a powerful branch of mathematics that helps physicists expand the description of matter. Topology describes objects that remain the same under smooth, continuous deformations, for example, a SOLARIS cup transforming into a Krakow pretzel but into the German pretzel! As illustrated in Figure 1, the cup can be smoothly deformed into the Krakow pretzel because they are topologically equivalent. Generally, this means that the cup and the Krakow pretzel have the same number of holes, and this number is called the integer topological invariant or genus g . Recently, topology has played a significant role in distinguishing and classifying materials. Combining symmetry and topology has led to an understanding of certain groups of electronic materials classified as topological phases. The importance of topology in the field of science is highlighted by the fact that the 2016 Nobel Prize in Physics was awarded for the discoveries of topological phase transitions and topological phases of matter¹ (for Thouless, Haldane, and Kosterlitz).

The concept of topological order was developed in the 1980s to understand the quantum Hall effect². Thirty years later, another topological phase was discovered, where a combination of spin-orbit coupling, inversion and time-reversal symmetry led to extraordinary phenomena, with topology playing a key role in their description – these are known as topological insulators.

2.2 Topological Insulators theory

2.2.1 Band theory and insulating state

One of the most significant discoveries in theoretical physics was the description of the solid state in terms of their electrical properties, as understood by Wilson³. He classified crystals into insulating and metallic states based on a theory whose foundations lie in the newly described quantum world - the Band theory⁴. Band theory is one of the earliest theories to emerge from the quantum description of matter and systematizes the description of the electronic properties of solid state, more precisely, the crystalline state. The theory leverages crystal translation symmetry and allows for the expression of every electron in terms of the crystal momentum \mathbf{k} defined in the periodic Brillouin zone. These electron states can be described by wave vectors $|\psi(\mathbf{k})\rangle = e^{i\mathbf{k}\cdot\mathbf{r}}|u(\mathbf{k})\rangle$, where $|u(\mathbf{k})\rangle$ is eigenstate of the Bloch Hamiltonian $H(\mathbf{k})$

$$H(\mathbf{k}) = e^{i\mathbf{k}\cdot\mathbf{r}} H e^{-i\mathbf{k}\cdot\mathbf{r}} \quad 2.1$$

and all of the eigenvalues $E_m(\mathbf{k})$ are defining the electronic band structure.

Based on the band theory, we can describe the state of an insulator. An insulator is the simplest state occurring in solid-state physics. It is characterized by electrons strongly bound to atomic nuclei - in insulators, mainly covalent bonds are present. However, their most significant property is the energy gap that separates the filled valence band from the unfilled conduction band (it's important to note that, according to quantum theory, vacuum is also considered an insulator). The question that arises is whether every insulator state is the same. Surprisingly, the answer is no.

2.2.2 Integer Quantum Hall effect and Topological Insulators

The most popular example in the literature confirming that not every insulator is the same is the integer quantum Hall effect⁵. This phenomenon can be observed when a two-dimensional electron gas (2DEG) interacts with a strong external magnetic field. Electrons moving along circular orbits with a specific cyclotron frequency ω become quantized, leading to Landau level quantization. If we assume that n Landau levels are filled and the rest are unoccupied, we observe an energy gap between these two levels - just like in an insulator. However, in this process, an electric field will be generated, which will cause drift of cyclotron orbits. This drift results in the generation of Hall current, which is described by the quantized Hall conductivity

$$\sigma_{xy} = \frac{ne^2}{h} \quad 2.2$$

However, if we treat the Landau levels as a band structure and assume that this structure can be described within the framework of regions with periodic potential, then the Bloch theory allows for describing these states by \mathbf{k} - which ultimately leads to the dispersion of energy levels with \mathbf{k} . As a result, we obtain a band structure very similar to that of an insulator state. The answer to why the quantum Hall effect is different from the insulator state can be found within the Topology.

The 2D band structure can be described by a \mathbf{k} -dependent Hamiltonian, known as the Bloch Hamiltonian. A band structure that possesses an energy gap can be described by equivalent classes of Bloch Hamiltonians, where smooth deformations from one Hamiltonian to another do not result in the closing of the gap. These classes are characterized by a topological invariant $n \in \mathbb{Z}$, called the Chern invariant. The Chern invariant is a mathematical construct that can be

physically described by the Berry phase associated with the Bloch function. Knowing that the Bloch state is invariant under transformation

$$|u(\mathbf{k})\rangle \rightarrow e^{i\phi(\mathbf{k})}|u(\mathbf{k})\rangle \quad 2.3$$

We can define the Berry connection

$$\mathbf{A} = -i\langle u(\mathbf{k})|\nabla_{\mathbf{k}}|u(\mathbf{k})\rangle \quad 2.4$$

That it transform as $\mathbf{A} \rightarrow \mathbf{A} + \nabla_{\mathbf{k}}\phi(\mathbf{k})$ with 3.7 And accordingly, we can define the Berry curvature for a closed loop C in the \mathbf{k} -space as

$$\gamma_C = \oint_C \mathbf{A} d\mathbf{k} = \int_S \mathcal{F} d^2\mathbf{k} \quad 2.5$$

where $\mathcal{F} = \nabla \times \mathbf{A}$ is the Berry curvature (S is related to the closed surface). The Berry phase is one of the most important concepts in band theory. It describes the quantum adiabatic transport of a particle in a slowly changing field, such as an electric or magnetic field. Such transport occurs in the Bloch crystal structure (the motion of electrons within the band, which can be viewed as motion along a closed loop in momentum space). And it can be shown that for such transport occurring in the 2D Brillouin Zone, the topological invariant, called Chern number, is quantized and can be expressed as

$$n = \frac{1}{2\pi} \int_S \mathcal{F} d^2\mathbf{k} \quad 2.6$$

Generally, the Chern number n cannot change when the Hamiltonian changes smoothly, and based on the Gauss-Bonnet theorem, it is related to the genus g . This invariant plays a crucial role in explaining the integer quantum Hall effect, thanks to the TKNN theory⁶, which showed that the quantized Hall conductivity is precisely the Chern number.

$$\sigma_{xy} = \nu \frac{e^2}{h} \quad 2.7$$

where ν is the TKNN number (Chern number).

To delve further into the description of the quantum Hall effect, we need to invoke Haldane's theory², which describes the emergence of this phenomenon in graphene in a periodic magnetic field. Graphene⁷ is a material where the valence band and conduction band touch at two specific points in the BZ, and near these points, a linear dispersion of massless particles described by the Dirac equation is observed. Haldane's theory assumes that the Bloch Hamiltonian in the two-band model for p_z orbitals of two atoms in the unit cell can be expressed as

$$\mathcal{H}(\mathbf{k}) = \mathbf{h}(\mathbf{k})\vec{\sigma} \quad 2.8$$

where $\vec{\sigma}$ are Pauli matrices ($\vec{\sigma} = (\sigma_x, \sigma_y, \sigma_z)$) and $\mathbf{h}(\mathbf{k}) = (h_x(\mathbf{k}), h_y(\mathbf{k}), 0)$. Factor $h_z(\mathbf{k}) = 0$ because combination of inversion \mathcal{P} and time-reversal symmetry \mathcal{T} requires it (for \mathcal{P} : $h_z(\mathbf{k}) = -h_z(-\mathbf{k})$ and for \mathcal{T} : $h_z(\mathbf{k}) = h_z(-\mathbf{k})$). This leads to the emergence of a Dirac point, because $\mathbf{h}(\mathbf{k})$ can have zeros in two dimensions. According to this theory, graphene exhibits two so-called 2D massless Dirac Hamiltonians with linear dispersion.. In principle, breaking time reversal or inversion symmetry should open the gap in this massless states, leading to an ordinary insulator state. However, Haldane showed within this theory that this state is not insulating but rather has a quantized Hall conductivity.

2.2.3 Surface and edge states

One of the main consequences of applying topology in the classification of materials with an energy gap is the existence of gapless conducting states on the surface of such materials (at the interface where the topological invariant changes). The conducting states on the surface were predicted by Halperin⁸ in the integer quantum Hall state, and they can be described as states moving along cyclotron orbits, bouncing off the edges (edge state). These surface states are not dependent on impurities or structure disorder (because there are no available states for backscattering), making them ideal one-dimensional conducting channels (unlike bulk states). The formation of these energy channels can be explained based on filled Landau levels, which are quantized. Each such level acts as a generator of an edge channel. Ultimately, the number of these levels is closely related to the topological invariant and thus to the quantization of Hall conductance. However, the most important aspect is that in the quantum Hall effect, all bulk states are localized, while electrons on the surface form conducting channels characteristic to the topological phase. An alternative explanation for the formation of edge states (these states are chiral, meaning they propagate along the edge in only one direction) can be presented through Haldane's theory. In this case, when we change the Hamiltonian near the surface, it allows for a change in the dispersion of edge states. This change affects how many times the Fermi level is crossed by the edge state - there are two possibilities: with positive or negative group velocity. The number of such crossings cannot change and is determined by a topological invariant in the so-called *bulk-edge correspondence*

$$N_R - N_L = \Delta n \quad 2.9$$

N_R and N_L are right (positive velocity) and left (negative velocity) modes and Δn is the difference in the Chern number across interface (odd number of crossing implies existence of the metallic edge states).

According to Haldane's theory, breaking time reversal symmetry leads to the emergence of a topologically nontrivial state such as the quantum Hall effect. However, this simplistic model does not account for a very important property of particles, spin. Spin was introduced into topological phase theory in 2005 by Kane and Mele⁹ through the introduction of spin-orbit coupling, which allows for the formation of a nontrivial insulator phase while not breaking the time reversal symmetry. In this theory, an important role is played by time reversal symmetry (for fermions), which is represented by an antiunitary operator Θ , which $\Theta^2 = -1$ for an electron with spin $1/2$. From all above considerations, the time reversal symmetry invariant Bloch Hamiltonian must satisfy

$$\Theta \mathcal{H}(\mathbf{k})\Theta^{-1} = \mathcal{H}(-\mathbf{k}) \quad 2.10$$

and must not close the energy gap by smoothly deformed. Together with the application of Kramers theorem (the eigenvalues of Hamiltonian are doubly degenerate) and bulk-edge correspondence, this theory introduced a new topological invariant (time reversal classification), \mathbb{Z}_2 invariant¹⁰, which takes values 0 or 1 (for TKNN invariant equal 0) and can be calculated for real 2D materials. Based on this theory, by performing electronic structure calculations, one can determine whether a given material exhibits surface metallic states. In other words, it is possible to state whether a material qualifies as a 2D topological insulator or not. As move up in dimensionality, the concept of topological insulators can be generalized from 2D to 3D (unlike the quantum Hall effect). According to bulk-edge correspondence, for a 3D topological insulator, the invariant takes on four values $(\nu_0; \nu_1, \nu_2, \nu_3)$ ¹¹⁻¹³ where ν_0 describes how many times the Kramers points enclosed the Fermi circle (odd times for topological insulator and $\nu_0 = 1$ for strong 3D topological insulator). The surface electronic structure of a strong topological insulator resembles that of graphene, but unlike graphene, it possesses only a single Dirac point (four in the case of graphene). The existence of surface states in an topological insulator can be visualized on materials with inversion symmetry¹⁴, Figure 2, and by applying Dirac theory, which requires the mass term to change sign at the interface in such a case.

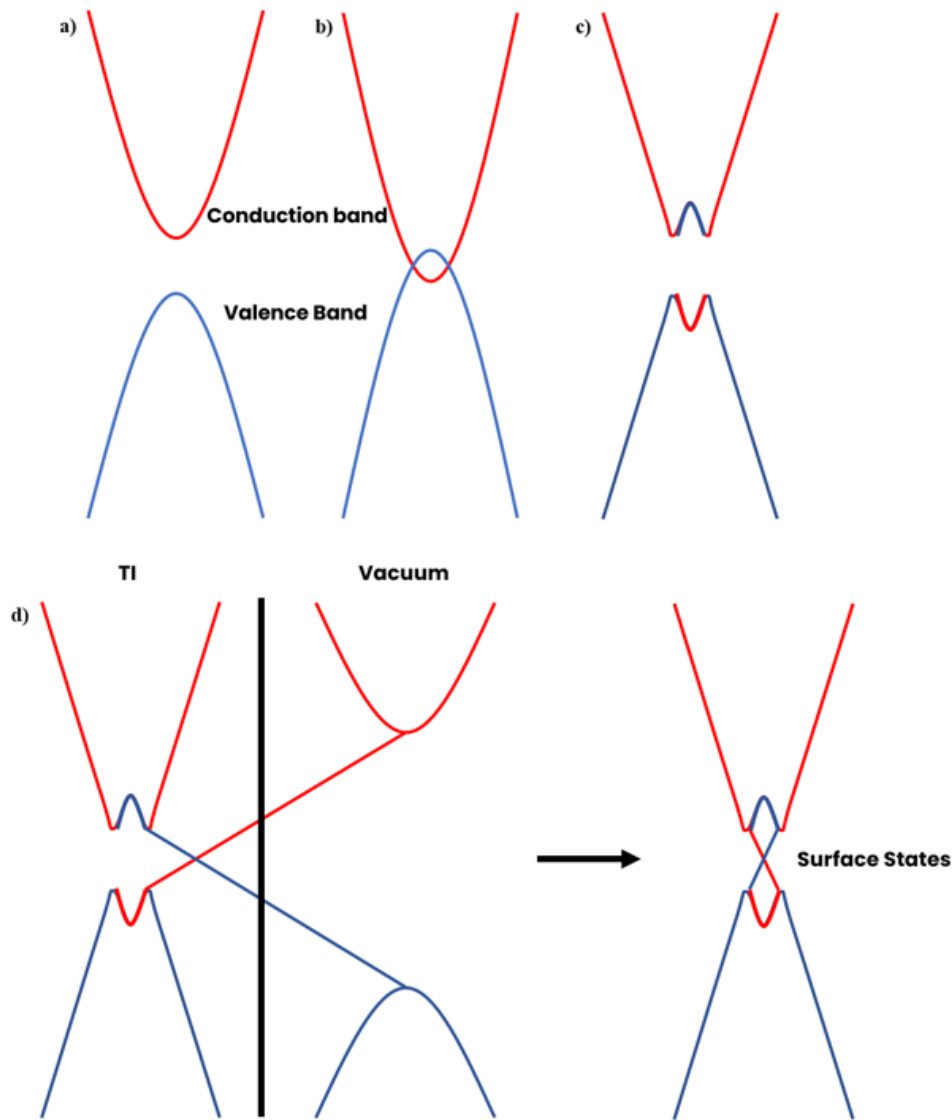


Figure 2 A simple illustrative presentation of the phenomena driving topological insulators and the existence of surface states. In a trivial insulator, parabolic conduction and valence bands (p-type) are distinguishable a), with the Fermi level located in the gap between these two bands. In materials with a high atomic number Z , the bands near high-symmetry points, such as Γ , can cross (b) in the absence of spin-orbit coupling (SOC). When SOC is present, this band crossing becomes unstable, leading to the opening of a gap, resulting in a non-trivial insulator with inversion symmetry, where the chemical potential is situated in the gap c). In d), the transition between a non-trivial insulator (left) and a trivial insulator (right, vacuum) is depicted. At the trivial-non-trivial interface, the transition is not smooth (different Chern number), necessitating the closure of the gap, which leads to the existence of surface states at the surface of the material, as shown in d).

The surface states generated in a strong topological insulator form a kind of flat metal^{11,15} on the surface. However, unlike a typical metallic state, in a topological insulator, the spin is not degenerate - time-reversal symmetry requires the spin to rotate as it moves across the Fermi surface. This behavior leads to the emergence of nontrivial Berry curvature, which has

consequences such as surface states being unable to localize even in the presence of strong disorder.

2.3 Overview of Experimental Studies on Topological Insulators

2.3.1 Experimental realization of 2D and 3D Topological Insulators

The first theoretically predicted material that was supposed to fulfill the requirements of a quantum spin Hall insulator (a 2D TI) was graphene⁹. The realization of the assumptions of a topological insulator in graphene was challenging due to its weak spin-orbit coupling and narrow energy gap in this material. Therefore, theoretical efforts were initiated to find materials composed of heavier atoms (strong spin-orbit coupling). These efforts were successful both theoretically¹⁶, in 2006, and experimentally¹⁷, in 2007, and was achieved in the class of semiconductors $\text{Hg}_{1-x}\text{Cd}_x\text{Te}$.

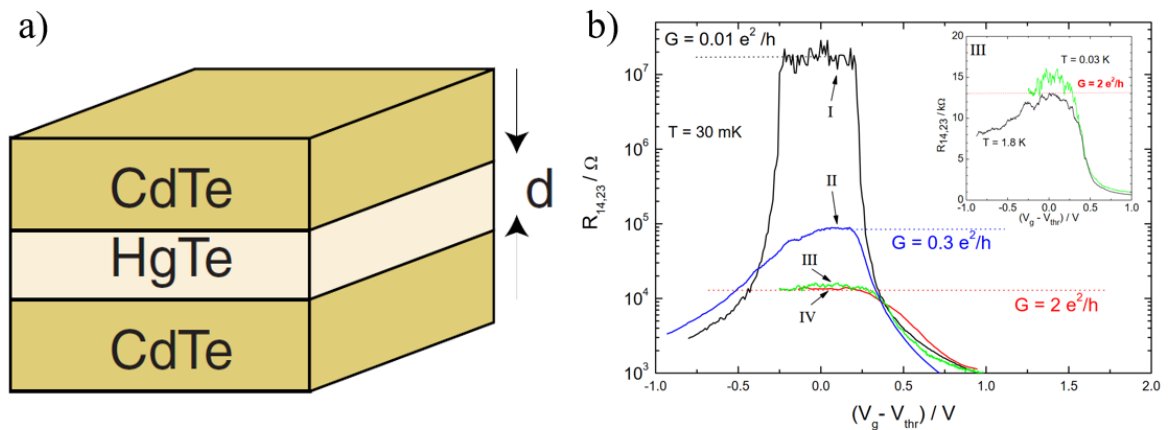


Figure 3 Layered CdTe/HgTe/CdTe quantum-well structures a). Longitudinal resistance of various quantum-well structures as a function of the gate voltage measured in zero magnetic field at 30 mK b). Structures show quantized conductance of $2e^2/h$, giving evidence for the 2D TI phase^{17,18}.

In this experiment, investigations of the transport properties of quantum wells in Hg/Te(Hg,Cd)Te material were conducted as a function of gate voltage, magnetization, and the thickness of the epitaxial layer. The research group demonstrated a transition from the insulator phase to a non-trivial insulator phase (to the spin quantum Hall state) under these conditions. The proof of the existence of this phenomenon in 2D triggered an avalanche of theoretical solutions^{11,12,15} aimed at creating a 3D topological insulator. Before discussing 3D TI's, we need to consider how we can classify topological phases. It is known that not every material can be considered as a TI. There exists a theoretical framework, developed within the field of topological band theory, which allows for the definition of the topological class of materials

capable of exhibiting such properties. This description is based on specific symmetries and dimensions^{18,19}. There are three topological classifications: \mathbb{Z} , \mathbb{Z}_2 , and $\mathbf{0}$, which correspond to the quantum Hall state, topological insulators, and superconductors, respectively.

Table 1 Periodic table of Topological state.

AZ	Symmetry			d							
	Θ	Ξ	Π	1	2	3	4	5	6	7	8
A	0	0	0	0	\mathbb{Z}	0	\mathbb{Z}	0	\mathbb{Z}	0	\mathbb{Z}
AIII	0	0	1	\mathbb{Z}	0	\mathbb{Z}	0	\mathbb{Z}	0	\mathbb{Z}	0
AI	1	0	0	0	0	0	\mathbb{Z}	0	\mathbb{Z}_2	\mathbb{Z}_2	\mathbb{Z}
BDI	1	1	1	\mathbb{Z}	0	0	0	\mathbb{Z}	0	\mathbb{Z}_2	\mathbb{Z}_2
D	0	1	0	\mathbb{Z}_2	\mathbb{Z}	0	0	0	\mathbb{Z}	0	\mathbb{Z}_2
DIII	-1	1	1	\mathbb{Z}_2	\mathbb{Z}_2	\mathbb{Z}	0	0	0	\mathbb{Z}	0
AII	-1	0	0	0	\mathbb{Z}_2	\mathbb{Z}_2	\mathbb{Z}	0	0	0	\mathbb{Z}
CH	-1	-1	1	\mathbb{Z}	0	\mathbb{Z}_2	\mathbb{Z}_2	\mathbb{Z}	0	0	0
C	0	-1	0	0	\mathbb{Z}	0	\mathbb{Z}_2	\mathbb{Z}_2	\mathbb{Z}	0	0
CI	1	-1	1	0	0	\mathbb{Z}	0	\mathbb{Z}_2	\mathbb{Z}_2	\mathbb{Z}	0

The so-called Periodic table of Topological Insulators Table 1 provides a framework for exploring various phases in the field.

Transitioning from 2D to 3D is not as straightforward due to the requirements that a three-dimensional material must meet (described in Chapter 2). Regardless, tremendous progress has been made in this field in the development of 3D materials. The first one was to be discovered was the alloy $\text{Bi}_x\text{Sb}_{1-x}$ ^{20,21}. In this experiment a high resolution ARPES data was collected for the single-crystal samples Figure 4. This pioneering experiment has set the pace for new discoveries in field of 3D topological insulators.

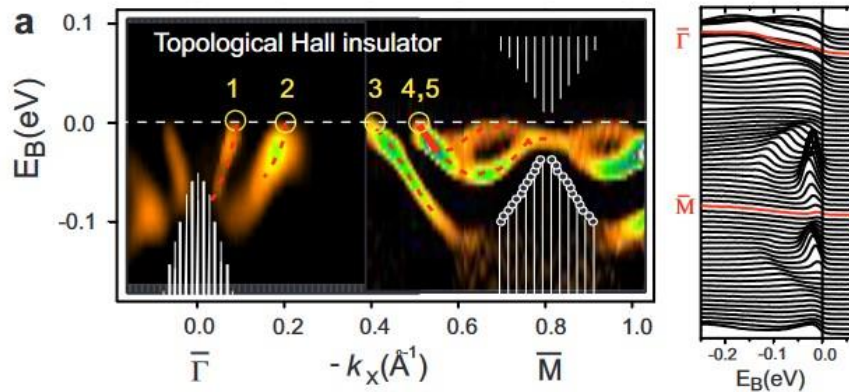


Figure 4 ARPES measurement of the topological gapless surface states in bulk insulating $\text{Bi}_{0.9}\text{Sb}_{0.1}$ ²⁰.

In the case of 3D topological insulators, transport measurements can be challenging due to the difficulty in separating surface conductivity from bulk conductivity. However, ARPES has

proven to be an ideal tool for studying surface states in these materials^{22,23}. ARPES allows for the investigation of the electronic band structure of a material, enabling imaging of surface states with high energy and momentum resolution. With its high resolution in the valence band regime, ARPES distinguishing surface states from bulk states. Surface states tend to exhibit characteristic features that can be easily identified; for example, their intensity may significantly differ from bulk states. Additionally, surface states do not vanish in the direction perpendicular to the surface, further aiding their identification via ARPES.

2.3.2 Bandgap semiconductors of heavy elements

It has been recognized that the most promising materials for realizing topological insulators are those build of elements with high atomic mass. This is because heavy elements enable the formation of strong spin-orbit coupling. Among this new generation materials²⁴ were narrow-bandgap semiconductors made of heavy elements. The first group of such materials were compounds like Bi_2Se_3 , Bi_2Te_3 and Sb_2Te_3 . The initial reports on the realization of the new generation of topological insulators emerged in 2008 and 2009²⁵, primarily focusing on the material Bi_2Se_3 ²⁵⁻²⁹ and it was demonstrated that this compound, with a very wide energy gap of 0.3 eV, belongs to the group of topological insulators Figure 5.

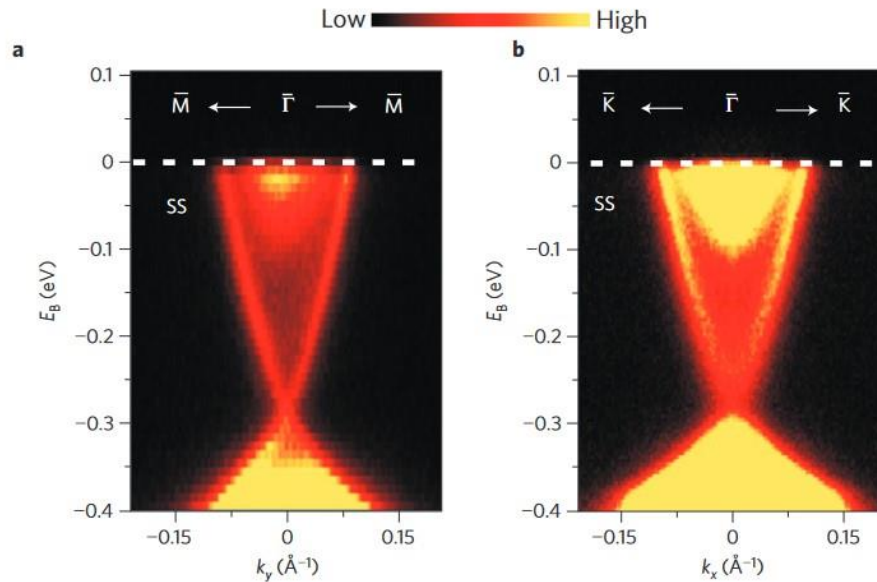


Figure 5 Bi_2Se_3 surface states, ARPES data collected for Γ -M a) and Γ -K b) direction along the BZ²⁹.

The same observations were made for Bi_2Te_3 and Sb_2Te_3 compounds. The entire group of compounds is classified as strong topological insulators. In the following years, tremendous efforts were made to characterize other materials exhibiting similar properties. Table 2

presented several selected compounds that exhibited topological insulator properties (shortly after the first experimental confirmation of 3D TI's).

Table 2 Summary of experimentally confirmed topological insulators³⁰

Type (according to ¹¹)	Material	Band gap
2D, strong	CdTe/HgTe/CdTe	~ 10 meV ¹⁷
2D, strong	AlSb/InAs/GaSb/AlSb	~ 4 meV ³¹
3D, strong	Bi _{1-x} Sb _x	~ 30 meV ²⁰
3D, strong	Sb	Semiconductor ²¹
3D, strong	Bi ₂ Se ₃	0.3 eV ²⁹
3D, strong	Bi ₂ Te ₃	0.17 eV ³²
3D, strong	Sb ₂ Te ₃	0.3 eV ³³
3D, strong	(Bi,Sb) ₂ Te ₃	~ 0.2 eV ³⁴
3D, strong	Bi ₂ Te _{1.6} S _{1.4}	0.2 eV ³⁵
3D, strong	PbBi ₂ Te ₄	~ 0.2 eV ³⁶
3D, TCI	SnTe	0.3 eV ³⁷
3D, TCI	Pb _{1-x} Sn _x Te	~ 0.3 eV ³⁸

2.3.3 Crystal and electronic structure of Bismuth Telluride

Bismuth telluride, Bi₂Te₃, has been a well-known material with excellent thermoelectric properties since the 1950s and 1960s³⁹, which have been improved over the years⁴⁰. Due to its good thermoelectric properties, other phases of Bi-Te have been studied. According to the phase diagram of Bi-Te (Figure 6), it forms seven stable compounds, including Bi₂Te₃, which is stable in a very narrow compositional range (Bi 40% and Te 60%) and exhibits the highest formation temperature among all the studied phases.

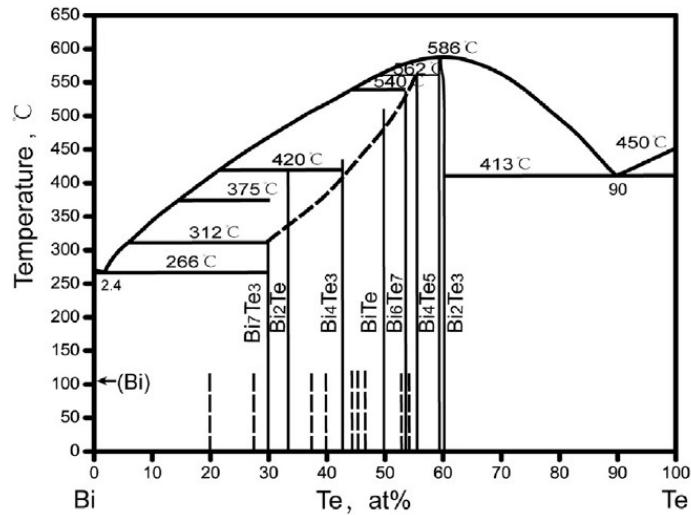


Figure 6 Bi-Te phase diagram^{41,42}

Since the prediction and experimental evidence of the existence of topological insulator properties in this material, it has regained the attention of scientists and is considered a potential candidate for spintronics applications. Bi_2Te_3 is layered materials with a rhombohedral crystal structure (space group $D_{3d}^5(R\bar{3}m)$). The unit cell (parameters for hexagonal cell are $a = 4.395\text{\AA}$, $c = 30.44\text{\AA}$, $\alpha, \beta = 90^\circ$, $\gamma = 120^\circ$) is composed of five hexagonal layers with stacking sequence of Te(1)-Bi-Te(2)-Bi-Te(1) which create a quintuple layer (QLs) Figure 7. a). The bonds within QL have a covalent character, however, at the connection of two QLs (Te(1)-Te(1)), the bond exhibits van der Waals character (vdW). This is due to the significant distance between the two Te(1) layers, approximately 3.65\AA , which is considerably larger than the typical covalent bond distance for Te-Te (2.7\AA)⁴³. Due to the strong covalent bonding within QLs and weak vdW interactions at the QL-QL interface, Bi_2Te_3 is a material that naturally cleavage easily along the weak interlayer bond.

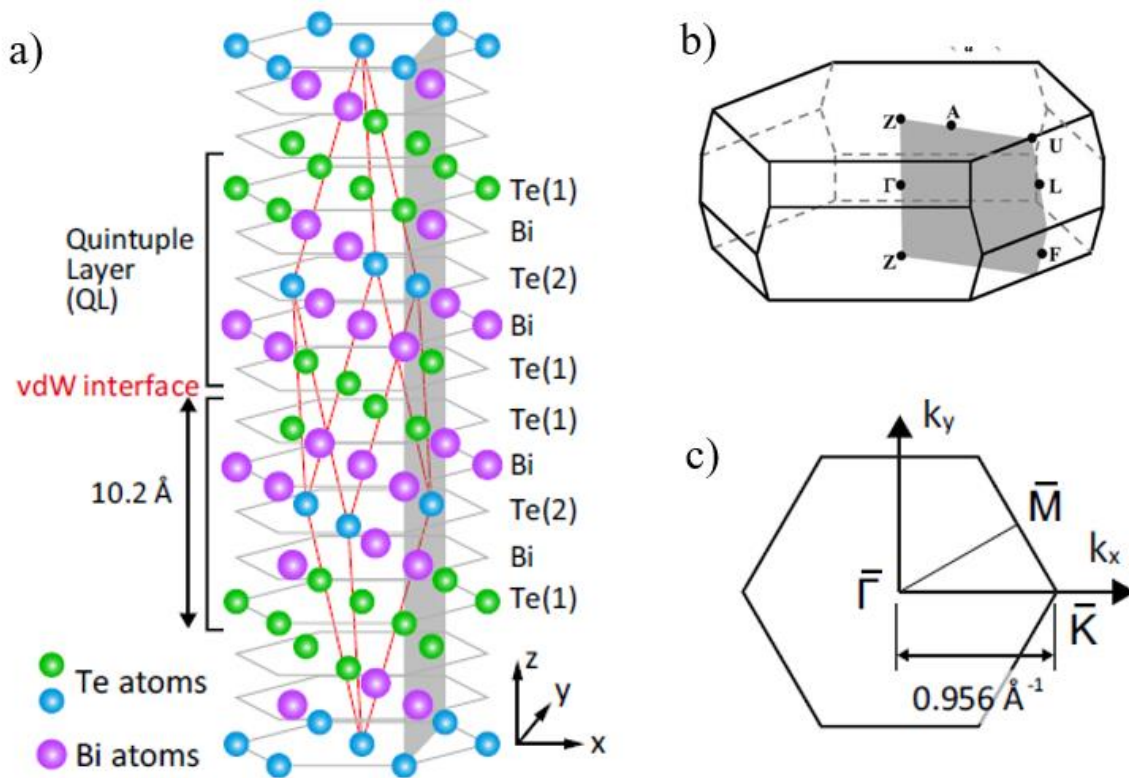


Figure 7 Bi_2Te_3 crystal structure. a) hexagonal unit cell⁴³, b) the Brillouin zone of the rhombohedral cell⁴⁴ and c) is the Bi_2Te_3 2D Brillouin zone.

Experimental and theoretical studies of the electronic structure of materials exhibiting 3D topological insulator properties are a major focus in contemporary solid-state physics. Due to its wide energy gap and rich electronic structure, Bi_2Te_3 is an ideal subject for research due to induced modifications in its electrical properties, such as surface modifications or the introduction of defects or structural dopants. Theoretical calculations using first-principles local-density FLAPW⁴⁵ and ab-initio DFT methods^{46,47} show that the direct gap occurs in the high symmetry point Γ in the Brillouin zone (Figure 7 a)). Typically for materials with heavy atoms, such as Bi and Te, calculations are performed with SOC. In the Figure 8 b), we can see a significant contribution of SOC in the electronic structure of Bi_2Te_3 . Considering SOC, which leads to phenomena such as band inversion at the gamma point, we can observe the emergence of a non-trivial energy gap.

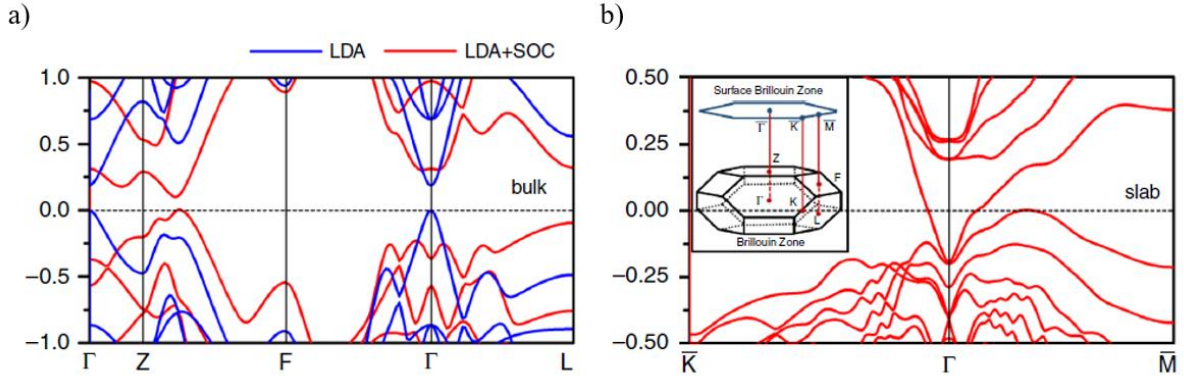


Figure 8 Bi_2Te_3 , DFT (LDA), band structure calculation for a) bulk and b) slab. Red and blue lines indicates calculation with and without SOC, respectively⁴⁷.

Strong SOC in Bi_2Te_3 leads to various phenomena such as the opening of the energy gap, well degeneracy, a rich electronic structure, and ultimately to the emergence of surface states. Surface states, due to being protected by time reversal symmetry, are resistant to surface perturbations (e.g., influence of external molecules), yet they are sensitive to the influence of magnetic impurities. Introducing an external magnetic field to a topological insulator should lead to phenomena such as the opening of the gap and QAH.

2.3.4 Doped Bi_2Te_3

Over the past 15 years, numerous experiments have been conducted on Bi_2Te_3 and Bi_2Se_3 , involving the introduction of both magnetic⁴⁸ and non-magnetic dopants or the deposition of thin layers on top of the TI. Non-magnetic dopants are a common approach to influence factors such as carrier type or electrical properties. Main non-magnetic solid elements include Cu⁴⁹, Ca⁵⁰, or Sb^{51,52}, which can be introduced into the structure using methods such as MBE or Bridgman method. Non-magnetic impurities can also be introduced as gas molecules (like air⁵³ or CO⁵⁴), which can migrate into the material or cause the formation of a passivation layer and creating the 2DEG. The essence of exposing the surfaces of topological insulators to environmental conditions lies in their potential future applicability. The basis of such actions is the modification of the surface while preserving surface states.

As opposed to non-magnetic impurities, magnetic impurities can lead to the breaking of time-reversal symmetry, which may result in the phenomena described earlier. Due to this, significant efforts have been made to investigate the impact of external magnetic fields on the transport properties of topological insulators. The most popular methods of introducing magnetism into these materials include structural doping or deposition of thin layers. Since the beginning, the

primary focus has been on the influence of transition metals such as Mn^{55,56}, Cr^{57,58}, or V⁵⁹ on the modification of the electronic structure of topological insulators. One of the main elements used for the modification of these materials is iron. Iron structures exhibit strong magnetic properties due to their atomic configuration and electronic structure (partially filled d shell). Due to this fact, significant amount of research have been made to describe the processes occurring in topological insulators under the influence of this element. In the case of Bi₂Te₃, several experiments have been conducted^{48,60–63}.

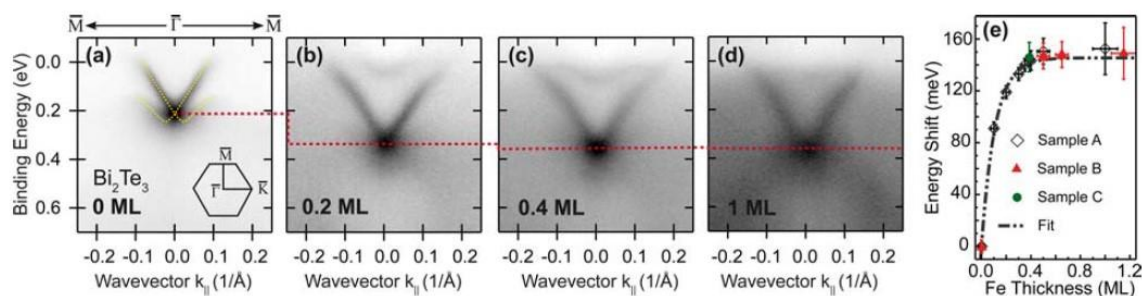


Figure 9 ARPES spectra collected for single crystal Bi₂Te₃ with excitation energy of 55 eV. a) to d) is the surface states behavior under deposition of Fe.

One example are studies made by Scholz⁶⁴ where iron film was deposited at the surface of Bi₂Te₃ single crystal. The ARPES research in this article demonstrated the modification of the electronic structure while simultaneously preserving surface states Figure 9. Report includes realization of the band-bending scenario (n-type) and creation of the 2DEG. The resistance of surface states to the influence of the magnetic layer allowed speculation about additional factors that must be fulfilled to open an energy gap, such as the appropriate direction of magnetization (the same group conducted research on Bi₂Se₃ under the influence of Fe deposition⁶⁵).

Another type of experiment is doping. In the work⁶⁶ made by Jo, the influence of iron doping on the electronic structure of Bi₂Te₃ was demonstrated. In this experiment, alloys were produced by the method of consistent melting from pure elements. This process was crucial as it allowed for the design of the electronic structure - by using excess Bi, defects can be created, leading to the formation of p-type charge carriers (in the case of excess Te, n-type carriers are formed). In this study, samples were prepared with an excess of Te and with varying atomic content of Fe. It was demonstrated that as the Fe content increased in the structure, the doping character changed to p-type. The materials were characterized using ARPES, diffraction methods, and magnetization measurements, which allowed the determination that Fe is in the divalent form. In this case as well, the surface states were preserved, and the energy gap remained unopened.

One of the many elements that has drawn the attention of scientists as a potential dopant for topological insulators is cobalt. Cobalt is an element with a very high Curie temperature (higher than iron) and weaker magnetic properties. Due to its crystalline structure, it also exhibits a different character of magnetic anisotropy compared to iron. Compounds with this element may demonstrate a high level of resistance to environmental conditions, which is very significant in the application context. In the study made by Makarova⁶⁷ the changes in the electronic structure of Bi₂Te₃ under the influence of Co atom deposition on its surface were investigated. In this experiment, Co was evaporated onto the material's surface at a high temperature of 420°C, and then the prepared material was annealed at a temperature close to the melting point of the substrate, 585°C. ARPES studies showed that with the increasing thickness of the Co layer (from 1 Å to 3 Å), the Dirac point migrated towards lower binding energies, implying the generation of n-type carriers. XPS measurements of core states revealed the possibility of the formation of a Co compound with Bi or Te. Finally, with the increase in layer thickness, the intensity of the surface states decreased in ARPES. The influence of both elements, Fe and Co, on the magnetic properties and electronic structure of Bi₂Te₃ was investigated in the work by Shelford⁶⁸. Samples were prepared by depositing transition metals onto the surface of a monocrystalline topological insulator (with a thickness of approximately 0.5% ML). XMCD studies confirmed that the thin coatings of Fe and Co did not lead to the disappearance of surface states.

The rich electronic structure and relatively easy access to surface states via ARPES have enabled scientists to conduct spin-resolved measurements of 3D topological insulators. However, due to the low efficiency of spin-resolved photoemission measurements (even up to 1000 times lower than conventional photoemission), the research process becomes highly time-consuming and often impractical. Scientists have sought new solutions for sampling spins, and one potential solution was CD-ARPES. However, it quickly became apparent that unraveling spin-related information from CD measurements was difficult to interpret. Nevertheless, CD-ARPES has proven to provide insights into the Orbital Angular Momentum (OAM) of electrons. However, it was also found that data analysis is very complicated in this area. In this dynamically changing field, techniques for analyzing data obtained in CD-ARPES measurements are still being sought, which will allow for unambiguous extraction of information about the OAM of electrons. Numerous theoretical studies have been conducted to elucidate the information obtained through this technique. Access to OAM information in semiconductor or magnetic materials is highly significant in terms of applications in quantum

optics or quantum computing. In the case of TIs, CD-ARPES measurements have been conducted for many compounds, including Bi_2Te_3 . However, due to difficulties in data analysis, most studies focus on investigating changes in the CD signal as a function of material thickness and excitation energy.

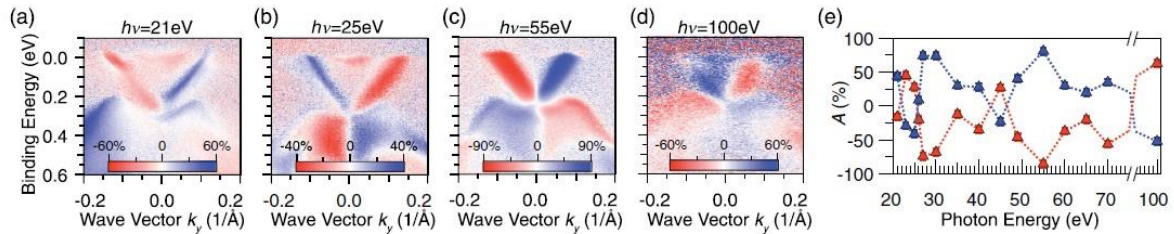


Figure 10 Circular dichroism effect measured for Bi_2Te_3 with ARPES. ARPES data a - d) show sign change of the effect with energy range from 21 to 100 eV. e) is the plot of the circular dichroism sign for different excitation energies.

In the research conducted by Scholz⁶⁹ the influence of different excitation energies, from soft x-rays range, was studied. It was shown that in a narrow energy range, from 21 to 100 eV, the experimental CD signal changes its sign Figure 10. Based on several theoretical models, it was excluded that this signal could originate from changes in spin texture (it should not depend on the excitation energy). However, it was also demonstrated that such a change could occur for calculations performed in a one-step model. Subsequent studies, conducted by Xu⁷⁰, demonstrated the electronic structure of Bi_2Te_3 using CD-ARPES, incorporating both experimental and theoretical data. The main focus of these studies was to show how the thickness of thin film layers of this material affects the CD signal from the surface states. It was shown that transitioning from a system with 1 QL to a system with 12 QLs results in a change in the sign of the surface states CD signal. Ultimately, based on theoretical and experimental results, it was demonstrated that the thickness of the layer, excitation energy, crystal momentum, and measurement geometry play a significant role in interpreting the CD signal. These conclusions highlight the considerable challenge in interpreting CD data.

Chapter 3 Experimental details

Chapter 3 outlines the experimental methods used in the study. Section 3.1 focuses on the growth of thin films and their structural characterization, detailing the use of MBE, interface formation, and Low Energy Electron Diffraction (LEED) for structural analysis. Section 3.2 describes various photoemission spectroscopy techniques, including the basics of photoemission, ARPES, XAS, and CD-ARPES for probing electronic structure and magnetic properties. Section 3.3 provides an overview of the experimental setup, including the radiation sources, generation of the synchrotron radiation, and descriptions of beamlines PHELIX and URANOS at SOLARIS National Synchrotron Radiation Centre, along with the sample preparation process.

3.1 Thin films growth and structural characterization

3.1.1 Molecular Beam Epitaxy

MBE is an experimental technique that allows for the fabrication of thin (atomic-scale) layers of materials under ultra-high vacuum conditions. Due to the significant demand for clean semiconductor materials, the technique has become highly popular not only in scientific laboratories but also in industrial applications over the past 30 years. The operation of MBE is based on epitaxial growth of layers on a crystalline substrate using atomic beams. Pure materials (solid state, purity level of 99.9999%) are placed in effusion cells or electron beam evaporators, where they are vaporized into the volume of the MBE chamber under the influence of high temperature or an electron beam (the general principle of operation is shown in Figure 11 b)). The entire process is conducted under vacuum conditions to minimize the formation of defects resulting from the interaction of the substrate or reaction of evaporated atoms/molecules with residual gas molecules. A standard example of an MBE chamber is shown on Figure 11 a). MBE not only enables the fabrication of chemically and structurally ultra-clean materials but also allows for the modification of their morphology.

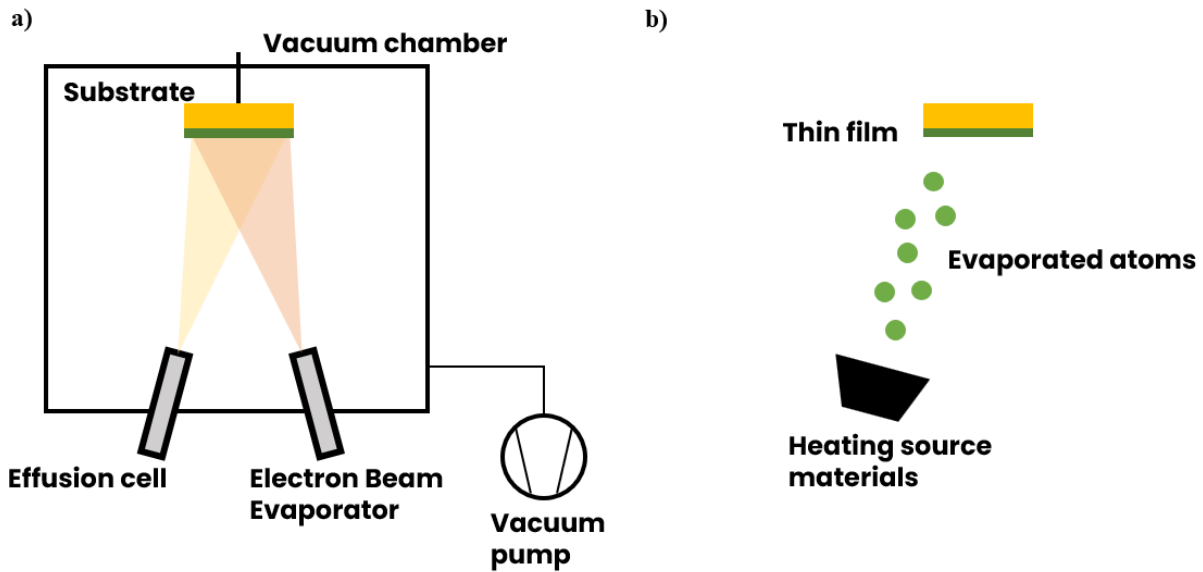


Figure 11 Illustrative example of a standard MBE chamber with two types of material sources in a). b) presenting the thermal deposition process. The deposition is carried out in a UHV environment. The material is heated by e.g. resistive heating, and the evaporated material is directed onto the substrate.

One of the most popular physical methods for creating thin films is electron beam evaporation. The evaporant (source material) is placed in a cell, under the filament's window, typically made in the form of a loop (mostly from tungsten). The flow of electric current through the filament heats it, generating an electron beam through thermoemission. These electrons are accelerated towards the evaporant surface by an anode. Accelerated electrons bombard the material surface, causing it to heat up (during bombardment, many other phenomena are observed, such as backscattered electrons, secondary electrons, or the emission of X-rays. However, a large portion of the kinetic energy of electrons results in the generation of heat energy, and the rest of the effects can be disregarded) until it release its vapors (evaporation or sublimation). Accelerating voltage is also applied to intensify the evaporation process. This technique allows for the creation of highly pure layers from materials with very high melting temperatures or high chemical reactivity, which is often difficult to achieve with other methods.

One of the most important aspects of MBE is the growth process, which is determined by how atoms or molecules organize themselves on the substrate during deposition. These growth modes are influenced by various factors such as substrate temperature, deposition rate, lattice mismatch, and surface energies. The main growth modes include:

- Frank-van der Merwe growth (layer by layer) - in this mode the thin film grows one atomic layer at a time. Each layer is completed before the next one starts. This growth occurs when the interaction between the substrate and the deposited atoms is strong

enough to favor a smooth, continuous film over three-dimensional structures. The atoms have a tendency to spread out across the substrate surface, forming a complete monolayer before the next layer starts to form.

- Volmer-Weber growth (islands) – in this method atoms tend to form small, three-dimensional islands on the substrate rather than spreading out to form a continuous film. This growth mode occurs when the interaction between the deposited atoms is stronger than the interaction between the atoms and the substrate. As a result, atoms cluster together to minimize their surface energy, leading to the formation of discrete islands.
- Stranski-Krastanov growth (layer and island) - this method starts with layer by layer growth, but after a few monolayers, the strain between the film and substrate causes the growth to transition to island formation. The initial layers grow smoothly as in Frank-van der Merwe mode, but after reaching a critical thickness, the strain energy due to lattice mismatch becomes significant. To relieve this strain, the system transitions to forming 3D islands on top of the thin film.
- Step-flow growth - in this mode, atoms migrate and attach themselves to the steps or terraces on the substrate surface, causing the steps to advance across the surface. Atoms landing on the surface diffuse until they reach a step edge, where they are incorporated into the crystal lattice. This leads to the formation of a smooth film, as the steps move across the substrate, incorporating atoms layer by layer.

3.1.2 Interface formation

The MBE system, equipped with EBV, enables the fabrication of clean thin layers of materials (elements), including transition metals. This technique allows for very precise modification of semiconductor surfaces or surface materials, such as topological insulators. Modifications can involve chemical reactions, mechanical interactions, as well as surface coating. Theoretical description of surface modifications in metals, semiconductors, and topological materials is very challenging and feasible only for pure systems (absence of dopants, impurities). Therefore, the prospect of clean experiment is crucial for combining the obtained experimental data with theory. In the case of topologically insulating materials, where surface states are topologically protected, the idea emerged to modify their morphology to protect surfaces from environmental conditions (such as oxidation) and induce other physical phenomena such as the quantum anomalous Hall effect. To achieve this, one can create a metallic interface on the surface of a topological insulator. According to Lüth, *A solid interface is defined as a small number of atomic layers that separate two solids in intimate contact with*

one another, where the properties differ significantly from those of the bulk material it separates⁷¹. Of course, there are also simpler types of interfaces, such as vacuum-solid interfaces. However, due to their technological importance, information about the properties of solid-solid interfaces is most desirable. One of the most common types are semiconductor interfaces, such as interfaces in semiconductor heterostructures or metal-semiconductor junctions (MOS structure). Generally, creating a solid-solid interface is highly complex, and numerous factors must be considered when designing such structures, including thermodynamic parameters and phase diagrams. The interface can be fabricated under controlled conditions using the MBE method. A thin layer of material can be deposited onto a crystalline substrate and adopt its crystalline structure - epitaxial growth. The growth process of such a layer consists of several stages. The first is the condensation of the evaporated material on the substrate (from the cell e.g., EBV), whose rate r can be described by the formula

$$r = \frac{1}{p\sqrt{2\pi MKT_0}} \quad 3.1$$

where p is the vapor pressure, M molecular particle weight, k is the Boltzmann constant and T_0 is the temperature. During the deposition of the layer, several processes can occur on the surface of the substrate Figure 12, such as:

- Absorption of particles on the substrate surface,
- Re-evaporation of particles from the substrate surface,
- Diffusion of particles across the substrate surface, which may ultimately result in particle absorption or re-evaporation.

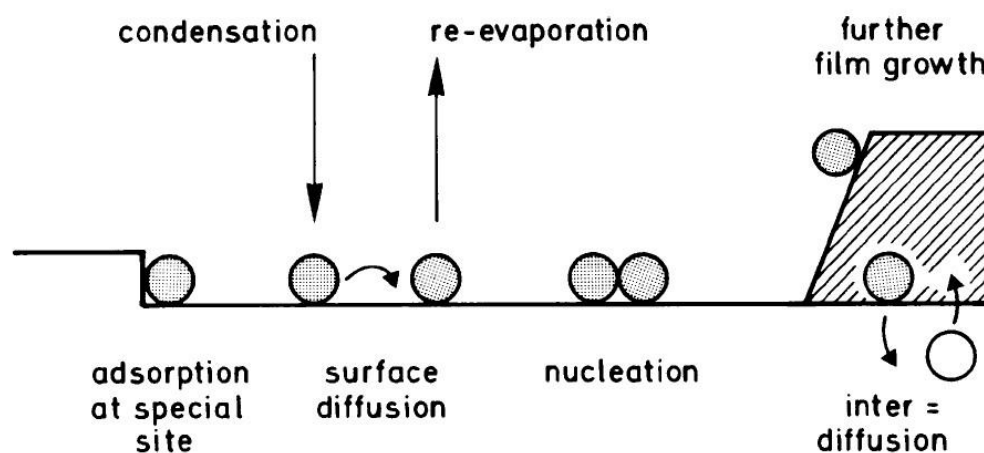


Figure 12 Illustrative example of atomic processes that drive film growth during thermal deposition onto a solid substrate⁷¹.

To ensure that particles are absorbed on the surface, a specific characteristic activation energy (deposition energy) must be overcome. The value of this energy depends mainly on the atomic properties of the substrate surface and the evaporated material. The quality and properties of the final interface obtained depend on the type of process pathways that occurred during the fabrication of the thin layer. To eliminate additional factors that could influence the properties of the fabricated layer or interface, these processes should be conducted under ultra-high vacuum conditions. This is a crucial factor that has a significant impact on the "freshness" of the investigated surfaces. To illustrate the influence of the residual gas pressure p on the material's surface, we need to present the following formula

$$p \cong \frac{6kTz}{\langle v \rangle} \quad 3.2$$

where k is the Boltzmann constant, T is temperature, in K degrees, and z is the frequency coefficient of gas molecule events with the surface [$\frac{1}{cm^2s}$]. Making certain assumptions about the number of atoms/molecules constructing a monolayer, the mass of molecules, and the temperature, we can demonstrate that under conditions of high vacuum, at the level of 10^{-6} mbar, gas molecules can form a monolayer within one second. Maintaining ultra-high vacuum conditions, at the level of 10^{-10} mbar, during the interface fabrication allows for the neglect of these processes. In addition to selecting an appropriate methodology for thin film fabrication and ensuring proper vacuum conditions, another important parameter influencing the quality of the fabricated interface is the preparation of the substrate surface. In experiments with modern semiconductor materials, the easiest and most popular method is cleavage under ultra-high vacuum conditions (for single crystals, annealing combined with ion sputtering is also utilized). Cleaving samples involves applying significant stress to the material using a knife or dedicated blade in a vacuum system. This process exposes a fresh, untouched surface. Often, this surface is not flat and contains many defects, but for hard materials, it is often the only solution.

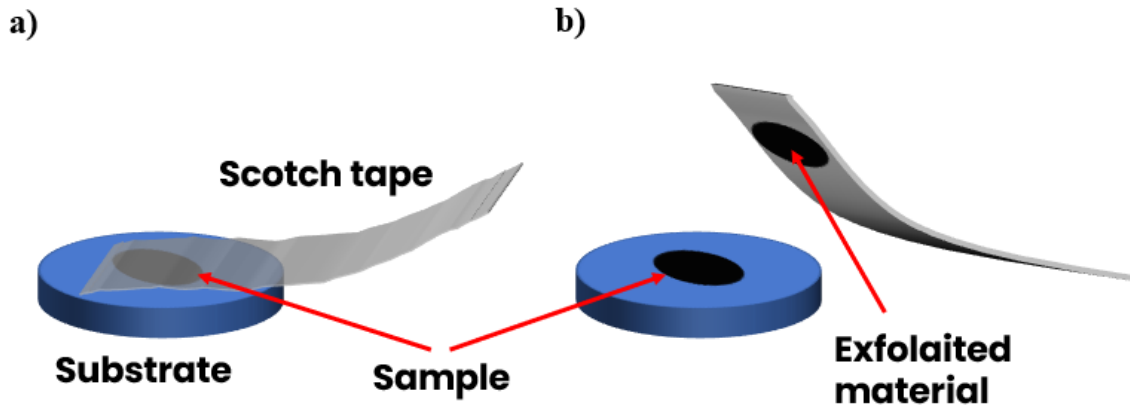


Figure 13 The mechanical exfoliation process using scotch tape: The tape is applied to the material's surface, a), and then, with applied force, it is peeled off, b). This removes a few layers of the sample, revealing a fresh surface.

Other cleaving techniques are also used, such as exfoliation Figure 13. Exfoliation can be applied to samples with a so-called layered structures. Materials with such a characteristic structure are composed of layers that are weakly bonded together by van der Waals forces. Thanks to this property, exfoliation can be employed, which involves peeling off the top layer of the material using adhesive tape. One of the most characteristic materials for which this technique is used is graphene. This technique can also be applied to many semiconductor materials (metal dichalcogenides such as WSe_2) and topological insulators (such as Bi_2Te_3 or Bi_2Se_3).

The process of cleaving or exfoliating a surface often leads to the formation of a non-uniform sample surface, and frequently, such a process needs to be repeated. However, surface quality assessment is not always conducted organoleptically. There are measurement techniques that allow for measuring the crystalline structure of the material surface in situ, one of which is LEED.

3.1.3 Structural characterization by Low Energy Electron Diffraction

LEED is a standard technique used to characterize the atomic structure of material surfaces, primarily freshly prepared crystalline materials or deposited layers. The principle of this technique is based on the phenomenon of scattering low energy electrons, ranging from 20 to 200 eV, on the material's surface. According to the de Broglie wavelength formula

$$\lambda = \frac{h}{p} = \frac{h}{\sqrt{2m_e eV}} \quad 3.3$$

where p is the momentum of the electron and V is the accelerating voltage, the wavelength of the electrons within this energy range is comparable to the interatomic spacing which makes it suitable to the diffraction measurements. As a result of the interaction between electrons and substrate atoms, a so-called LEED pattern forms on the fluorescent screen Figure 14 a). The measurement relies on the symmetry and distance of points in the diffraction pattern (LEED pattern) and the Bragg condition has to be conserved

$$2d \sin \theta = n\lambda \quad 3.4$$

where d is the interplane spacing distance, θ is the electron incident angle and n is the order of the diffraction. Since the diffraction pattern corresponds to the distribution of atoms in the reciprocal lattice vector \mathbf{G} , one can apply a transformation that reveals the distribution of atoms in the real space which can be approximately expressed as

$$d_{LEED} \propto \frac{1}{a_{real}} \quad 3.5$$

and the conclusion that can be taken from 3.5 is that as a larger real space lattice is measured the diffraction spots on the LEED pattern are closer to each other. The standard LEED setup consists of an electron gun and a fluorescent screen, which allows observing the Bragg diffraction spots Figure 14 b). The high surface sensitivity is ensured by using low-energy electrons (below 200 eV), which result from the small mean free path in this energy range Figure 17.

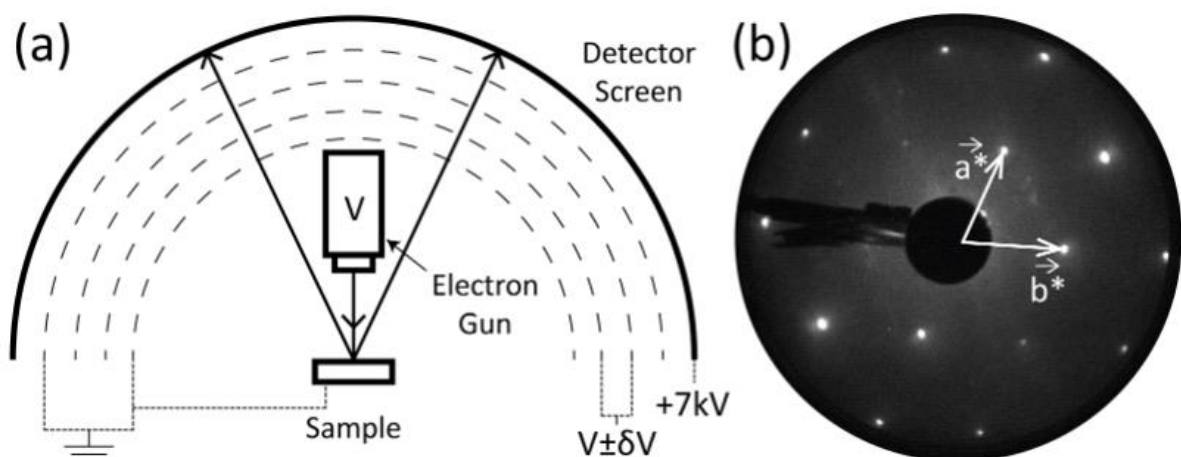


Figure 14 a) LEED standard setup and b) LEED pattern recorded from the clean Mo(110) surface⁷².

3.2 Photoemission Spectroscopy

3.2.1 Photoemission background

The phenomenon of electrons being ejected from a material, such as metal, when illuminated by electromagnetic waves was first demonstrated in an experiment by H. Hertz in 1887⁷³. It took almost 20 years for a theoretical explanation of this discovery to be presented, which was introduced by A. Einstein in 1905⁷⁴, made possible by the rapid evolution of quantum mechanics. In his work, Einstein described this phenomenon through the quantization of light into particles (photons) with discrete amounts of energy that depend on the light's frequency ν :

$$E_{kin} = h\nu - \phi \quad 3.6$$

where E_{kin} is the kinetic energy of the emitted electron is determined by Planck's constant h and ϕ which represents the work function - a parameter related to the minimum energy required for an electron to be emitted from the surface of the material. Einstein's theory and explanation of the photoelectric effect earned him the 1921 Nobel Prize in Physics.

In the following decades, significant efforts were made in both theoretical understanding and experimental exploration of the photoelectric effect. More sophisticated photoelectron measurement tools were introduced during this time. In the initial photoelectron experiments, light from a continuous source was monochromatized within a prism, and the photoelectron current was measured with respect to the applied retarding voltage using a counter electrode. The rapid development of instrumentation allowed for the enhancement of construction and efficiency of photoelectron analyzers, as well as experimental chambers capable of achieving ultra-high vacuum levels. The improvement of light sources, such as x-ray tubes or discharge lamps, also had a substantial impact. These advancements gave rise to a new method, Photoemission Spectroscopy (PES)⁷⁵.

In the late 1950s, K. Siegbahn initiated the development of photoemission spectroscopy for investigating the energy levels of core electrons in materials using X-ray tubes. With the principle of energy conservation governing the photoemission process, it became feasible to determine the binding energy of these electrons in solids by measuring their kinetic energy

$$E_{kin} = h\nu - \phi - |E_{bin}| \quad 3.7$$

where $h\nu$ is the photon energy and $|E_{bin}|$ is the electron binding energy. PES experiments required well-monochromatized light and stable light sources. Throughout the development of

PES, notable progress was made in light source technology, culminating in the advent of the next generation of sources like synchrotrons and, more recently, free-electron lasers.

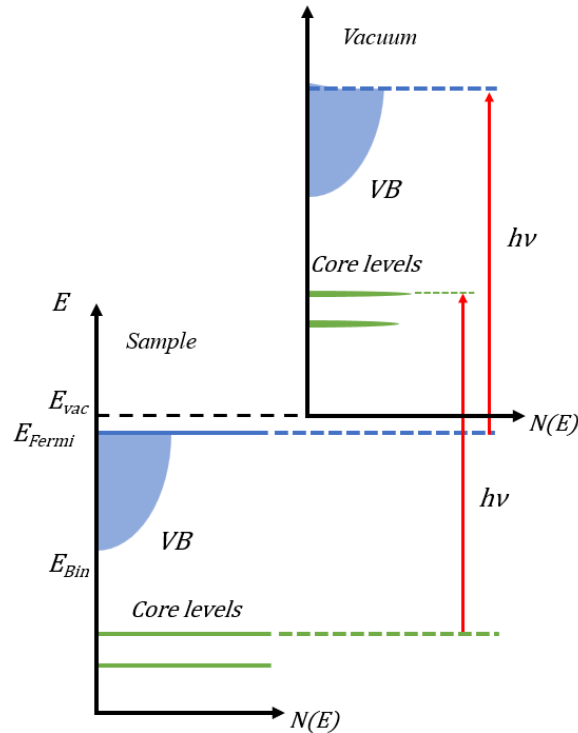


Figure 15 Relationship between the energy levels in the solid and the electron energy distribution produced by photons with energy $h\nu$.

In general, PES is a method where in the material's surface is illuminated by photons with energy $h\nu$, prompting electrons to transition from occupied to unoccupied states within the electronic structure. If these states lie above the vacuum level E_{vac} , the energy (and momentum) of the photoelectrons can be measured. Consequently, the system is left with one electron removed (or with an added positive charge). It's crucial to recognize that the initial state before excitation differs from the final state without the electron. The photoemission process engenders a complex interplay of correlated effects, complicating the overall understanding of the phenomenon. To gather information from PES, simplifications are necessary, with one of the most significant being the so-called sudden approximation. In this approximation, it's assumed that the excited electron doesn't interact within the system, and any hole created in this process is instantaneously filled by another electron. The probability ω of transition from the initial state i with associated wave function ψ_i to the final state f with wave function ψ_f is determined by Fermi's Golden Rule:

$$\omega \propto \frac{2\pi}{\hbar} |\langle \psi_f | \Delta | \psi_i \rangle|^2 \delta(E_f - E_i - \hbar\nu) \quad 3.8$$

where \hbar is Planck constant, E_f and E_i are final and initial state bindings energies. The delta factor $\delta(E_f - E_i - \hbar\nu)$ ensures that energy is conserved during the transition process. Δ , the perturbation operator, describes interaction between the system electron and the photon (electromagnetic wave) as

$$\Delta = -\frac{i\hbar e}{2mc}\nabla\cdot\mathbf{A} - \frac{i\hbar e}{mc}\mathbf{A}\cdot\nabla + \frac{e^2}{2mc^2}|\mathbf{A}|^2 - e\phi \quad 3.9$$

where \mathbf{A} is a vector potential and ϕ is scalar potential (not to be confused with the work function). We can simplify equation 3.9 by making few assumption. Since we can choose the photon energy for the photoemission process, which is typically carried out with UV or soft x-ray light, we can assume that the vector and scalar potentials are zero ($\nabla\cdot\mathbf{A} = 0$, $\phi = 0$). We can also neglect the field potential $|\mathbf{A}|^2$ (although it cannot be neglected when using hard x-rays). If the momentum operator of the electromagnetic wave can be written as $\mathbf{p} = i\hbar\nabla$, then we can simplify the perturbation operator to

$$\Delta = \frac{e}{mc}\mathbf{A}\cdot\mathbf{p} \quad 3.10$$

and the transition probability can we written as

$$\omega \propto \frac{2\pi e}{\hbar mc} |\langle\psi_f|\mathbf{A}\cdot\mathbf{p}|\psi_i\rangle|^2 \delta(E_f - E_i - \hbar\nu) \quad 3.11$$

It must be mentioned that the sudden approximation is in general in good agreement with experiments that are carried out with photons with energies in UV and soft x-rays range, where $|\mathbf{A}|^2$ factor can be disregarded..

The Fermi statistic provides information about the transition of the excited electron (by photon) from the material (initial state) to the vacuum level (final state), known as the photoexcitation process. However, the photoemission effect is far more intricate and encompasses numerous processes within the entire phenomenon. The most realistic description of photoemission is the *one-step model*, which characterizes the electron's exit from the material's surface as a single coherent process. In principle, this model allows for a quantitative interpretation of photoemission spectra, but it has been found to be very challenging to work with. Historically, the first model that attempted to describe photoemission was the three-step model proposed by Berglund and Spicer in 1964⁷⁶. Due to its simplicity compared to the *one-step model*, it is commonly used in the description of photoemission experiments.

3.2.2 Angle Resolved Photoemission Spectroscopy

In the previous section, we discussed how PES allows us to measure the energy of core-level electrons, where electrons from occupied states in the band structure are excited to unoccupied states above the vacuum energy, and their kinetic energy can be measured with a photoelectron analyzer (see the standard PES setup in the figure). However, as depicted in the figure, valence band electrons can also be probed. Moreover, electronic states in valence bands not only possess well-defined energy but also momentum (wave vector k). The energy and momentum of electrons within the material are directly connected with the photoelectrons emitted in photoemission through conservation laws. For the final state energy, we can rewrite equation 3.7.

$$E_f = h\nu - \phi - |E_{bin}| \quad 3.12$$

And the momentum final state k_f can be expressed

$$\mathbf{k}_f = \mathbf{k}_i \quad 3.13$$

In a standard PES experiment, the kinetic energy of the photoelectron is measured with respect to the analyzer and photon energy. To probe the energy and momentum of photoexcited electrons, ARPES was developed. This technique allows for the study of the relationship between the energy E of a single electron and its associated wave vector \mathbf{k} , termed $E(\mathbf{k})$, ultimately revealing the band structure. Due to the high energy resolution of photoemission analyzers and the advancement of excellent light sources, ARPES has gained enormous popularity in the study of solid-state properties in recent decades.

We have already discussed the basic theory of photoemission in the previous section, and we will now expand on this topic by elaborating on the three-step model, which is the most convenient and intuitive for describing ARPES. The foundation of this model lies in splitting the photoemission process into three consecutive steps:

1. Photoexcitation of the electron by a photon.
2. Transport of the photoexcited electron to the surface of solid.
3. Transmission of the photoelectron through the surface into the vacuum.

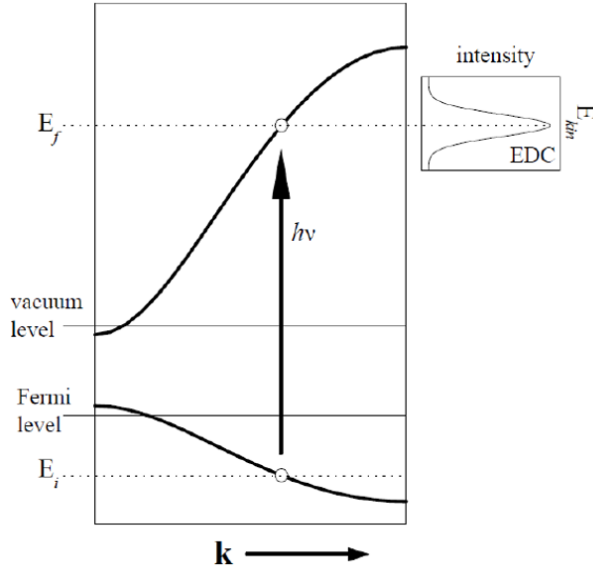


Figure 16 Scheme of the direct (vertical) transition between the initial and final states in the reduced zone⁷⁷.

In the first step the photon with energy $h\nu$ is illuminating the surface of the material and then, penetrates it. As the photon propagates within the material, there is a finite probability that it will be absorbed by a system electron. It's important to note that we are considering low-energy photons (below 1000 eV). With this assumption, we can neglect the wave vector of a photon, and we can treat the photoexcitation process as an optical or direct transition (illustrated as vertical transitions in Figure 16). Once the photon is absorbed, the electron in the initial state is excited to a higher energy state (final state) with the photon energy $h\nu$ while maintaining its momentum. From equation 3.13, we can write the in-plane and out-of-plane components

$$\begin{aligned} k_{\parallel,f} &= k_{\parallel,i} \\ k_{\perp,f} &= k_{\perp,i} \end{aligned} \tag{3.14}$$

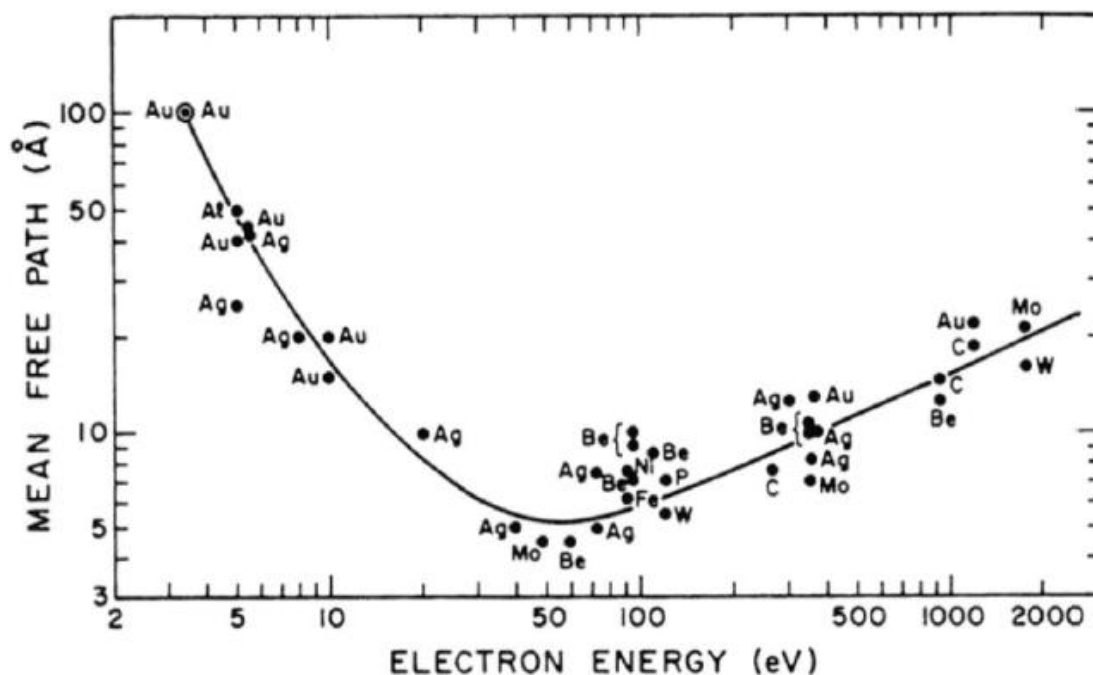


Figure 17 Universal curve for inelastic mean free path of electrons^{71,78}

The second step in the three-step model describes the propagation of the photoexcited electron towards the surface of the material. Due to strong Coulomb interaction in the solid state, the moving electron may undergo elastic and inelastic scattering multiple times before reaching the surface. Inelastic scattering processes contribute to the energy and momentum distribution observed in recorded photoemission spectra. The primary causes of inelastic scattering in solids are electron-electron interactions and site defects, both of which affect the *inelastic mean free path* (IMFP) of the excited electron. The IMFP is defined as the average distance between two independent inelastic events and plays a significant role in describing the specific information depth that can be obtained in a photoemission experiment. In principle, the inelastic mean free path depends on the energy of photons and the density of the material. In practice, the plotted curve exhibits a similar character for a vast array of elements and materials, and for a general description, we can utilize the so-called "universal curve" as depicted in Figure 17. According to Figure 17, the average inelastic mean free path for energies in the range of 20 to around 500 eV is below 1 nm, and this value increases for higher energies. Now, we can understand that photoemission spectroscopy is a surface-sensitive technique for the UV and soft X-ray ranges. An important observation from Figure 17 is that by simply altering the photon's energy, we can probe electrons from different depths within the sample.

In the final step, the photoexcited electron arrives at the surface and must exit the material. During this stage, the electron encounters a potential step at the surface, leading to scattering and diffraction (altering the trajectory of the electron). One consequence of diffraction is that the out-of-plane component of the photoelectron wave vector \mathbf{k}_\perp is not conserved, while the in-plane component \mathbf{k}_\parallel remains it

$$\begin{aligned} k_{\parallel,out} &= k_{\parallel,f} \\ k_{\perp,out} &\neq k_{\perp,f} \end{aligned} \quad 3.15$$

Energy maintain conserved

$$E_k = E_f \quad 3.16$$

Applying the law of conservation of energy

$$E_f - E_i = h\nu \quad 3.17$$

We can get the relation

$$E_{kin} = \frac{\hbar^2}{2m} (k_{out}^2) = \frac{\hbar^2}{2m} (k_\parallel^2 + k_\perp^2) = E_f - E_{vac} \quad 3.18$$

where E_{vac} is associated with work function ϕ in the relation $\phi = E_{vac} - E_F$ (E_F is the Fermi level).

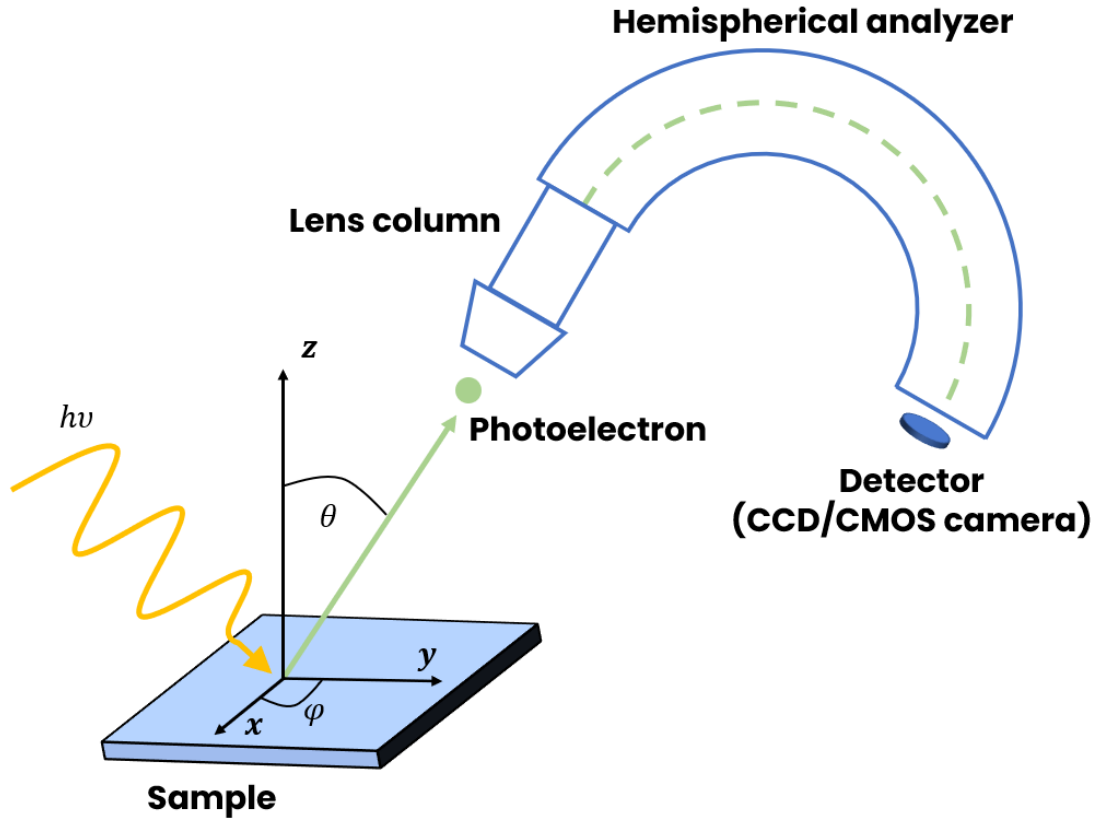


Figure 18 Hemispherical electron analyzer and the working principle of the standard ARPES.

The standard geometry for ARPES is illustrated in Figure 18. A hemispherical analyzer collects the photoelectrons ejected from the material with a specific angular distribution. By measuring their kinetic energy and emission angle, we can define k_{out} as function of θ and φ . Given that $k_{out}^2 = k_{\parallel}^2 + k_{\perp}^2$, $\mathbf{k}_{\parallel} = (k_x, k_y)$ and $\mathbf{k}_{\perp} = k_z$ from 3.15

$$k_x = \frac{1}{\hbar} \sqrt{2mE_{kin}} \sin \theta \cos \varphi \quad 3.19$$

$$k_y = \frac{1}{\hbar} \sqrt{2mE_{kin}} \sin \theta \sin \varphi \quad 3.20$$

$$k_{\parallel} = k_x + k_y = \frac{1}{\hbar} \sqrt{2mE_{kin}} \sin \theta \quad 3.21$$

$$k_{\perp} = k_z = \frac{1}{\hbar} \sqrt{2mE_{kin}} \cos \theta \quad 3.22$$

and binding energy E_{bin} is defined as

$$E_{bin} = h\nu - \phi - E_{kin} \quad 3.23$$

Summarizing, from eq. 0.14 and 0.15 we can write initial state

$$\mathbf{k}_{x,i} = 0.512\sqrt{E_{kin}} \sin \theta \cos \varphi \quad 3.24$$

$$\mathbf{k}_{y,i} = 0.512\sqrt{E_{kin}} \sin \theta \sin \varphi \quad 3.25$$

This provides a complete picture of the 2D electronic structure of a material that can be measured (binding energy and in-plane component of momentum) with ARPES. Unfortunately, 3D systems cannot be treated in the same way because the \mathbf{k}_{\perp} component of the wave vector is not conserved during surface emission in the three-step model. This means that \mathbf{k}_{\perp} cannot be directly extracted from E_{kin} and emission angles. To explicitly express the out-of-plane component of momentum, the free-electron approximation must be employed. The assumption of the free-electron model is that electrons can move freely within an additional potential, V_0 , known as *inner potential*. From the first step, we can write

$$E_f = \frac{\hbar^2}{2m} (k_{\parallel}^2 + k_{\perp}^2) - V_0 \quad 3.26$$

Now, we can express the initial state of out of plane component by solving above equation for $k_{\perp,f}$

$$k_{z,i} = \sqrt{\frac{2m}{\hbar^2} (h\nu - \phi - E_{bin} + V_0) - k_{x,i}^2 - k_{y,i}^2} \quad 3.27$$

The inner potential can be experimentally determined by measuring the electronic structure of the material with different excitation energies and then correlating them with theoretical results. The free-electron approximation is widely used, even if the final states do not exhibit free electron behavior, because this approximation is easy to work with and generally produces correct results.

3.2.3 X-ray Absorption Spectroscopy

In the 1970s and 1980s, XAS emerged as the pioneering experimental technique utilizing synchrotron radiation. XAS stands as a well-established analytical method, elucidating the structural and electronic properties of materials at both the atomic and molecular levels. This technique finds applications across nearly all scientific fields, including solid-state physics, materials science, chemistry, and biology.

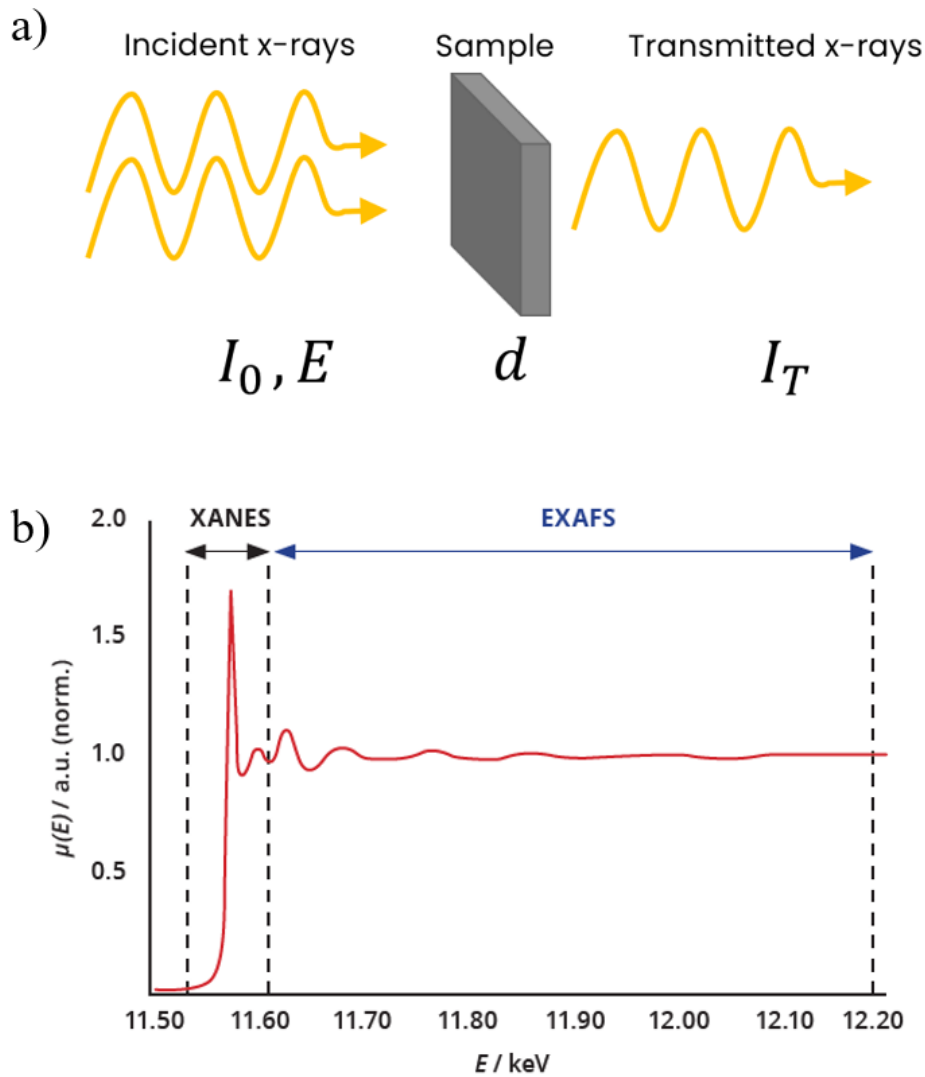


Figure 19 Standard XAS measurement setup a) and b) is a typical XAS spectrum with highlighted the near-edge structure (XANES) and extended absorption fine structure (EXAFS)⁷⁹.

The standard XAS spectrum is obtained by measuring the intensity of the incident light I_0 , and the intensity of the light transmitted I_T through the sample Figure 19 a). According to the Lambert-Beer Law, the transmitted intensity can be expressed as

$$I_T(d) = I_0 e^{-\mu(E)d} \quad 3.28$$

Here, $\mu(E)$ represents the energy-dependent linear absorption coefficient. This coefficient changes smoothly as a function of photon energy, depending on sample density ρ , atomic number Z , and atomic mass A .

$$\mu(E) = \frac{\rho Z^4}{AE^3} \quad 3.29$$

However, by altering the energy of the incident light illuminating the sample surface, we can match the energy of the core electron, enabling the emission of a photoelectron. During this process, a core-hole is created, and $\mu(E)$ undergoes a transition from a smooth to a sharp course, known as the absorption edge (Figure 19 b). This edge can be divided into three parts: the pre-edge region, the near-edge structure (XANES), and the extended absorption fine structure (EXAFS). The explanation of the absorption edge structure lies within the quantum theory. According to perturbation theory, the transition between the core level and the final state is described by the equation 3.8, where the perturbation operator Δ represents the interaction causing the transition - the x-ray photon. Together with the delta factor (density of state), Δ induces a modulation of the absorption coefficient, creating the X-ray absorption fine structure (XAFS). The many-body problem considered here, where all electrons can interact with the x-rays, is complex, and for practical purposes, an approximation is often employed. Using the one-electron approximation along with the dipole approximation, we can express the absorption coefficient as follows

$$\mu \propto |\langle f | \varepsilon \cdot \vec{r} | i \rangle|^2 \rho \quad 3.30$$

where ε describes the x-rays polarization vector. The dependence of the matrix element on the polarization of incident X-ray light is of great significance in the case of structurally ordered materials such as single crystals. Typically, linear and circular polarizations are used for synchrotron measurements, allowing for the investigation of dichroism.

Dichroism is the optical property of a material to exhibit differential absorption of linearly polarized light (linear dichroism) or circularly polarized light (circular dichroism). In the case of circular dichroism and when a magnetic field is introduced to the system, we refer to it as magnetic circular dichroism (in the X-ray range, X-ray Magnetic Circular Dichroism, XMCD). The XMCD signal can be observed for magnetic materials (ferro- and ferrimagnets).

The basic theory of XMCD can be described in terms of the magnetic dipole transition moments for left and right circularly polarized light, denoted as μ_L and μ_R respectively. The difference in absorbance, known as the XMCD signal $\Delta\mu$ can be expressed as

$$\Delta\mu = \mu_L - \mu_R \quad 3.31$$

In the case of transition metals, a strong signal originates from the L₂ and L₃ edges (transition from p to d orbitals) - electrons from the d orbitals are the main contributors to magnetism in this group of elements. The mechanism of XMCD can be explained based on the p states in transition metals. These states are split into 2p_{1/2} and 2p_{3/2} by spin-orbit coupling, where l and

s are coupled either parallel or antiparallel. Circularly polarized x-ray light selectively excites the 2p electrons to the unoccupied valence band in a spin-selective manner (following the selection rule for orbital angular momentum). Due to the coupling of l and s (antiparallel for $2p_{1/2}$ and parallel for $2p_{3/2}$), the process of transferring electrons to the unoccupied valence band becomes spin-polarized. Since the transition dipole moment conserves electron spin, electrons with spin up can only occupy free spin up states. Data from XMCD allows us to obtain information about the spin magnetic moment and the orbital magnetic moment, enabling measurements of magnetic anisotropy energy. These measurements are particularly effective for thin materials, where the contribution of the orbital magnetic moment to the total magnetization is significant.

3.2.4 Circular Dichroism – ARPES

Dichroism can be described as a process in which the photocurrent intensity depends on the polarization of light, stemming from the fact that photoemission is an optical transition process. There are two main effects that characterize dichroism in photoemission. Firstly, there is circular dichroism in angular distribution (CDAD), where certain combinations of total angular momentum j and z -component m_j are preferentially excited by circularly polarized light. This process also involves the photoelectron diffraction of nearby atoms. Secondly, when considering the spin-orbit splitting of core levels, magnetic circular dichroism (MCD) must be considered. Due to the spin-orbit splitting, the probed system exhibits a relatively long-range magnetic order compared to the wavelength of the illuminating electromagnetic wave (UV or soft X-rays). It has been observed that in such systems, the intensity of photoemission peaks varies with changes in polarization from right circular to left circular. The result of dichroic measurement can be expressed as

$$I_{dich} = \frac{I_{RCP} - I_{LCP}}{I_{RCP} + I_{LCP}} \quad 3.32$$

where I_{RCP} and I_{LCP} are the photoelectron intensity spectra collected with right and left circularly polarized light, respectively. Circularly polarized light can also probe the spin-polarized electrons in the valence and conduction bands of semiconductors, leading to the development of the idea of CD-ARPES. To delve deeper into the circular dichroism (CD) effect, we need to take another step into photoemission theory and introduce the basics of dipole selection rules that govern this process.

The dipole selection rules allow us to predict electronic transitions based on the symmetry of the electronic wave functions involved in the photoexcitation process (the first step in the three-step model). We will begin with the sudden (dipole) approximation version of Fermi's Golden Rule, 3.8 , and introduce the photoemission matrix element M_{if}

$$M_{\psi_i\psi_f} \propto \langle \psi_f | \mathbf{A} \cdot \mathbf{p} | \psi_i \rangle \quad 3.33$$

The polarization of the photon can be formulated as $\epsilon \parallel \mathbf{A}$, and under this condition, we can write

$$M_{\psi_i\psi_f} \propto \langle \psi_f | \epsilon \cdot \mathbf{p} | \psi_i \rangle \quad 3.34$$

This presentation is called the velocity form of the dipole matrix element and can further be rewritten as the so-called length form

$$M_{\psi_i\psi_f} \propto \langle \psi_f | \epsilon \cdot \mathbf{r} | \psi_i \rangle \quad 3.35$$

The polarization vector ϵ can describe various polarizations of light (linear, circular, and elliptical). From this standpoint, the matrix element can be calculated for selected symmetries of the wave function, and the dipole selection rules can be formulated. It can be determined that the matrix element can be nonzero only for particular relations of the orbital quantum number l and the magnetic quantum number m of the initial and final states, which form the basis of the selection rules.

We have already mentioned that the dipole selection rules allow us to predict electronic transitions based on the electronic wave functions. This can be easily understood in the atomic picture, where we can express the first rule as

$$\Delta l = \pm 1 \quad 3.36$$

which refers to the change in l carried by the photon. The second rule depends on the polarization of the light

$$\Delta m = 0, \pm 1 \quad 3.37$$

where $\Delta m = 0$ for linear polarization and $\Delta m = +1$ for right circular polarization and $\Delta m = -1$ for left circular polarization. According to the selection rules the electron from s orbital can only be transmitted to the p orbital and electrons from p orbital can be emitted to s and d orbital. For a more illustrative example, let's consider the excitation of the 2p level

$$\begin{aligned} p &\rightarrow d \text{ for } \Delta l = +1 \\ p &\rightarrow s \text{ for } \Delta l = -1 \end{aligned} \quad 3.38$$

It's worth noting that due to spin-orbit coupling, atomic levels split. Consequently, the total angular momentum $J = L + S$ (where L is total orbital momentum and S is total spin momentum) becomes a good quantum number. As a result, the p level splits into $p_{3/2}$ and $p_{1/2}$ and with linearly polarized light, the allowed transitions are

$$\begin{aligned}
 p_{3/2} &\rightarrow d_{3/2} \\
 p_{1/2} &\rightarrow s_{1/2} \\
 p_{-1/2} &\rightarrow s_{-1/2} \\
 p_{-3/2} &\rightarrow d_{-3/2}
 \end{aligned}
 \tag{3.39}$$

And for circular polarized light, the allowed transition are for $\Delta m = +1$

$$\begin{aligned}
 p_{3/2} &\rightarrow d_{5/2} \\
 p_{1/2} &\rightarrow d_{3/2} \\
 p_{-1/2} &\rightarrow s_{1/2} \\
 p_{3/2} &\rightarrow s_{-1/2}
 \end{aligned}
 \tag{3.40}$$

and for $\Delta m = -1$

$$\begin{aligned}
 p_{3/2} &\rightarrow s_{1/2} \\
 p_{1/2} &\rightarrow s_{-1/2} \\
 p_{-1/2} &\rightarrow d_{-3/2} \\
 p_{-3/2} &\rightarrow d_{-5/2}
 \end{aligned}
 \tag{3.41}$$

We have to consider that the light dipole operator interacts only with the orbital part of the electronic wave function and does not directly interact with the electron spin. However, the spin is tied to specific orbitals by spin-orbit interaction, and as a result, spin-polarized photoelectrons can be excited even from nonmagnetic systems. This process is called *optical spin-orientation* and forms the basis of all magneto-dichroic phenomena observed in photoemission and absorption spectroscopy. ARPES combined with synchrotron radiation as a light source, gives us the possibility to selectively measure electronic transitions in both magnetic and nonmagnetic materials. This makes it one of the most powerful experimental tools for studying dichroic phenomena.

3.3 Experimental setup and Methodology

3.3.1 Radiation sources

To complete the PES experiment, a suitable light source is required. Historically, the first source of monochromatic light used in photoemission experiments, by Siegbahn, was the X-ray tube. The utilization of X-ray sources led to the development of X-ray Photoemission Spectroscopy (also known as Electron Spectroscopy for Chemical Analysis (ESCA)), for which Siegbahn was awarded the Nobel Prize in Physics in 1981. Core level photoemission, primarily measured by XPS, stands as one of the most powerful qualitative methods in condensed matter physics. While X-rays can also excite valence states, probing valence electrons with standard X-ray tubes (e.g., with Mg or Al anodes) is time-consuming due to their emission lines being above 1 keV. The parameter that determines this is the photoionization cross section, which will be discussed further later in this section.

An alternative light source for investigating valence states is gas discharge lamps, particularly Helium lamps. Helium lamps can produce He I (21.2 eV) and He II (40.8 eV) emission lines via gas discharge. Low-energy, monochromatic ultraviolet light is ideal for probing valence states because the emitted radiation energies are near the photoionization threshold for these states. UV lamps, as stable and high-resolution sources, are integral parts of all laboratory ARPES systems. To fully exploit photoemission experiments and comprehensively understand the measured sample or system, it is advantageous to use both X-ray and UV sources. Fortunately, a more versatile light source exists – synchrotron radiation. Because synchrotron radiation plays an enormous role in my thesis, it deserves a brief description in its own section.

3.3.2 Synchrotron radiation

The history of synchrotron radiation is intertwined with attempts to accelerate particles, a process that began in the 1950s. Initially, there was no understanding of why accelerated particles had such a short lifetime in accelerators. However, physicists eventually realized that very fast charged particles lose energy when they interact with an external magnetic field. This phenomenon is known as synchrotron radiation⁸⁰.

A more precise definition of synchrotron radiation is when charged particles (such as protons or electrons) are accelerated to relativistic speeds and exposed to an external magnetic field, causing their trajectory to change, and emitting electromagnetic waves in the direction of their motion⁸¹. Synchrotron light is produced by electron storage rings, known as synchrotrons. An

electron accelerator is composed of an injector system (linear accelerator), vacuum chambers, bending magnets, and radiofrequency (RF) cavities. The bending magnets (dipoles) maintain the electrons in a closed trajectory by applying a Lorentzian force perpendicular to the electron velocity vector

$$\frac{d\mathbf{p}}{dt} = e \left(\mathbf{E} + \frac{\mathbf{v} \times \mathbf{B}}{c} \right) \quad 3.42$$

where \mathbf{p} is electron momentum, e is electron charge and \mathbf{v} is electron velocity and \mathbf{E} and \mathbf{B} are the electric and magnetic fields, respectively. Each interaction of an electron with a dipole magnet emits synchrotron radiation. The consequence of this process is energy loss by electrons, which must be compensated to maintain a stable trajectory of particles in the storage ring. This compensation is achieved in the RF cavities, where an electric field is introduced in phase with the moving electrons, accelerating them in the longitudinal direction. As a result, electrons can circulate for hours or even days at relativistic speeds in the storage ring.

Every bending magnet serves as a source of electromagnetic waves, which can be collected by experimental instruments called beamlines built around the synchrotron. In modern facilities (3rd generation), not only do bending magnets serve as a source of light, but other magnetic systems are also placed in the storage ring, such as undulators (and wigglers). The insertion devices (ID), including undulators and wigglers, are constructed with magnetic periodic structures that force electrons to undulate in the transverse direction.

Synchrotrons are constructed with tens of bending magnets that control the electron trajectory in the storage ring while also emitting light. However, their multifunctionality limits their flexibility in generating peak photon energy, which is constrained by their magnetic characteristics. To enhance the potential of the storage rings, insertion devices (ID) were developed. These ID devices are placed between two sections of bending magnets (straight sections) in the accelerator, and their sole purpose is to emit light. The main benefits of using these devices include:

- Control of the peak photon energy emission and polarization of light through the design of the magnetic structure.
- Increase in the intensity of emitted light due to the electron wiggling "inside" the device in relation to the bending magnet.
- Increase in spectral brightness.

One of these additional magnetic structures, undulators, ensures exceptional control of the peak photon energy and polarization. Undulators are built from two rows of permanent magnetic structures with a set periodicity. By controlling the gap opening and longitudinal positions between the two rows of magnetic structures in the undulator, the magnetic field is determined, and light with specific photon energy and polarization is emitted.

The polarization of the light emitted by accelerated electrons is one of the most important parameters that scientists can utilize in their research. The radiation emitted from a bending magnet is mostly linearly polarized. To understand this, we must realize that the accelerated electron is bent in the horizontal plane, and the electric field of the emitted electromagnetic wave (synchrotron radiation) is parallel to this plane. This consideration only applies when we observe electrons in the horizontal plane. Of course, photons are produced in a cone, and the perpendicular component of the electric field is also present above and below the horizontal plane. We can define the degree of linear polarization P_L as a function of the horizontal I_{\parallel} and vertical component I_{\perp} of the electromagnetic wave

$$P_L = \frac{I_{\parallel} - I_{\perp}}{I_{\parallel} + I_{\perp}} \quad 3.43$$

The horizontal and vertical components of the electric field are also constantly shifted by a factor of $\frac{\pi}{2}$ resulting in the production of elliptically polarized light. If the phase shift is $+\frac{\pi}{2}$ it is called elliptically right-polarized, and if the phase is $-\frac{\pi}{2}$ it is called elliptically left-polarized. The degree of circular polarization can be represented as

$$P_C = \frac{I_R - I_L}{I_R + I_L} = \frac{\pm 2\sqrt{I_{\parallel}I_{\perp}}}{I_{\parallel} + I_{\perp}} \quad 3.44$$

where I_R and I_L are the intensities of right and left polarized light, respectively, and the sign is determined by the phase.

The availability of various polarizations of light across a wide range of photon energies is one of the most important features of synchrotron radiation. This feature has proven to be very useful in studying the orbital and spin angular momentum of both magnetic and nonmagnetic materials through absorption and photoemission spectroscopy.

3.3.3 Beamlines

From all above considerations the synchrotron radiation and photoemission spectroscopy (ARPES and XPS) emerges as perfect combination to study electronic and

magnetic properties of complex quantum materials. The concept and technical realization of such as powerful tool is met at the beamline. Generally, the beamlines are constructed from three main parts: the source, the optical part that focusing the beam and the end station,. and they are built around the storage ring facilities.

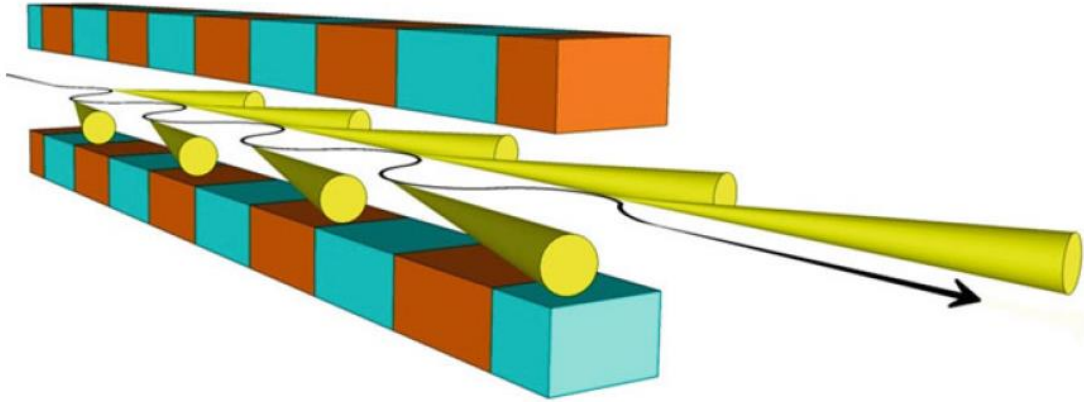


Figure 20 Radiation beam emission from the magnetic insertion device such as wigglers or undulators⁸¹.

Starting from the source, there a few types that can be used (and were mentioned before in the theoretical section devoted to synchrotron radiation): bending magnets and the IDs that can further split to the wigglers and the undulators. The undulators are two jaws periodic magnets structures that can be installed between two bending magnets sections (the straight section). Electron passing through the undulators magnetic field is force to oscillate perpendicular to the direction of their motion and each of the wiggle of an electron is source of synchrotron light, Figure 20.

One of the parameters that differ wigglers from undulators is K parameter defined as

$$K = \alpha\gamma \quad 3.45$$

where α is an wiggling angle and $\frac{1}{\gamma}$ is natural angular aperture of synchrotron radiation. We can show that value of K for an electron propagating in the IDs magnetic field is

$$K = \frac{e}{2\pi mc} \lambda_0 B_0 = 0.934 \lambda_0 B_0 \quad 3.46$$

where λ_0 is undulator or wiggler magnetic period and B_0 is their magnetic field. For wigglers the value of K is much higher than 1 ($K \gg 1$) and this implicated that α is much wider than natural angular aperture and this case interference effect between the magnetic poles can be neglected. This is not the case in undulators where K is much smaller than 1 ($K \ll 1$) and interference effect occurs between the emitted light and moving electrons. Finally, radiation is

emitted in the narrow cone with angle θ on the axis of the undulator and the constructive interference occurs at the wavelength λ , that is depend of parameter K

$$\lambda = \frac{\lambda_0}{2\gamma^2} \left(1 + \frac{K^2}{2} + \gamma^2 \theta^2 \right) \quad 3.47$$

In the undulators beside the fundamental wavelength also higher harmonics (shorter wavelengths) are generated

$$\lambda_n = \frac{\lambda}{n} \quad 3.48$$

and their number and intensity are bond (it increase) with K (only odd harmonics are emitted on the axis of insertion device). Next important factor is, that K is dependent on B_0 . It follows from this dependence that λ is tunable by value of magnetic field that can be continuously changed by gap opening between two separate undulator magnetic jaws. With this features undulators are efficient sources of UV and x-ray light and are commonly used in purpose of photoemission beamlines e.g. PHELIX or URANOS beamlines at the SOLARIS Synchrotron Radiation Centre⁸².

3.3.4 PHELIX and URANOS beamlines

The PHELIX undulator beamline is installed at the BM06 straight section of SOLARIS, the third-generation light source with an electron energy of 1.5 GeV and a current of 500 mA. The beamline is designed for conducting experiments with ultra-high vacuum PES and XAS in the soft X-ray range, and Near Ambient Pressure XPS (NAP-XPS) will be available at the second branch in the future.

The soft X-ray PES and XAS end station is aimed at investigating the electronic structure of various types of materials, ranging from highly ordered crystalline solids to amorphous phases like ceramics, glass, or minerals. The availability of numerous techniques makes this end station a powerful and unique tool for studying very complex systems. PES experiments can be conducted using methods such as ARPES, CD-ARPES, Spin-ARPES, and XPS. The SPECS PHOIBOS 225 energy analyzer with a deflector system and CMOS camera allows for the collection of photoemission data with an energy resolution better than 2 meV and an angle resolution of 0.1°. Absorption spectra can be obtained using TEY and TFY. The combination of PES and XAS experiments is met in a method called Resonant-PES (ResPES).

The source of the PHELIX beamline is the APPLE-II type undulator, which delivers soft X-rays with the following parameters:

- Photon energy range from 40 eV up to 1800 eV (horizontal polarized light),
- Linear (horizontal and vertical) and Circular (left and righthanded) polarized light,
- The ultimate resolving power $E/\Delta E$ 10 000 in 50 to 1500 eV energy range,
- Flux range from $\sim 10^{12}$ ph/s for 100 eV and $\sim 10^{11}$ ph/s for higher photon energies, above 300 eV.

The optical design of the PHELIX beamline is based on a classic plane-grating monochromator (PGM) setup operating with collimated beam. The focusing and re-focusing mirrors system allow for obtaining the beam size spot on the sample of 120 μm x 40 μm (h x v).

The URANOS beamline is much similar to the PHELIX in terms of its primary experimental technique, PES, and radiation source, the APPLE II undulator. The beamline is installed at the BM05 straight section of SOLARIS and specializes in UV and soft X-ray (8-100 eV) ARPES. The central component of the end station is the SCIENTA DA30L photoelectron analyzer with a deflector system, boasting an energy resolution of 1.8 meV and an angle resolution of 0.1°. The combination of high energy resolution with low energy photons provides remarkable capabilities in defining the chemical properties and valence band electronic structure of materials such as semiconductors, topological materials, and spintronic materials.

The optical design of the URANOS beamline is based on a PGM and normal incident monochromator (NIM), both working with collimated beam. The focusing and refocusing mirror system allows for obtaining a beam spot size on the sample of 60 μm x 150 μm (h xv).

Both beamlines have preparation chambers in their vacuum systems, allowing for the in-situ deposition of thin layers of elements, e.g. transition metals (pressure during deposition at level of 10^{-10} mbar). In the both cases, deposition rate can be measured by a quartz balance with resolution of 0.01 Å. The quality of the layers can be assessed based on LEED measurements. All available preparation techniques enable the study of surface properties and electronic structure under the influence of external (environmental) factors.

3.3.5 Sample description and preparation process

The single crystal of Bi_2Te_3 was fabricated by the MaTeCK company in Julich (in 2019). The sample was grown using the Molecular Beam Epitaxy technique by deposition on a silicon substrate, Si(111), under UHV conditions at a level of 10^{-9} mbar.



Figure 21 Omicron flag style holder compatible with the PHELIX and URANOS systems. Bi_2Te_3 single crystal is placed in the middle of the holder and attached by the UHV glue.

The sample thickness was 1 mm, with a total surface area of 100 mm^2 ($10 \times 10 \text{ mm}$). During the project, the sample was divided into 6 parts, with the majority being used to investigate the effect of thin Fe layers on the electronic structure properties, with only one sample being characterized under Co deposition. The deposition of the elements (Fe and Co) during the project was conducted via PREVAC style electron beam evaporation in ultra-high vacuum ($\sim 10^{-10}$ mbar). Fe and the Co were deposited from wires made of pure elements with the purity of 99.99% (manufactured by PI-KEM). The deposition parameters were optimized for quartz crystal microbalance readings - the deposition rate was set at $0.3 \text{ \AA}/\text{min}$. Further, the sample electronic structure was investigated mostly by ARPES, XPS and XANES. All measurements of photoelectron spectroscopy and absorption spectroscopy were conducted using synchrotron radiation (at the NSRC SOLARIS in Krakow). The research was carried out at the URANOS and PHELIX beamlines. Due to characteristic layered structure of Bi_2Te_3 , each sample could be prepared multiple times via exfoliation under UHV conditions (the exfoliation process was conducted under pressure of 10^{-8} mbar in the LoadLock chambers). Each sample was mounted onto flag-style holders (OMICRON) using conductive Epoxy adhesive (EPO-TEK®) which is resistance for ionizing radiation.

Chapter 4 Results and Discussion

In this chapter the results and discussion of the experimental findings are presented. Section 4.1 focuses on pristine Bi_2Te_3 , characterized using XPS, ARPES, and CD-ARPES to analyze OAM. Sections 4.2 and 4.3 investigate Bi_2Te_3 covered with Fe and Co layers, respectively, using XPS, ARPES, and CD-ARPES to examine changes in the electronic structure and magnetic properties induced by the transition metal layers. To facilitate a clearer understanding of the experimental findings and provide context for the phenomena discussed in this chapter, several topics related to doping and defects, applied techniques limitations (such as IMFP and penetration depth), and topological insulator-related phenomena were highlighted through brief theoretical descriptions.

4.1 Pristine Bi_2Te_3

To study the electronic structure of topological materials is very challenging due to the many variables that can differ from experiment to experiment, even for the same sample. The surface preparation process, material evaporation, and influence of the measurement, especially when using synchrotron radiation, are perhaps the most important technical parameters, but they are not the only factors that could impact the acquired data. Significant effort has been put into characterizing the electronic structure of the pristine sample to establish a well-defined starting point. In general, I have mainly focused on photoemission spectroscopy (XPS and ARPES) to characterize the sample's chemical and electrical properties. XPS is a widely used method to study surface physics and chemistry. Element identification, chemical state information, and surface sensitivity are a few of the most important features of this technique. Especially for 2D materials, thin layers systems, or quantum materials where understanding the surface electronic structure and surface chemical composition is highly desired.

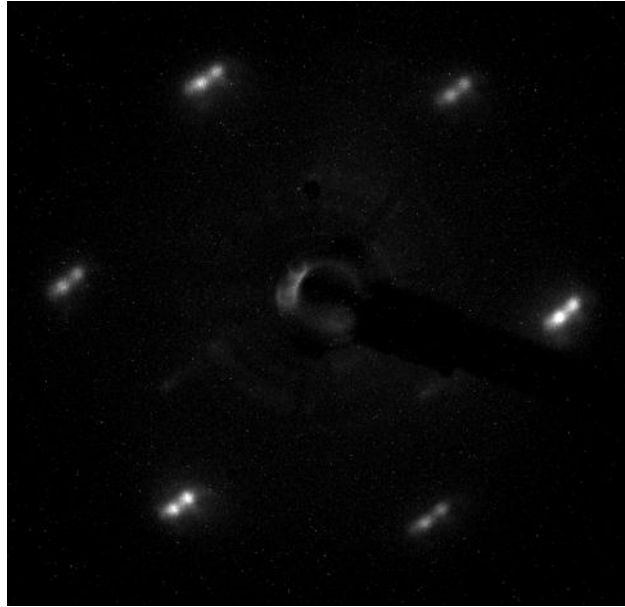


Figure 22 LEED pattern measured for pristine Bi₂Te₃ at the electron energy of 69 eV. The double bright spots can implicate that the surface of the TI absorb the residual gas molecules and the superstructure could form at the very top of Bi₂Te₃.

Unfortunately, we lack some data from the LEED technique, but this was mainly due to technical issues that I will not delve into. Only a few images were collected of the pure material during the experiments to determine whether the material would retain its hexagonal lattice structure after exfoliation, Figure 22. In XPS study, we heavily focused on the core levels near the valence band, specifically Te4d and Bi5d. This focus was driven by the fact that these levels can be reach even with very low photon energies. By combining these results with those obtained at higher photon energies, we achieve a kind of deep profile chemical information⁸³. This information has proven to be very interesting for understanding surface and interface chemistry of the material. A significant part of this thesis is based on ARPES data. The direct observation of surface states and the valence band electronic structure is a major advantage of this technique. Proper surface preparation plays a very important role and affects the quality of the acquired data. Several experiments had to be performed using this method to establish a good starting point. Another advantage of ARPES is the direct observation of OAM, which could play a tremendous role in modern spin-based surface physics in the coming years. In the first part of Chapter 4, I will focus on the data (XPS and ARPES) measured for the pristine single crystal of Bi₂Te₃.

4.1.1 XPS studies

All XPS studies of the single crystal Bi₂Te₃ were carried out at the PHELIX beamline in the SOLARIS synchrotron facility. Measurements at the PHELIX beamline were performed

over a wide photon energy range, starting from 100 eV and extending up to 1000 eV. The sample beam spot size is in the range of 150 μm in the horizontal direction and 50 μm in the vertical direction. The SPECS PHOIBOS 225 hemispherical analyzer, with an energy resolution below 2 meV, was found to be a perfect tool for studying the electronic structure. The collected XPS data were analyzed and plotted using CasaXPS and OriginPro software. All the XPS data are energy calibrated to the Fermi level, and for a few specific photon energies, the Au 4f core levels were also included in the energy calibration. The single crystal of Bi_2Te_3 , provided by MaTecK company, with dimensions of 10 x 10 x 1 mm, was later cut into smaller pieces for two sets of experiments: time-resolved ARPES⁶³ and synchrotron studies. Samples were mechanically exfoliated several times in air and then transferred into the vacuum load-lock chamber, where they were exfoliated again in an ultra-high vacuum regime of 10^{-7} - 10^{-8} mbar to avoid oxygen contamination. Samples prepared this way were rapidly transferred into the analyzer chamber to start measurements. Measurements were carried out under UHV conditions of 1×10^{-10} mbar. In the first step, the crystal surface quality (using ARPES) and chemical composition (using XPS) were investigated. In Figure 23, the XPS survey data collected for 850 eV photons are presented, referring to the pristine surface of Bi_2Te_3 . In terms of XPS, if I did not observe the presence of O1s and C1s core levels and did not detect satellites in the Bi4f and Bi5d core levels, I considered the material to be clean (in terms of environmental contamination) and thus pristine. The high photon energy of 850 eV appears to be optimal in terms of flux, which remains sufficiently high for the PHELIX beamline. From a chemical state detection standpoint, it provides access to the main Bi (Bi4d, Bi4f, and Bi5d) and Te (Te3d and Te4d) transitions, Figure 26. Additionally, environmental components such as N1s, O1s, and C1s are detectable within this energy range. Further considerations within the thesis will elaborate on the main transitions of Fe and Co (700 to 800 eV), which also fall within this energy range.

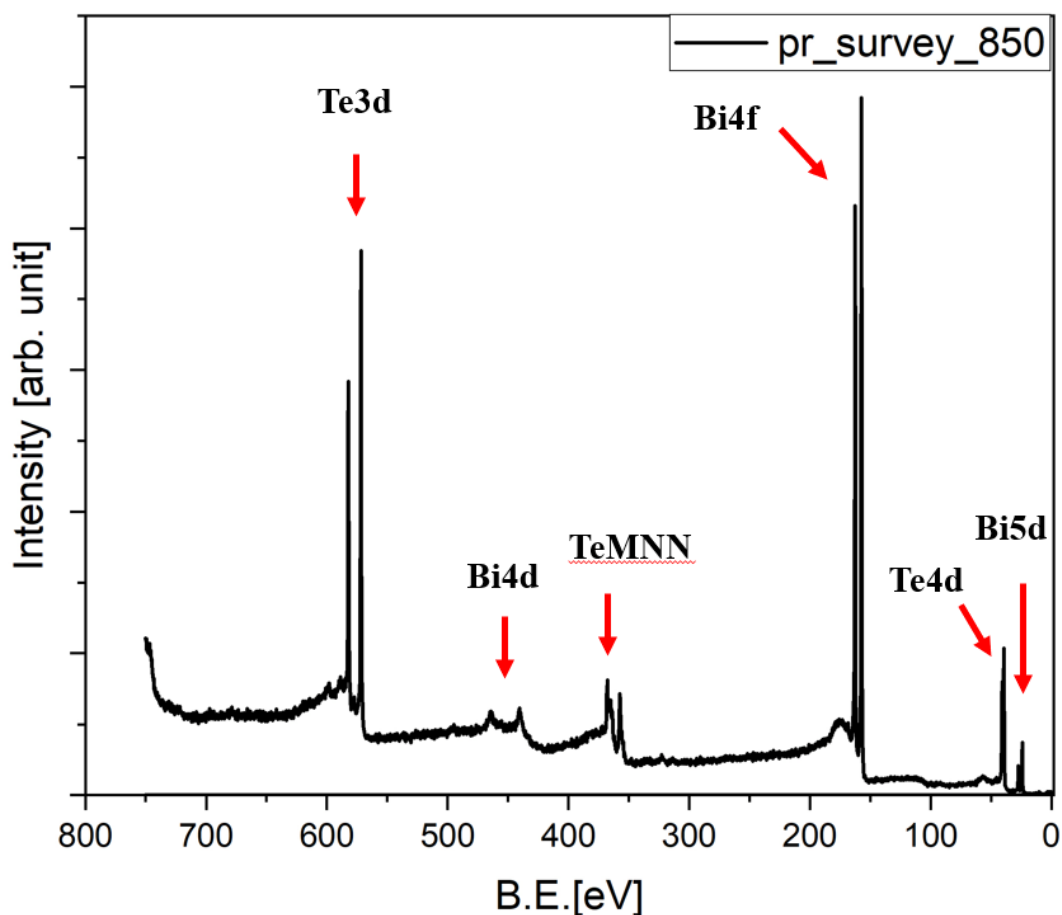


Figure 23 XPS survey measurement of the Bi₂Te₃ single crystal taken for photon energy of 850 eV.

However, the main goal was to study the VB electronic structure and achieve high surface sensitivity, which requires lower photon energies (according to Figure 17). The optimal energy range for XPS was determined experimentally to be between 100 and 200 eV, providing access to Te4d and Bi5d transitions. The analysis of these core levels shows that the maximum of the Te4d_{5/2} is located at a binding energy of 39.38 eV, and the maximum of the Bi5d_{5/2} is located at a binding energy of 24.37 eV, as shown in Figure 24. The analysis (spectra fitted by Gaussian/Lorentz lines) was performed for core levels collected with photon energy of 115 eV. These values were compared with reference data from an X-ray lamp for the same material⁸⁴. For the Te4d core level, there is an energy shift in the range of 20 meV, and for the Bi5d core level, the energy shift is around 70 meV. The resolution of the beamline is expected to be better than 50 meV for this beamtime, and the spectra were collected with a 10 or 40 meV energy step.

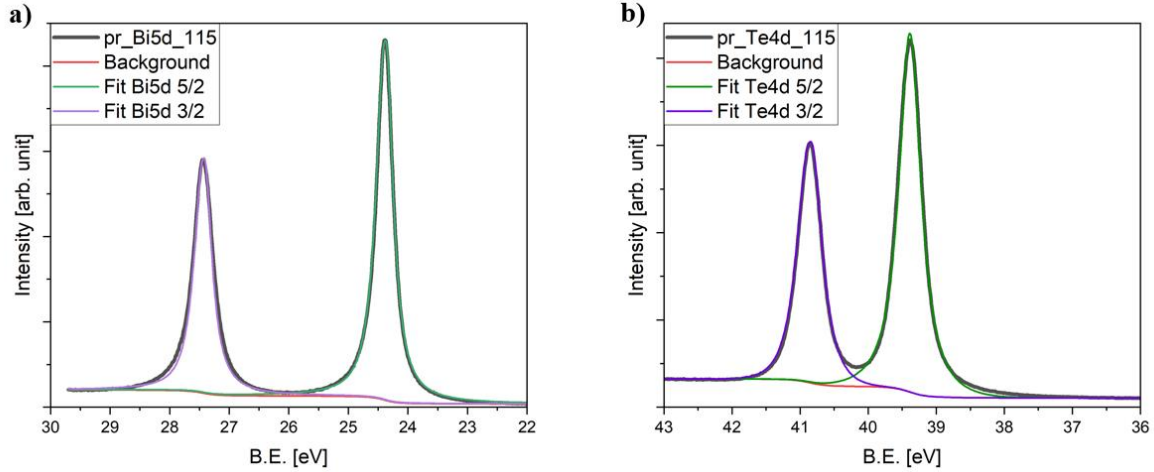


Figure 24 XPS data collected for Bi_2Te_3 . a) Bi5d and b) Te4d core levels analysis.

As presented in Figure 25, a set of data was collected for several excitation energies up to 850 eV. Differences in the binding energy positions and the peak-to-peak ratio can be easily observed, Table 3. The peak-to-peak ratio for d-orbitals should be 3:2 (1.5). However, this ratio can be affected by factors such as experimental conditions, including the photoionization cross-section, IMFP, or spectrometer transmission functions. In this discussion, the peak-to-peak parameter is presented because it was found that the ratio changes during scanning with different excitation energies. It is expected that this behavior, where the ratio varies with photon energy, is related to imperfect changes in the spectrometer's transmission functions. This energy discrepancy may be due to several factors, whether related to the sample or to the research method and the measurement itself. According to the analysis of the Te4d core level revealed that the line is slight asymmetric towards smaller binding energy, that can be concluded as the single crystal is overdoped with Te atoms. This can be easily explained by the fact that the crystal was grown using MBE technique. In this process, to achieve a very high-quality single crystal, it has to be grown in an overpressure of Te to avoid desorption of the Te atoms from the crystal structure during growth⁸⁵ (the growth process is run in the high temperature regime, substrate is heated to around 400 °C, which enhances the desorption of the atoms of Te). At this point, it is worth reminding that the single crystal of Bi_2Te_3 is a layered material, consisting of QLs with the stacking sequence Te(1)-Bi-Te(2)-Bi-Te(1), where the QLs are connected by vdW bonds. Within this interspace, adatoms can be localized and expand this space, potentially leading to modifications in the electronic structure⁸⁶ like band splitting and bandgap expansion. Besides the aspects of the samples, there are technical factors that cannot be neglected and often cannot be excluded. The first is the photon flux, which changes as the photon energy changes. For the Phelix beamline, the flux is in the range of 10^{12} ph/s for low energies and in the range

of 10^{11} to 10^{10} for higher energies (above 250-300 eV), with the peak intensity around 150 eV. In the case of pristine material, a shift in the binding energy is observed in the region of the highest beamline flux, which might indicate surface charging. Charging is a common problem in photoemission spectroscopy, especially when combined with high-brilliance sources like synchrotrons or lasers. This phenomenon occurs because the materials do not efficiently conduct away the charge when illuminated with X-rays, leading to an accumulation of positive charge on the sample surface. One result of this is the shift of peaks in the XPS spectrum. Charging can occur even in narrow bandgap semiconductors like Bi_2Te_3 when using very bright sources.

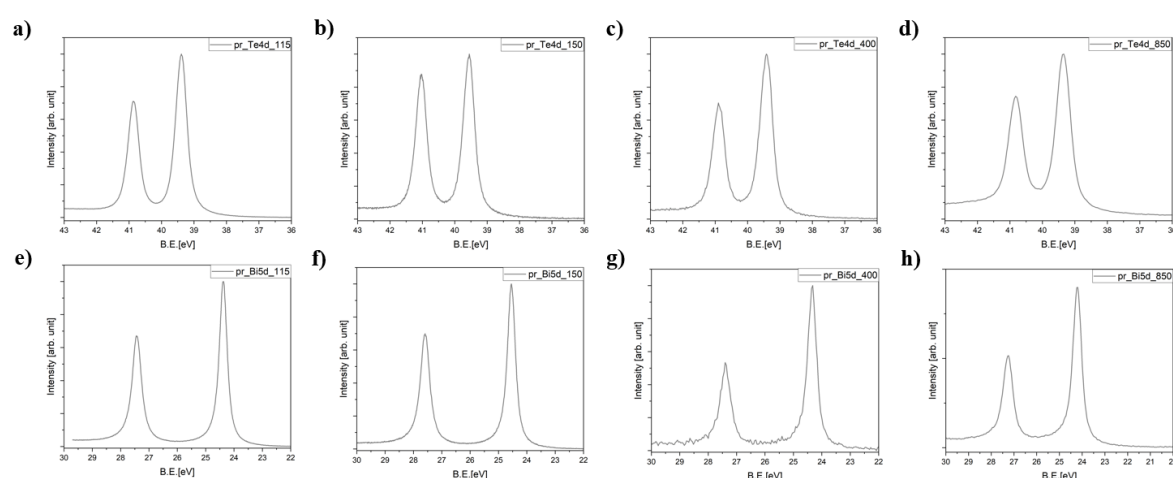


Figure 25 XPS spectra of Te4d and Bi5d were collected for various photon energies: a-d) Te4d core levels for 115 eV, 150 eV, 400 eV, and 850 eV, respectively; e-h) Bi5d core levels for 115 eV, 150 eV, 400 eV, and 850 eV, respectively.

Table 3 Comparison of Te4d and Bi5d peaks Binding Energy positions and differences in peak to peak ($\text{Te4d}_{5/2} / \text{Te4d}_{3/2}$ and $\text{Bi5d}_{5/2} / \text{Bi5d}_{3/2}$) ratio parameter.

Photons Energy [eV]	Te4d _{5/2} Binding Energy [eV]	Peak ratio	Bi5d _{5/2} Binding Energy [eV]	Peak ratio
115	39,38	1,43	24,37	1,49
150	39,55	1,14	24,56	1,45
400	39,40	1,43	24,32	1,89
850	39,34	1,33	24,20	1,80

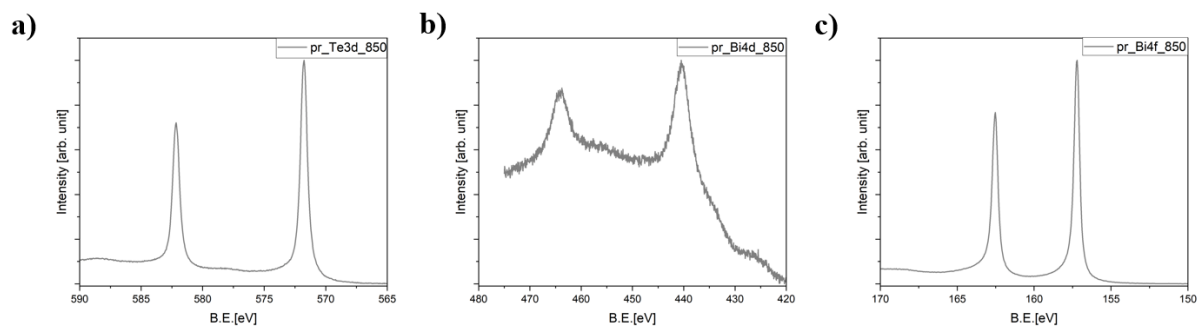


Figure 26 A photon energy of 850 eV provides access to deeper core levels of Te and Bi: a) Te3d, b) Bi4d, and c) Bi4f.

However, high flux not only implies a charging phenomenon but so-called radiation damage also. The radiation damage effect is one that can influence electronic structure of the materials. Unfortunately, the general formalism for this process is practically impossible to implement and describe due to the fact that this effect occurs for practically all materials, not only biological but also solids. In the later sections of this thesis, I will describe how radiation damage affects the electronic structure of topological insulators. However, at this point, I would like to focus solely on the impact of this process on semiconductors. Specifically, in this case, we can distinguish three phenomena that can be observed on the surface of an illuminated semiconductor.

The first is ionization, which involves the ionization of atoms in the surface material and, in certain cases, the creation of defects, or vacancies, leading to changes in the electronic structure. The next process is the so-called displacement damage, which leads to structural changes on the surface of the illuminated material. The third process discussed here is oxidation, more broadly defined as a chemical reaction occurring on the material's surface under the influence of incident UV and X-ray light. This phenomenon is quite common and relatively easy to detect in the photoemission studies. Besides the obvious factor of light illuminating the material's surface, the atmosphere (usually gaseous) in which the measurement is conducted plays a crucial role in this process. In the case of photoemission spectroscopy, where measurements are typically carried out under UHV conditions, it might seem that the issue of the atmosphere surrounding the sample is minimized. However, even under conditions of 10^{-10} or 10^{-11} mbar, a layer of residual gas molecules can "settle" on the material's surface within a few or several minutes. Residual gases, which constitute the gaseous atmosphere remaining in vacuum chambers after pumping down to UHV conditions, mainly consist of molecules of hydrogen, nitrogen, methane and its derivatives, oxygen, nitrogen oxide, carbon monoxide, carbon

dioxide, and water. Due to the wide variety of particles in the atmosphere and the different properties of the material's surface, chemical reactions can occur in several ways, such as the absorption of hydrogen molecules into the material's structure, the reaction of nitrogen molecules with the surface, or the deposition of carbon through the photodissociation of carbon monoxide, carbon dioxide, or methane molecules. Many of these processes can also occur spontaneously without illuminating the surface, such as absorption; however, these processes tend to occur much more slowly. In the case of carbon deposition on the sample surface, it is straightforward to determine whether the surface has undergone radiation damage by measuring the C1s core level in XPS. Figure 27 shows the measurement of C1s before and after approximately 12 hours of exposure to soft X-rays. A significant increase in the intensity of the C1s peak is observed on the surface, which should be free of carbon contamination. In the case of semiconductors, such chemical changes on the surface can lead to phenomena such as band bending, which is one of the key issues in surface physics. The influence of UV light and soft x-rays on the electronic structure of the synchrotron and laser studied materials is still often skipped or overlooked in the data analysis. The challenges associated with radiation damage and particle absorption into the crystalline structure of the material, as well as their impact on the electronic structure, will be further discussed in subsequent sections of my thesis.

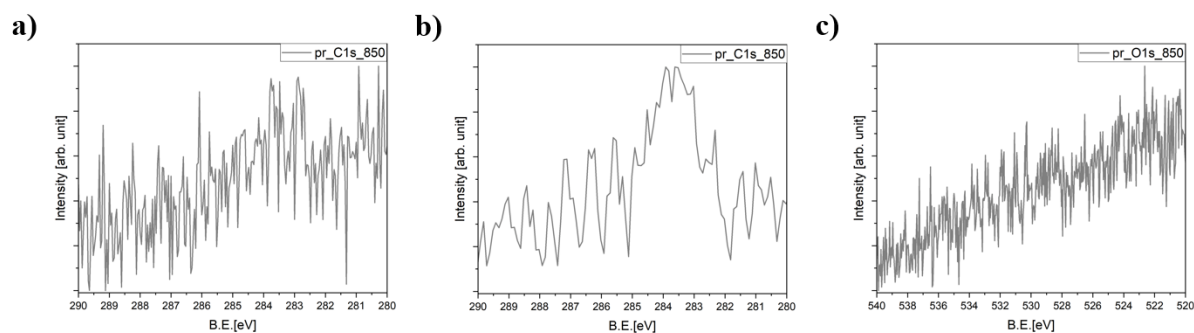


Figure 27 XPS data for C1s and O1s core levels for a pristine single crystal of Bi_2Te_3 were collected at 850 eV. The data presented in a) show the C1s core level after illuminating the sample surface for several minutes following sample preparation in the UHV. Spectrum b) shows the intensity of the C1s after approximately 12 hours of illumination. Spectrum c) shows the O1s, which does not change after several hours of exposure to X-rays.

The another issue discussed here regarding the description and analysis of XPS data is the photoelectron acquisition process by the analyzer. The hemispherical electron analyzer is a relatively simple device in terms of its working principle, allowing for precise determination of the kinetic energy of electrons. More details on the concept and construction of the analyzer can be found in Chapter 3. At this stage, we need to focus on the data acquisition process during

the experiment, specifically on the transmission parameters that affect the measurement. Each hemispherical electron analyzer is characterized by a set of transmission parameters such as Pass Energy, Energy Resolution, Acceptance Angle, Transmission Function, and Spectral Intensity, which are integral to every spectrum collected on the device. Proper adjustment (detector calibration) and the operator's know-how allow for collecting data with very high energy resolution.

However, most analyzers are calibrated using sources like electron guns or X-ray lamps with high photon energies (e.g., an Al lamp with an energy of 1486.6 eV). While this calibration is appropriate for these sources, it may not be ideal for measurements performed with synchrotron radiation, where the photon energy can be freely changed. Parameters such as the Transmission Function change when scanning with kinetic energies. When scanning with different photon energies, the kinetic energy changes for the same core level, which can lead to inconsistencies in the XPS spectrum for wide excitation energy range, such as non-constant peak ratios or not correct energy difference between peak (the last point can be related with the Gain parameter). Additionally, one of the best calibration samples is noble metals such as gold, where the Au4f and Au4d core levels are found at relatively high kinetic energies. If the transmission parameters are not correctly adjusted during energy scans in XPS, it can result in problems such as inconsistent peak ratios, especially when analyzing core levels at low kinetic energies.

The final point that can influence changes in the photoemission spectrum, discussed in this section, is the IMFP, λ_{in} . This curve has already been described, Figure 17, but during experiments conducted using synchrotron radiation, particularly when accessing low photon energies (>100 eV), it becomes a crucial factor in determining the sampling depth. Determination of λ_{in} can be conducted based on the equation⁸⁷

$$\lambda_{in} = \frac{(4 + 0.44Z^{0.5} + 0.104E^{0.872})a^{1.7}}{Z^{0.3}(1 - W)} [nm] \quad 4.1$$

where Z is the atomic number, a is an average atomic spacing, E is the energy in eV and W is the parameter related to the heating of formation of a compound. For low kinetic energies of electrons, the surface sensitivity of the material is very high, with a sampling depth ranging from 0.5 to 1 nm for most elements. As the kinetic energy of electrons increases (>1000 eV), the sampling depth increases to about 2-3 nm, as shown on Figure 28. The shallow sampling depth associated with low kinetic energies requires consideration of certain factors that can be neglected at higher energies, such as the atomic environment, which can differ between the surface and the bulk, and the inelastic scattering parameter, whose value increases as the kinetic

energy of the electron decreases. This parameter affects the shape of the XPS spectrum, particularly its background.

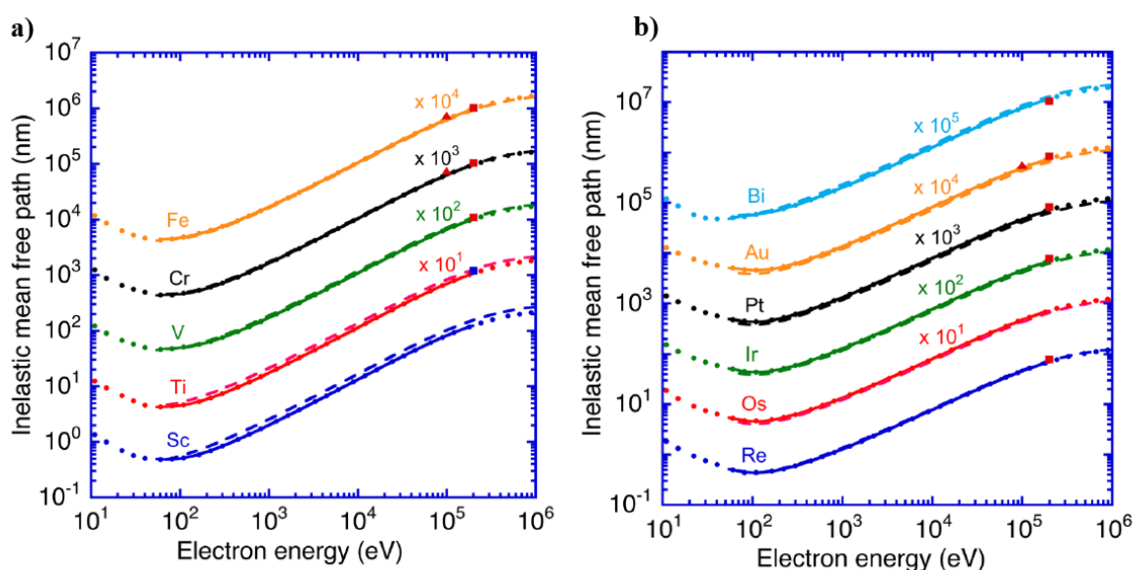


Figure 28 IMFP calculated⁸⁸ for few elements included a) Fe and b) Bi.

The conducted XPS studies revealed that the Bi_2Te_3 crystal is of very high quality and allowed for the determination of a starting point for chemical surface investigations of this sample. Measurements were performed at specific excitation energies ranging from 100 eV to 850 eV to facilitate chemical analysis at different sampling depths. The experiments successfully characterized the impact of synchrotron radiation (soft X-rays) on the measurements, enabling better surface quality control in subsequent stages.

4.1.2 ARPES studies

Bismuth-based topological insulators have attracted significant scientific attention over the past 20 years due to their simple yet remarkable electronic structure near the Fermi level. The surface states, with linear energy-momentum dispersion, form the so-called Dirac cone at high symmetry points. Electrons within the Dirac cone are spin-polarized, creating one-directional paths for spin in the electronic structure, which can be utilized in modern fields such as spintronics and quantum computing. These electrons cross at a single, symmetry-protected, spin-degenerate point known as the Dirac point. The position and tunability of the Dirac point in the electronic structure (energy direction) is a much studied area because mastering this process could lead to the production of topological transport devices. However, while the concept seems relatively accessible, its realization in experiments has proven to be very

challenging, requiring modifications in the structure of topological insulator materials. The concept of tuning the Dirac point in the electronic structure is well-known and can be achieved in several ways. One approach is chemical interference through surface decoration/deposition or structural doping, which can lead to a band bending scenario. Unfortunately, the challenge of precisely defining the position of the Dirac point in the electronic structure begins at the very outset and is rooted in the measurement method, such as ARPES. In ARPES, experiments are typically conducted with low-energy photons produced by UV lamps, lasers, or synchrotrons which may induce structural or chemical modifications in the illuminated region. Exposure to very intense light can influence the electronic structure, as discussed in the previous section. In this section, ARPES data for pristine Bi_2Te_3 will be presented. The ARPES data were collected at the URANOS and PEHLIX beamline at SOLARIS and were processed using an in-house software developed at the URANOS beamline. All the spectra were measured for Γ -K direction with the photon energy range from 20 eV to 180 eV. These experiments were complemented by XPS measurements, what allows for a comparative analysis.

The discussion of the ARPES results for the pristine single crystal Bi_2Te_3 begins with the analysis of the spectra collected using 20 eV photons. As shown in Figure 29 a), the VB is presented over a wide binding energy range, extending from 0.0 eV, which indicates the Fermi level, to - 3.5 eV binding energy. The bulk VB of Bi_2Te_3 are primarily composed of Bi p and Te p orbitals, exhibiting a parabolic shape that can be observed near the Γ point, which is aligned along the 0.00 wave vector k_x . As shown in Figure 29 b), the M-shaped band represents the Valence Band Maximum (VBM) and the single Dirac cone at Γ point.

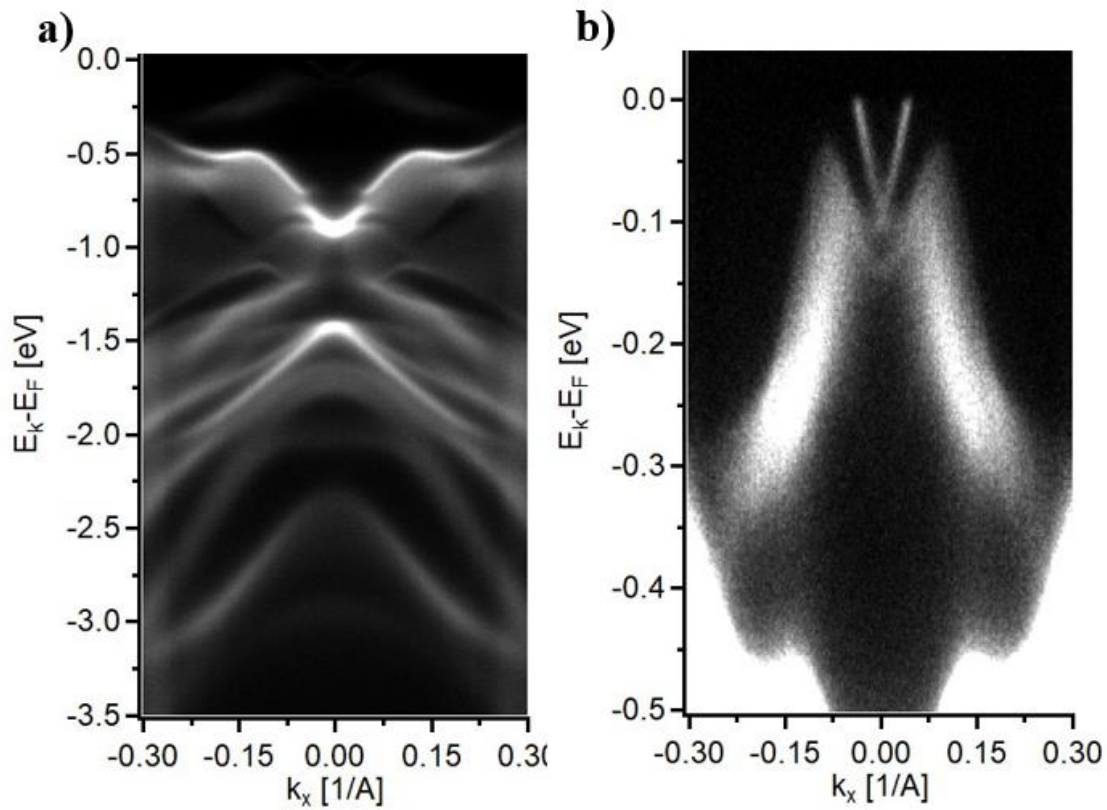


Figure 29 ARPES data collect with 20 eV photon energy in the Γ -K direction for wide binding energy range to illustrate a large VB area a). b) presents a band structure near the fermi level with the visible surface states in the range of 100 meV below Fermi level. Data were collected at 40 K.

The data presented in Figure 29 serve as a textbook example of ARPES measurements obtained from a high-quality Bi_2Te_3 crystal where the chemical potential is localized within the band gap. The energy position of the Dirac point is established at 100 meV below the Fermi level. The calculated band structure of the pristine material, shown in Figure 30 a), closely matches the observed band dispersion in my studies, further confirming the high quality of both the crystal and the experimental setup. The calculated energy gap is approximately 170 meV³². The values presented here do not fully align with all the experimental results conducted on pure Bi_2Te_3 , including theoretical data, where, for example, the band gap can vary by several tens of meV depending on the computational method used⁵³. From an experimental standpoint, there are two main reasons why the experimental data can differ significantly across studies.

The first is the sample itself, particularly its structure and chemical composition. The position of the Dirac point in the electronic structure can be influenced by chemical doping. In semiconductors, we generally distinguish between two types of doping: n-type and p-type. For pristine Bi_2Te_3 , both types can be considered⁸⁹. N-type Bi_2Te_3 is characterized by the relatively

deep position of the Dirac point in the electronic structure, typically around 200-300 meV below the Fermi level^{69,90}. N-type single crystals can be realized during the growth process⁹¹ (e.g., using MBE or the Bridgman method). If Te atom is missing from the crystal lattice, it creates a vacancy that acts as a donor site. Electrons associated with these vacancies can move to the conduction band, increasing the electron concentration. For the n-type material the Fermi level is shift near the conductivity band. In the case of p-type Bi₂Te₃, the hole contribution to conductivity is higher than in n-type Bi₂Te₃. The Fermi level shifts towards the VBM, with an energy position, that found in the literature, around 100 meV^{53,92}. The realization of p-type material also depends on the growth process, where a deficiency of bismuth (Bi : Te ratio should be 2:3) is introduced. This deficiency can lead to the creation of bismuth vacancies, which act as acceptors by trapping electrons and thereby generating holes. The observed type of conductivity can also be described in terms of antisite defects⁸⁹. In Bi₂Te₃, antisite defects can occur in two ways: bismuth on a tellurium site (Bi_{Te}) and tellurium on a bismuth site (Te_{Bi}). In both scenarios, one type of atom replaces another in the crystallographic lattice, creating either a deficiency or surplus of electrons in the material. Calculations and experiments have shown that Bi_{Te} acts as an acceptor, while Te_{Bi} acts as a donor. A straightforward explanation for this is that when a Te atom is replaced by a Bi atom in the lattice, an excess of electrons occurs because Bi has more valence electrons than Te, leading to n-type character of the material. Conversely, when a Bi atom is replaced by a Te atom, a deficiency of electrons is observed, resulting in p-type character of the material. Control of lattice defects is crucial for both current and future electronic devices, making a thorough understanding of these processes essential. Based on the considerations above, the ARPES data presented in Figure 29 and Figure 30 indicate p-type material, with an excess of Te atoms observed in the XPS data (Figure 24).

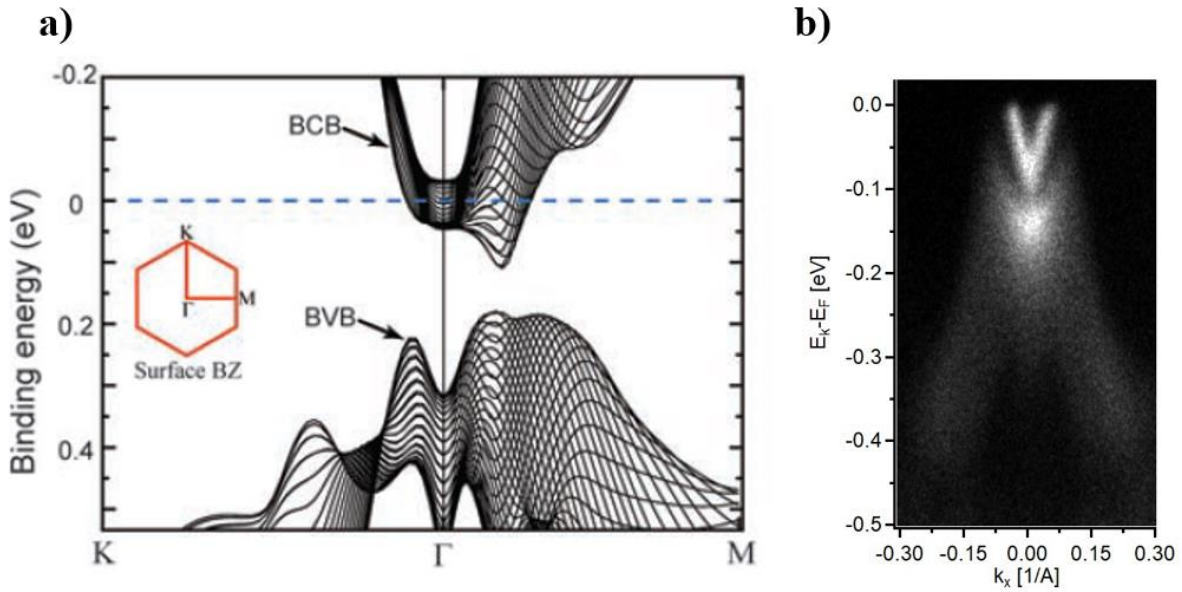


Figure 30 a) Represents the calculated bulk conduction band (BCB) and bulk valence band (BVB) dispersions along high-symmetry directions of the surface Brillouin zone for Bi_2Te_3 ³². b) Shows the Bi_2Te_3 spectra collected using 55 eV photons.

The second reason why the data may differ significantly, as previously discussed, is the influence of light, specifically UV light and soft X-rays generated by the synchrotron. These very bright sources produce a high density of photons focused on a small area, which can lead to chemical and structural modifications of the sample surface. In XPS, this can be observed, for example, as an increase in the C1s core level during illumination. In the case of ARPES data, the changes can be more subtle and are often not discussed by experimentalists, but they are an inseparable part of the experiment and should always be taken into consideration.

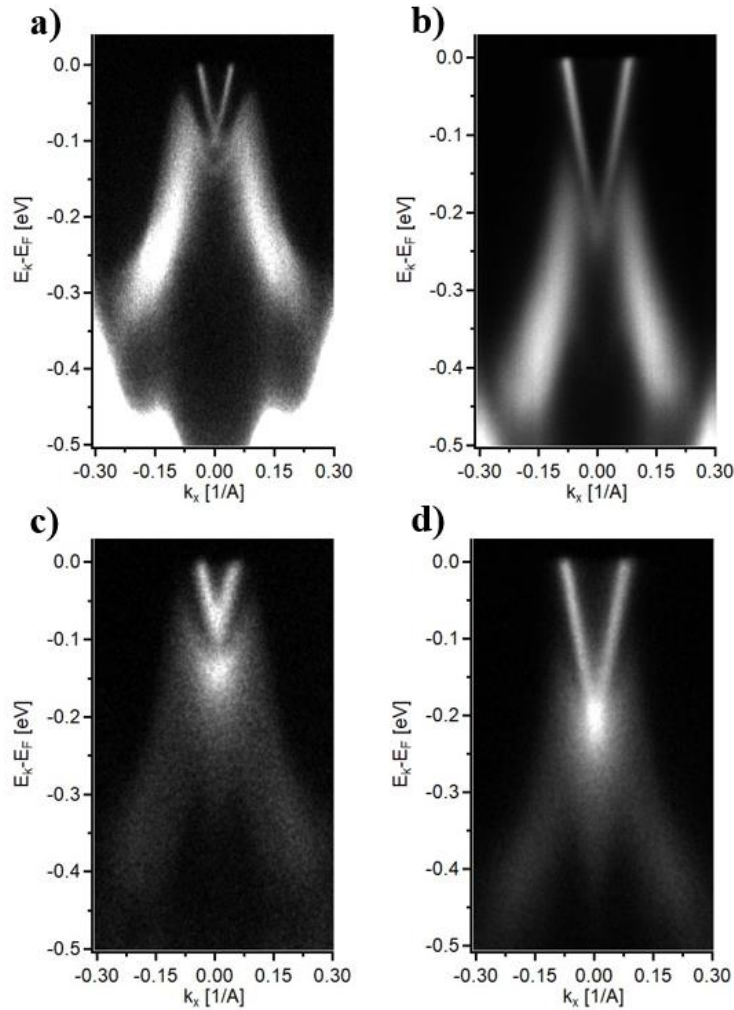


Figure 31 ARPES data collected for pristine Bi_2Te_3 . Spectra a) and c) represent the electronic structure near the Fermi level measured within the first few hours after the initial illumination of the sample surface with photon energies of 20 eV and 55 eV, respectively. Spectra b) and d) show the same data collected after the entire set of measurements was completed overnight. The "aging" process is evident, as the position of the Dirac point shifts towards higher binding energies.

A straightforward way to explain the influence of light on the sample's electronic structure is by examining Figure 31. The data presented in Figure 31 a-b) and c-d) were collected using 20 and 55 eV photons, respectively, with the sample temperature set to 40 K. Figure 31 a) and c) show spectra collected during approximately the first two hours of the experiment. Even within this timeframe, subtle modifications to the electronic structure were observed. Unfortunately, the data acquired in the very first minutes are difficult to interpret. The only statement that can be made here is that within the first seconds or minutes after the initial illumination of the sample, the chemical potential is much closer to the VBM, but the Dirac point cannot be measured accurately (assuming that its position is 3 - 4 meV from the Fermi level) and is therefore not presented. This observation is likely a consequence of the sample preparation process, specifically the mounting of the sample to the measurement holder. The challenge

begins right from the initial step of mounting the sample onto the sample holder. Achieving the desired crystal orientation is often crucial in ARPES studies. Unfortunately, this step cannot be overlooked in many cases because many measurement manipulators do not have 6-axis rotation capabilities (e.g., at the URANOS beamline). Crystal orientation can be achieved using tabletop diffractometers or LEED in UHV. Once properly oriented, the crystal must be introduced into the UHV system, where further preparation steps, such as annealing or exfoliation, are applied. The sample is then transferred to the analysis chamber, and measurements begin. However, high-quality data are often not obtained with the first light. The alignment procedure, which involves scanning the sample surface to find the optimal spot on the crystal surface and the desired point in the Brillouin zone, must be conducted. This process can take anywhere from a few minutes to several hours. During the alignment process, modifications in the electronic structure, referred to as "aging," can occur, Figure 31 b) and d).

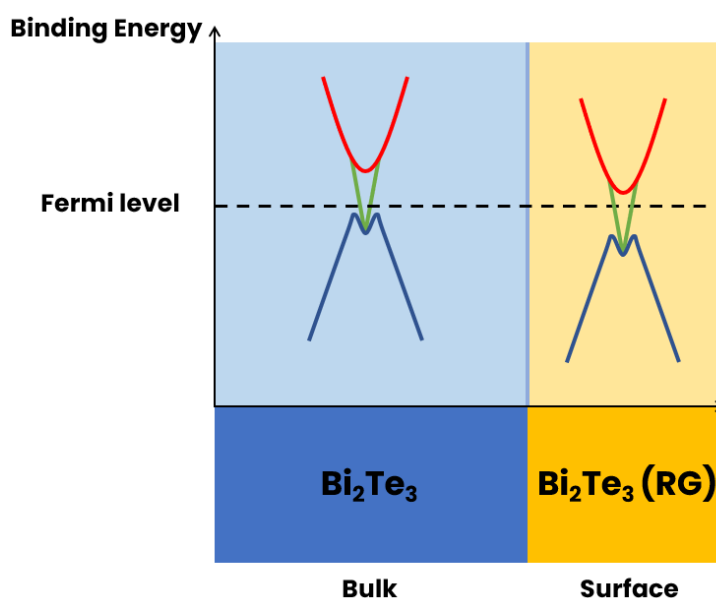


Figure 32 Illustrative representation of the band bending scenario in Bi_2Te_3 driven by residual gas (RG) adatom surface decoration (and absorption) and the influence of radiation. The chemical potential is positioned near the Dirac point in the bulk, and when an interface is created at the surface, the bands shift downward (n-type doping), placing the Fermi level near the CBM.

This "aging" process is an unintentional form of band bending, leading to changes in the valence band electronic structure and shifts in the position of the chemical potential as shown in Figure 32. A detailed yet simple explanation of this phenomenon in semiconductors and TIs can be found in the literature⁹³ and it is explained in Figure 33. A similar effect is observed in single-crystal Bi_2Te_3 , where downward band bending occurs over a few hours of illumination with low-energy photons (ranging from 20 eV to 100 eV), Figure 31. However, the photo-desorption

process (the last stage in Figure 33) was not detected in my research. The key idea is that Bi_2Te_3 is a vdW material, where the gaps between the quintuple layers (QLs) can act as reservoirs for adatoms and other molecules. Atoms can migrate into the Bi_2Te_3 structure and become "trapped" within the QL gaps through intercalation. This effect can expand the vdW gaps within the Bi_2Te_3 structure, causing modifications to the electronic structure, such as the shift of the Dirac point⁴⁶. A concomitant effect of the vdW gap expansion is the influence of absorbed gas molecules, such as H_2 , on the Bi_2Te_3 electronic structure. The material's sponge-like behavior can be driven by surface illumination, leading to adsorption. This absorption of H_2 molecules can lead to downward band bending (band bending of approximately 120 meV), a phenomenon predicted by theoretical approach⁹⁴.

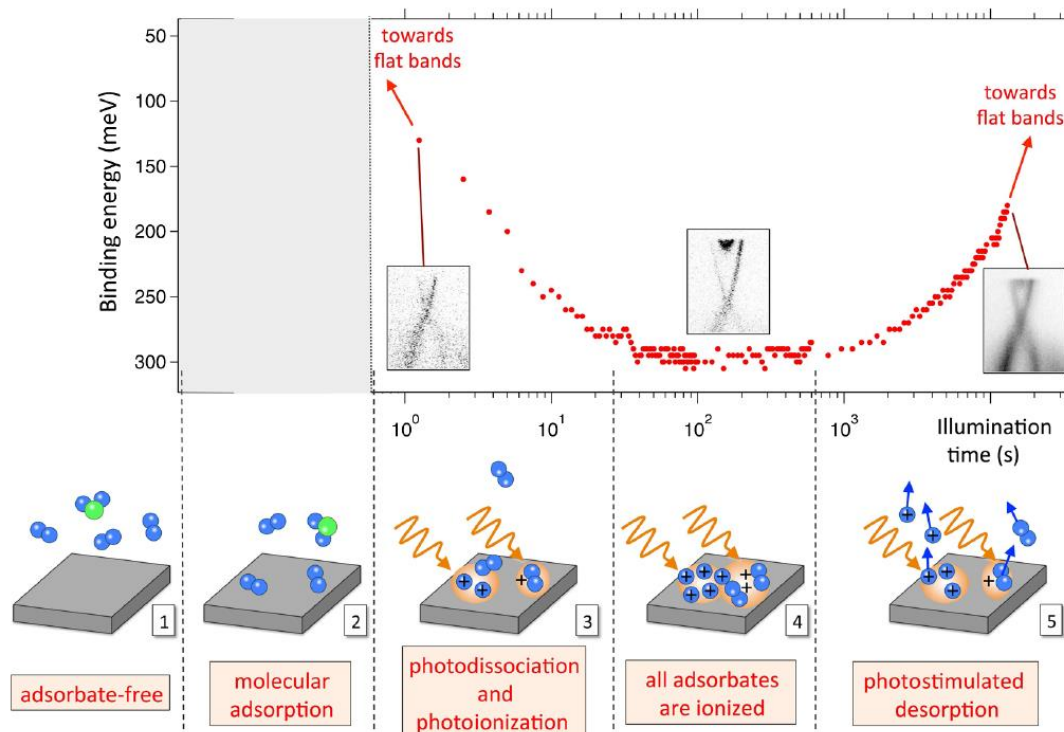


Figure 33 An illustrative explain proposition of the "aging" effect after exposure to residual gases and the UV light (27 eV) is demonstrated using the TI BiSbTeSe_2 from⁹³. In the first step, the sample is cleaved in UHV and can be considered pristine. Within a few seconds of exposure to UHV, residual gas molecules begin to cover the freshly cleaved surface. In the third step, the first photons reach the sample surface, and measurements starts. At this point, a downward band bending scenario begins as photodissociation of molecules starts to occur. The electronic structure shifts towards lower binding energies, which can lead to the unearthing of the CBM. Eventually (4th stage), most of the molecules become ionized, and maximum band bending is achieved. In the final stage, desorption of the ionized adatoms can occur, leading to upward band bending and partial restoration of the original band structure.

According to the collected ARPES data for the Bi_2Te_3 single crystal, it is evident that both factors-the sample growth/preparation process and the surface exposure to soft X-rays (and UV

light)-can significantly modify the electronic structure of the material, as shown in Figure 31. Unfortunately, my studies cannot conclusively determine which of these effects has a greater influence. However, it is clear that both phenomena must be considered during data analysis when studying various 2D and 3D materials using PES techniques. The above discussion will be crucial for further considerations addressed in this thesis. At this stage, based on ARPES data, it is concluded that the material is considered pristine when the Dirac point is located approximately 100 meV below the Fermi level and surface states are observable in the vicinity of the Fermi level.

4.1.3 CD-ARPES studies and OAM

OAM plays a significant role in solid-state physics, particularly due to its potential application in novel electronics based on orbitronics⁹⁵. Orbitronics is an emerging field within condensed matter physics that focuses on the manipulation and utilization of the OAM of electrons in solid-state systems. This field aims to harness the OAM of electrons as a means to store, process, and transmit information, potentially leading to new types of electronic devices with enhanced performance and novel functionalities. In materials, OAM refers to the component of an electron's total angular momentum associated with its motion around the nucleus, an atom, or a lattice site in a solid. Unlike spin angular momentum, which is an intrinsic property of the electron, OAM arises from the electron's spatial distribution and its orbital motion. OAM plays a crucial role in the electronic structure of materials, particularly in those with strong SOC, such as TIs and heavy metals. In the case of Bi-based TIs, the SOC is exceptionally strong and couples with OAM, contributing to the total angular momentum. Both of these phenomena significantly influence the electronic structure of materials.

CD-ARPES is a powerful technique that allows probing the OAM signal. The key idea behind CD-ARPES is that the interaction between circularly polarized light and the OAM of electrons leads to different photoemission intensities for circularly left-handed and circularly right-handed light. This intensity difference, CD, is related to the OAM of the electronic states in the material and can be visualized using the (3.32). The theory behind the CD signal and CD-ARPES technique is discussed in more detail in Chapter 3.

In topological insulators like Bi_2Te_3 , the surface states exhibit a strong coupling between spin and OAM due to SOC. The helical nature of these states implies that the OAM is oriented perpendicular to the electron momentum, and this orientation can be detected using CD-ARPES. In Figure 34, ARPES and CD-ARPES data measured for Bi_2Te_3 are presented. The

comparison is made between the spectra collected using linearly horizontally polarized light, a) and c) (the standard light polarization for both the PHELIX and URNOS beamlines), and the CD signal for photon energies b) of 50 eV and d) 55 eV. The data are consistent with other examples in the literature⁶⁹, and the CD signal does not change sign within this narrow energy range (CD measurements were performed from 49 to 57 eV with 2 eV step). The significance of this specific energy range lies in the idea that during the deposition the magnetic material the CD sign of the surface states can be changed. It was propose to decorate the surface of the Bi_2Te_3 with the Fe atoms to achieve such as magnetic interface. The Fe core level 3p, falls within this energy range and the further experiment were carried on for this system. Several CD-ARPES experiments were conducted on pristine Bi_2Te_3 during my research. In Figure 34, we can observe the data collected after approximately two days of illuminating the sample surface (with the Dirac point positioned around 200 meV below the Fermi level).

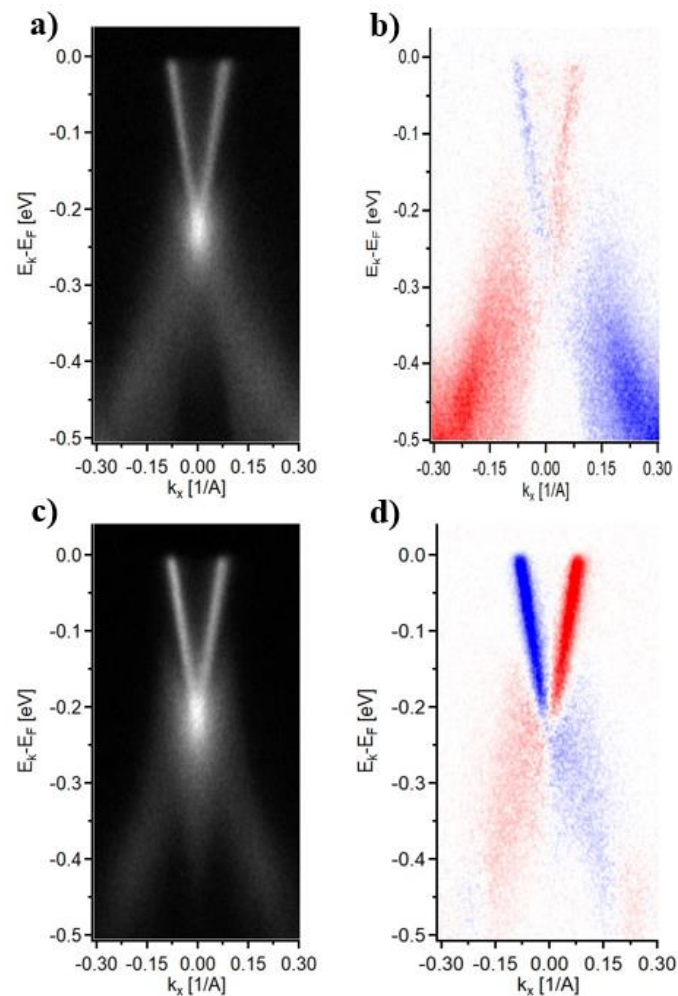


Figure 34 CD-ARPES data collected for a Bi_2Te_3 single crystal. In (a) and (c), ARPES spectra are shown for horizontally polarized light with photon energies of 50 eV and 55 eV, respectively, in the Γ -K

direction. The corresponding CD signals are presented in (b) for 50 eV and (d) for 55 eV light. Presented data were collect at the URANOS beamline at 40 K.

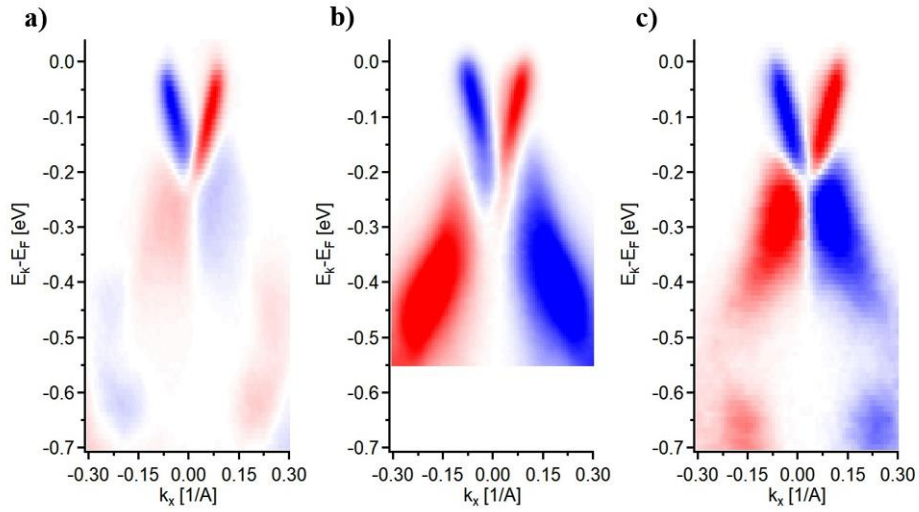


Figure 35 CD-ARPES data were collected for a Bi_2Te_3 single crystal for wide photon energy range up to 180 eV at the PHELIX beamline at 80 K. Spectra a) was measured for 55 eV, b) for 115 eV and c) for 180 eV.

Unfortunately, during the nearly three years of research conducted on beamlines, significant issues with crystal quality were observed at a certain point. The material underwent exfoliation dozens of times during the experiments, which affected the quality of the crystal surface what implicate the ARPES spectra, as seen in Figure 35 and Figure 36. The spectral resolution is noticeably better in Figure 35, which was collected several months earlier. Nevertheless, despite the reduced crystal quality, it was still possible to interpret the CD data. Figure 36 shows the CD signal for surface states over a broad energy range, aimed at verifying the data in⁶⁹ and expanding the understanding of CD signal changes across a wider excitation energy range than in Figure 10. The results are consistent with previous reports, showing a CD sign change in the energy range of 75 to 100 eV, followed by another sign change above 115 eV. The similar type of measurement were carried out for different Bi-based TIs⁹⁶ to show the photon energy dependence CD sign change in the surface states.

In my research, CD-ARPES measurements were conducted to determine whether introducing transition metal impurities on the surface of a TI can modify the CD signal. To achieve this, the deposited transition metal on the surface should exhibit magnetic properties and potentially break time-reversal symmetry. To establish a good starting point, I performed CD-ARPES measurements in the wide energy excitation energy range (including the Fe3p region) for

pristine Bi₂Te₃. This allowed us to track changes in the subsequent experiments, which included the deposition of Fe on the surface of the TI.

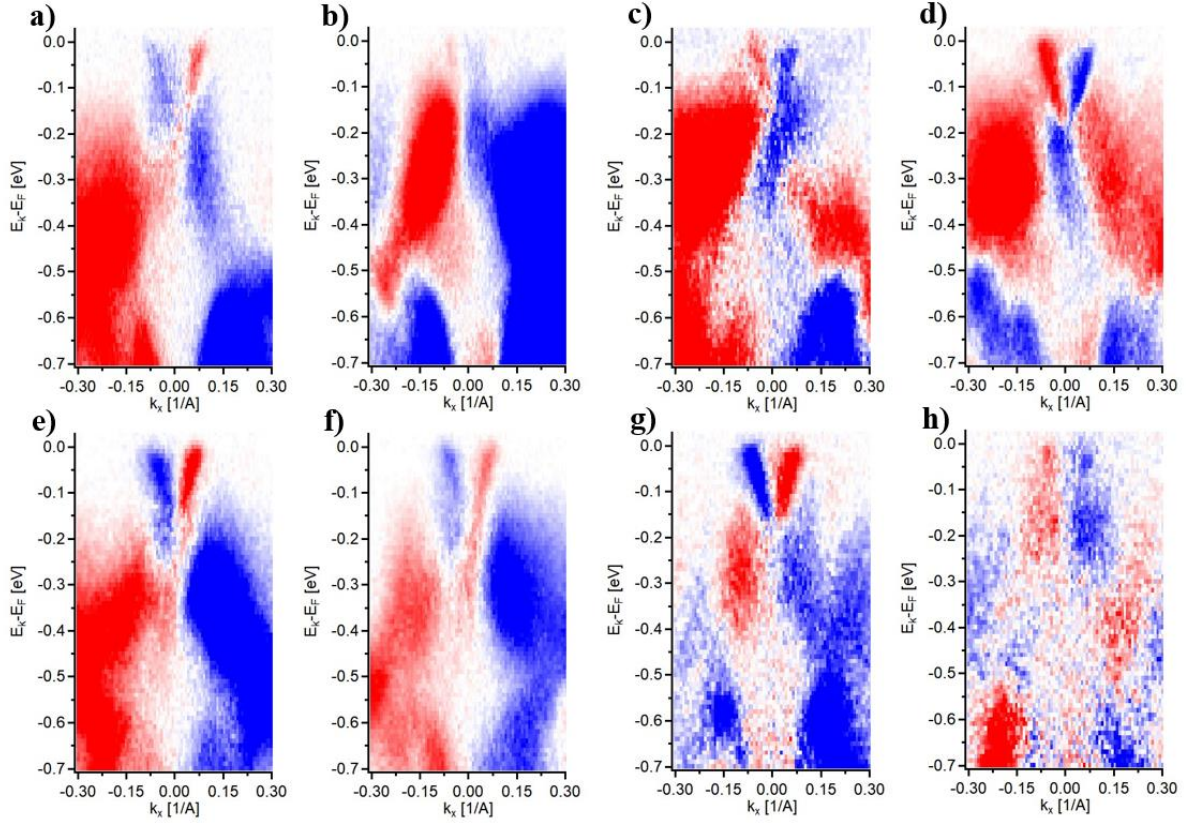


Figure 36 CD-ARPES measurements were performed on pristine Bi₂Te₃ for various photon energies: a) 50 eV, b) 80 eV, c) 95 eV, d) 100 eV, e) 115 eV, f) 120 eV, g) 130 eV, and h) 140 eV. The variation in the CD signal's sign with changes in excitation energy was studied across different energy ranges and was reported in⁶⁹.

4.2 Bi₂Te₃/Fe system

The primary objective of the project was to introduce a thin layer of transition metal on the surface of Bi₂Te₃ and monitor the resulting changes in the electronic structure through photoelectron spectroscopy measurements. Introducing dopants or capping the surface of a TI may brake time-reversal symmetry which is essential for the preservation of surface states. Magnetic dopants, in particular, can break time-reversal symmetry by introducing a magnetic moment with a preferred spin direction⁹⁷. This modification alters the Hamiltonian by incorporating a magnetic exchange interaction term in Equation 2.8, which in turn modifies the energy spectrum, leading to the opening of an energy gap

$$E(k) = \pm \sqrt{(\hbar v_F k)^2 + \Delta^2} \quad 4.2$$

where Δ is the energy gap open factor at Dirac point due to magnetic influence. This gap emerges directly from the interaction between the spin and OAM of electrons in the surface states, which are integral to the topological protection of these states. This can lead to the perturbation in the surface state, OAM distribution and influence the electronic structure. The opening of the gap can also lead to a phase transition, potentially unveiling the Quantum Anomalous Hall effect, where the Hall conductance is quantized even in the absence of an external magnetic field. This occurs because magnetic doping induces a chiral edge mode in the gapped surface state⁹⁸.

Over the past 15 years, research has focused on the effects of magnetic and non-magnetic dopants, as well as surface modifications, on TIs. These studies aim to induce broken time-reversal symmetry and shifts in the chemical potential, with the goal of exploring potential applications within the modified spin matrix. One approach involves constructing doped TIs using transition metals, which can lead to the manufacturing of magnetic topological insulators (MTIs). The Bi-based TI family is extensively studied using this method. A common example is Mn-doping of Bi_2Se_3 ^{99–104} and Bi_2Te_3 ^{55,66,105–107}, where Mn, with its five unpaired electrons in the 3d shell, provides a significant magnetic moment, making it ideal for magnetic studies. The concept of doping TIs with transition metals is discussed in Chapter 2. Doping not only leads to gap opening but also causes significant changes in the electronic structure and shifts the chemical potential. Controlling the shift of the Fermi level is a major focus of research due to its potential applications.

Capping TIs, while less common due to the potential degradation of surface quality, has also been explored. Studies on Bi_2Te_3 capped with transition metals like Fe ⁶⁴ have shown that, although gap opening is not observed, there are modifications in the electronic structure, leading to n-type doping and shifting the chemical potential towards the CBM. As outlined in the research objectives, the decision was made to cover the surface of Bi_2Te_3 with a transition metal, initially selecting Fe, and later Co, to expand our understanding of the chemical properties of the TI single crystal surface following this process. This section of the thesis will present the results of Fe deposition on the Bi_2Te_3 and its impact on the electronic structure and the collected signal using CD-ARPES. The sample preparation process was carried out in the UHV systems at the URANOS and PHELIX beamlines. The deposition of Fe was performed using high-purity (99.999%) metal wires in a PREVAC type Electron Beam Evaporator. The deposition rate was controlled by a quartz crystal microbalance and set to 0.3 Å/min for Fe. At the URANOS beamline, the evaporator with the material was installed in the preparation chamber during the

experiment. For the PHELIX beamline experiment, an MBE system was prepared for the deposition of both elements in UHV. The deposition was conducted at room temperature, after which the capped single crystal samples were introduced into the measurement manipulator. The majority of the ARPES and CD-ARPES data were collected at URANOS at 40 K, within the energy range of 20 eV to 55 eV. The PHELIX experiment was conducted at 40 and 80 K, and the resulting XPS and CD-ARPES data will be presented.

4.2.1 XPS studies

The deposition of Fe on the surface of Bi_2Te_3 was conducted in several stages until a thickness of 1 Å Fe was achieved. It was decided not to proceed with a thicker layer based on the ARPES data which indicated that a capping process diminished surface quality, making it unacceptable to continue collecting data with the remaining features at that stage of a research. The initial step involved decorating the surface of Bi_2Te_3 with 0.2 Å of Fe atoms. The experiments involving the deposition of Fe atoms were conducted on two beamlines, with the initial studies performed at URANOS, focusing on ARPES data. Subsequent experiments, including both ARPES and XPS, were carried out on the PHELIX beamline. The initial capping process was predict to deposit 0.2-0.3 Å per step until reaching a total thickness of 1 Å. However, due to the time-intensive nature of the preparation process, it was decided in the later stages (at PHELIX) to reduce the number of deposition steps to three (first 0.2 Å, second 0.5 Å, third 1 Å) to more efficiently monitor the electronic structure behavior.

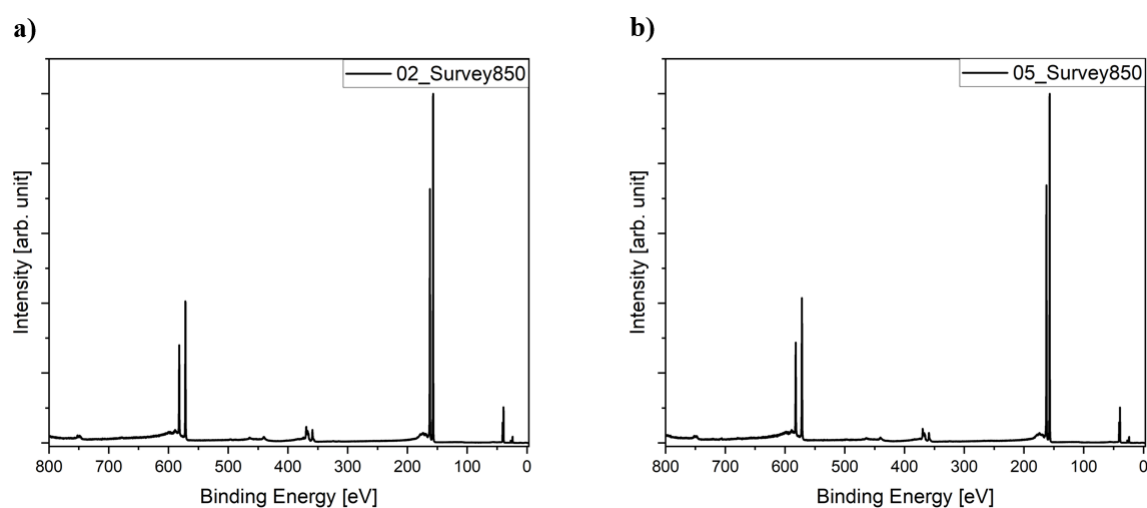


Figure 37 XPS survey spectra were collected with photon energy of 850 eV and temperature of 40 K. (a) The spectra were measured for 0.2 Å of Fe on top of Bi_2Te_3 , and (b) for 0.5 Å of Fe.

After the initial deposition steps, further deposition was carried out, adding approximately 0.3 Å of Fe atoms to the Bi₂Te₃ surface, resulting in a total expected coverage of 0.5 Å of Fe on the surface of the TI. Following the deposition, the sample alignment procedure was executed as previously described, and XPS survey data were collected. However, the amount of Fe detected was not significant at 850 eV. Due to limited beamtime, it was decided to proceed with ARPES measurements at this point so the XPS deep profiling was not conducted on this system. A coverage of 1 Å was achieved in the next step of the preparation process. Figure 38 presents survey data with indicators of the Fe3p and Fe2p core levels, which are visible at a photon energy of 850 eV. The background shape at higher binding energies suggests a decrease in surface quality, which is expected given the deposition process used.

The XPS data in Figure 37 present the survey spectra for 0.2 Å and 0.5 Å Fe deposited on top of Bi₂Te₃. From the outset, it must be understood that due to the exfoliation process, the surface preparation is not ideal. Even on a relatively flat surface, there can be areas where the sample is not well exfoliated, or where the surface is contaminated, making photoemission studies, especially ARPES, challenging. For pristine Bi₂Te₃, the situation is more straightforward. A good quality surface spot must be identified by scanning with the electron analyzer and sample manipulator. Once such a spot is detected, the measurement can begin. However, when additional preparation steps, such as deposition, are required, aligning the sample becomes much more complex.

The first issue is that the deposition process, which varies across different end stations, often operates with different geometric parameters (e.g., deposition angle or distance between the atom source and the sample). This, together with other growth conditions, can ultimately lead to uneven decoration of the surface, where islands or structures with varying densities of deposited atoms form. These irregularities will affect the photoemission signal, potentially leading to inconsistencies in the data. The second issue is that the sample manipulator monitors position the sample with a resolution in the range of 5-10 μm. While this may seem insignificant given that the beam spot size is approximately 100x50 μm, it can still impact the spectra resolution. Although this might not be as critical for XPS, it makes a significant difference in ARPES. Therefore, the sample alignment procedure was standardized by starting with ARPES spectra measured in Live Mode (snapshot mode). If a good quality surface spot was found, the XPS measurements were initiated. The manipulator positions were saved, and after any further preparation steps, alignment would begin from these saved positions. The assessment of surface quality was based on the visibility of surface states at the Γ point, within the Γ-K direction. The

final challenge encountered during data analysis and plotting was the variation in scan parameters selected throughout the experiments. Due to the need to maximize counts and reduce acquisition time, parameters such as Pass Energy or energy step were adjusted for both lower and higher photon energies. This led to slight shifts in the kinetic energy axis, which can be normalized to the Fermi level or the Au4f peak, but also disrupted ratio parameters (e.g., peak-to-peak or peak-to-background ratios). A clear example is presented in the survey spectra in Figure 37, where the energy step was set to 0.5 eV. This adjustment resulted in the Bi4f core level being measured near its maximum, while the Te3d level was measured below its maxima, potentially leading to some misinterpretation of the spectra. The survey spectra were only measured after the deposition of the d-metal and are intended to serve as a reference for subsequent steps.

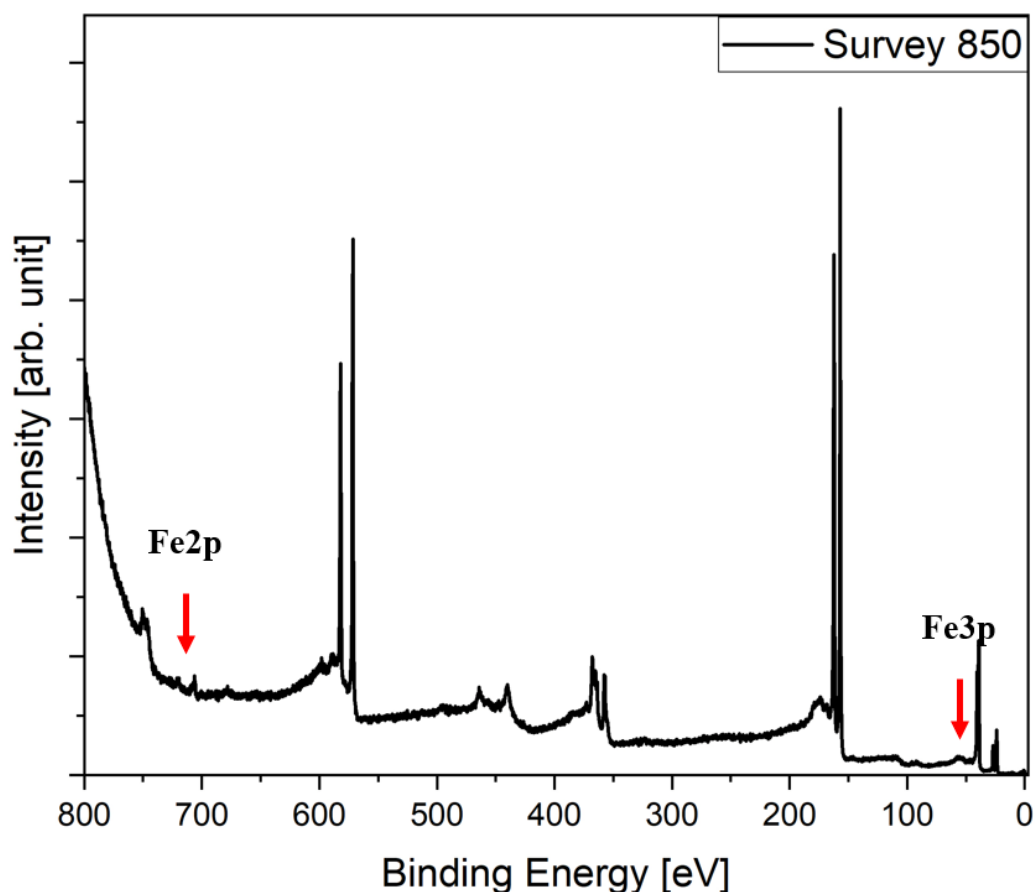


Figure 38 XPS survey spectra were collected at 850 eV for 1 Å of Fe atoms on Bi₂Te₃. The red markers indicate the positions of the Fe 2p and Fe 3p core levels, which are the main points of further analysis.

Of course, the primary technique for imaging surface states in topological materials is ARPES, which enables imaging with ultra-high energy and angular resolution. However, the idea for conducting detailed XPS studies emerged during the project as data analysis progressed and a

broader spectrum of theoretical studies was reviewed. These studies suggest⁸⁶ that when atoms or gas molecules are deposited onto the surface of Bi₂Te₃, they may penetrate the material's structure and occupy vdW gaps. The synchrotron radiation and beamlines offer a wide range of measurement capabilities, one of which is the ability to vary the excitation energy, ultimately allowing for depth profiling XPS measurements.

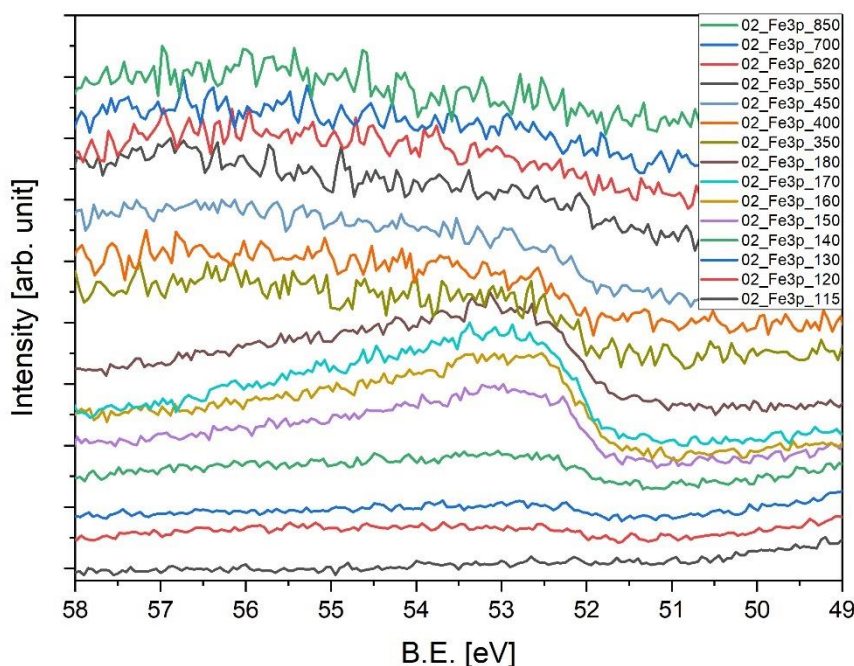


Figure 39 XPS data for the Fe3p core level. The spectra shown here were measured from the same spot after the deposition of 0.2 Å of Fe on the Bi₂Te₃ surface. The use of a wide photon energy range allows for variation in probing depth, providing detailed information about the chemical composition of the produced interface.

The implementation of XPS depth profiling measurements is illustrated in Figure 39. The spectra were collected across a wide energy range for the Fe3p core level. At first glance, it is evident that the intensity of the Fe3p signal varies with different photon energies. Within the range from 130 eV to 450 eV, the Fe3p signal remains detectable at the binding energy of around 53 eV. According to the IMFP curve, Figure 17, in this range, we are probing electrons from depths of approximately 5 to 10 Å (from the lowest to the highest kinetic energy). What is unusual in this study is that at lower excitation energies, specifically 115 eV and 120 eV, the Fe3p core level is not detected. According to the IMFP curve, these energies should provide information from the very surface, at a depth of approximately 4 Å (The penetration depth d can also be calculated using the formula $d = \frac{1}{\mu(\omega)}$ where μ is the absorption coefficient, which

depends on the excitation energy ω . The absorption coefficient is also material-dependent, varying with different materials and influencing how deeply the photons penetrate into the sample).

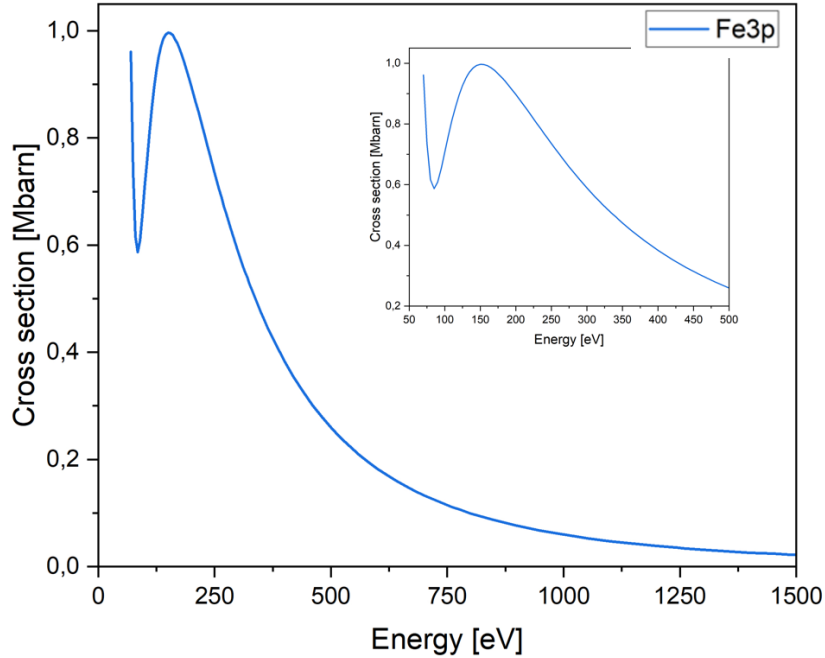


Figure 40 Photoionization cross sections vs photon energy calculated^{108,109} for Fe3p core level.

However, scanning with varying excitation energies introduces additional considerations beyond the technical and instrumental factors already mentioned. One critical factor that must be accounted for in the analysis is the photoionization cross section. This parameter plays a crucial role in XPS data analysis, especially when scanning across a wide energy range. The photoionization cross section estimates the probability of an electron being ejected from the material's surface upon absorbing UV light or x-rays. There is no universal formula that allows for direct calculation of the photoemission cross section; therefore, tabulated data are widely used in this context^{108,110,111}. In Figure 40, the Fe3p cross-section calculations are plotted according to available data in^{108,109}. In these studies, the following equation was applied to calculate the photoionization cross section

$$\sigma_{nlj}(E) = \frac{4\pi^2\alpha\alpha_0^2}{3} \frac{g_j}{g_{nl}} \cdot |R_{nlj}(E)|^2 \quad 4.3$$

where α is the fine structure constant, α_0 is the Bohr radius, g_j and g_{nl} are statistical weights for the specific orbital nlj and the initial state and $R_{nlj}(E)$ is the radial matrix element for the photoionization process.

Before analyzing the depth profile XPS spectra, it is essential to carefully examine the data presented in Figure 40. The photon energy range used in the experiment spans from 115 eV to 850 eV. Within this range, the photoionization cross section varies significantly, decreasing from 0.8 to 0.1 mbarn ($1 \text{ barn} = 10^{-24} \text{ cm}^2$), with a peak value of 1 mbarn observed between 155 and 160 eV. An important consideration for further data analysis is that the cross section remains relatively high, around 0.8 mbarn, for photon energies in the 110-115 eV and 220-230 eV ranges. Returning to Figure 39, we observe that the intensity of the Fe3p peak increases within the energy range where the photoemission cross section is notably high. The change in this parameter is also significant, varying by approximately 30% for energies in the range of 100 eV to 250 eV. Despite this variation, the value of the cross section remains relatively high in this energy range, especially when compared to higher energies like 450 eV or 850 eV, where the cross section values drop to 0.3 and 0.09, respectively.

Considering the information from the photoionization cross section and the interpretation of the IMFP, we can infer from the collected XPS data that after the initial deposition of approximately 0.2 Å of Fe on the surface of Bi₂Te₃, Fe was detected. However, the highest intensity of the Fe3p peak does not correspond to energies that probe the very surface of the material. This suggests that either the amount of Fe atoms at the illuminated spot was insufficient (potentially due to a non-uniform deposition process) or that a significant portion of the Fe atoms were absorbed into the Bi₂Te₃ structure, as discussed earlier. To further discuss this assumption, it is important to note that the data in Figure 39 are not normalized to the photoionization cross section. The energy scale and intensity were normalized to the Fermi level and a current diagnostic device (mirror current), respectively. Therefore, understanding the quoted values for photoemission cross section is crucial for the subsequent research steps.

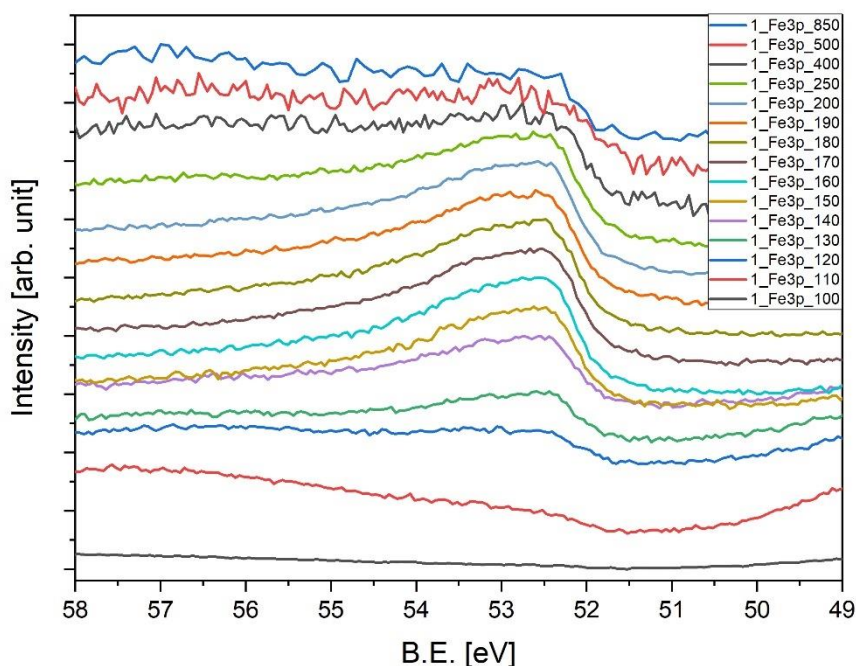


Figure 41 XPS data for the Fe3p core level. The spectra shown here were measured from the same spot after the deposition of 1 Å of Fe on the Bi₂Te₃ surface.

The primary focus during the Fe-capped Bi₂Te₃ studies was on the Fe3p, Te4d, and Bi5d core levels. Figure 41 presents XPS data for the Fe3p core level collected over a wide energy range. Based on data from lower Fe coverage, the starting excitation energy was reduced to 100 eV. Even after depositing five times more Fe atoms in the preparation process, the Fe3p core level signal remains nearly undetectable at the lowest photon energies (100 eV and 110 eV).

As shown in Figure 41, the amount of Fe is significantly higher compared to the first deposition step, with the maximum intensity of this transition appearing over a wide energy range, starting at 120 eV, increasing up to 200 eV, and then gradually decreasing as it approaches 850 eV, where the signal is very small. Considering the IMFP and photoionization cross-section parameters, this example suggests that Fe migration into the material is occurring. However, to fully understand this possible behavior, an analysis of the Te and Bi core levels must also be completed.

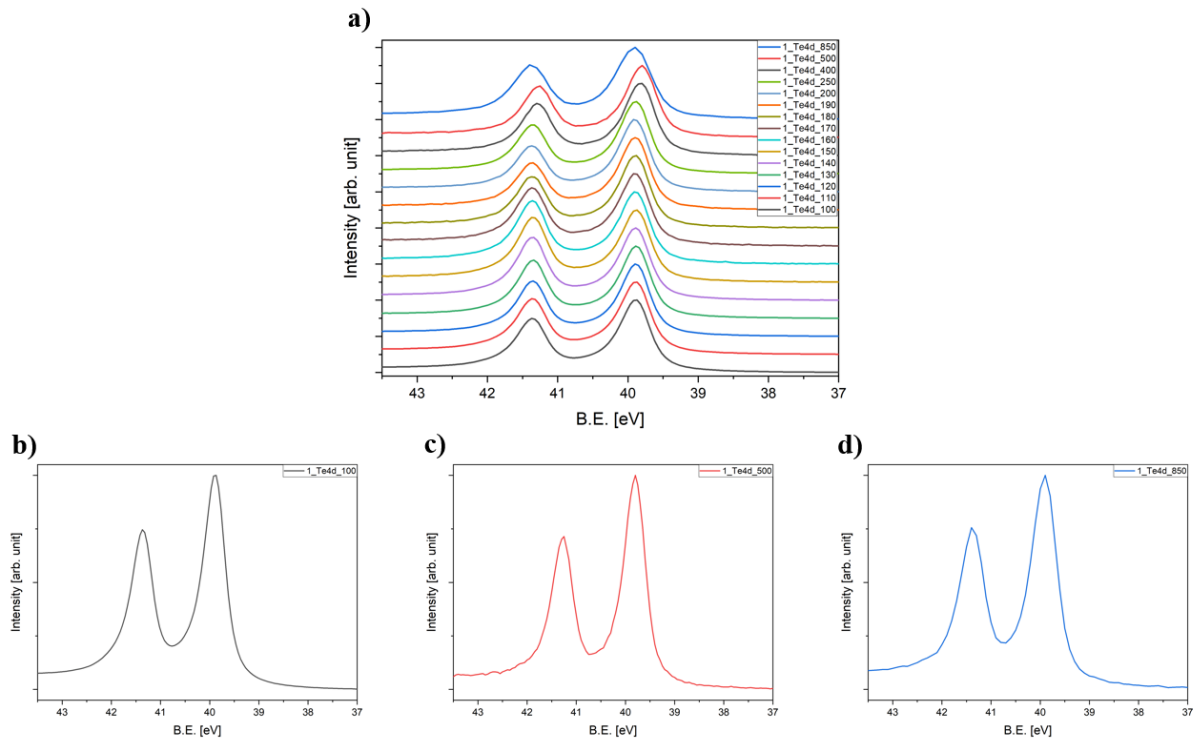


Figure 42 a) XPS spectra of the Te4d core level were collected across a photon energy range of 100 eV to 850 eV. The observed asymmetric shape of the core level peaks b-d) suggests that Te forms additional phases during the sample preparation and measurement processes.

Measurements of the Te4d and Bi5d core levels were conducted in conjunction with Fe3p spectra to ensure coherence. As shown in Figure 42, the Te4d spectra were collected across the same energy range as the Fe3p spectra. Analysis of the Te4d core level reveals an asymmetry toward higher binding energies, a feature not observed in pristine Bi₂Te₃. This asymmetry may indicate that Te has formed a new phase, which appears as a result of Fe deposition. According to the studies referenced in^{112,113}, the phase produced in the reaction is FeTe, which is expected to be amorphous in our case, as there was no heat treatment of the substrate to reconstruct the structure. It was also anticipated that Fe deposition could trigger a chemical reaction with Te atoms near the surface because the XPS data for the pristine material showed an excess of Te atoms in the Bi₂Te₃ structure. The energy position of the Te4d_{5/2} peak is revealed to be 39.85 eV, indicating a shift of approximately 300 meV compared to the spectra collected for pristine Bi₂Te₃. This chemical shift can be discussed as a band bending effect, a phenomenon already mentioned in this thesis. Band bending causes an energy shift of the entire photoemission spectrum near the surface where the junction is formed and this effect occurs and it is expected to be occurring in range of 200-300 meV according to ARPES data⁶³ that will be presented in the next pages. This phenomenon will be explained in more detail in the section where ARPES data is interpreted. A stable energy shift is observed in the photon energy range of 100 to 250 eV.

Beyond this point, the shift begins to decrease towards lower binding energies, with the position of the Te4d_{5/2} peak at 39.80 eV at 500 eV photon energy. This indicates that at these energies, we are approaching the limit of the band bending effect. Unfortunately, there is an inconsistency in the data for the 850 eV excitation energy. During post-experiment analysis, it was observed that the Fermi level was not fully captured, preventing the fit from being conducted in the same manner as for the other results. This discrepancy could affect the position of the core levels measured at this specific energy. Nevertheless, this result remains crucial for the overall experiment and must be presented to fully understand the chemistry of the produced interface.

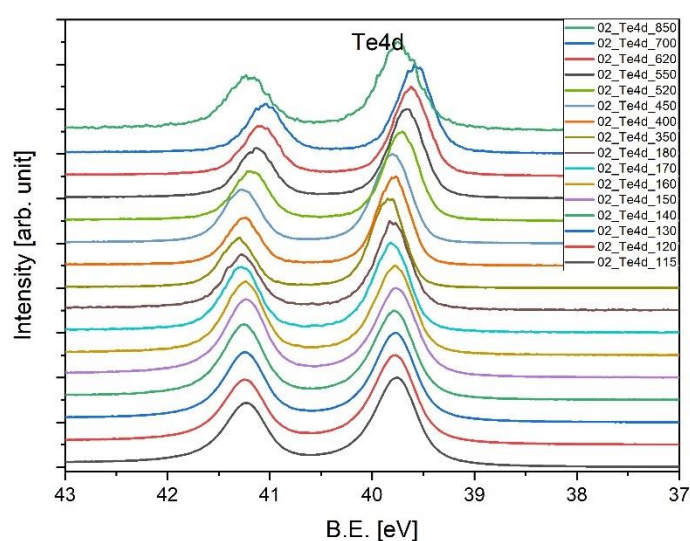


Figure 43 XPS spectra of the Te4d core level were collected for a 0.2 Å Fe deposited on the surface of Bi₂Te₃, in a photon energy range of 115 eV to 850 eV.

To complete the discussion of the Te4d core level, Figure 43 presents the data collected for a coverage of 0.2 Å of Fe, where a shift in the peak position across a wider energy range is observed. The energy position of the Te4d_{5/2} peak at a photon energy of 115 eV is 39.76 eV, indicating that a junction has been created and that the band bending effect is occurring. The maximum shift in the energy position is recorded at 39.83 eV for an excitation energy of 180 eV. This position remains stable until reaching 520 eV, after which it begins to shift towards lower binding energies, eventually reaching a position close to that of detected for the pristine material, 39.57 eV, at 700 eV.

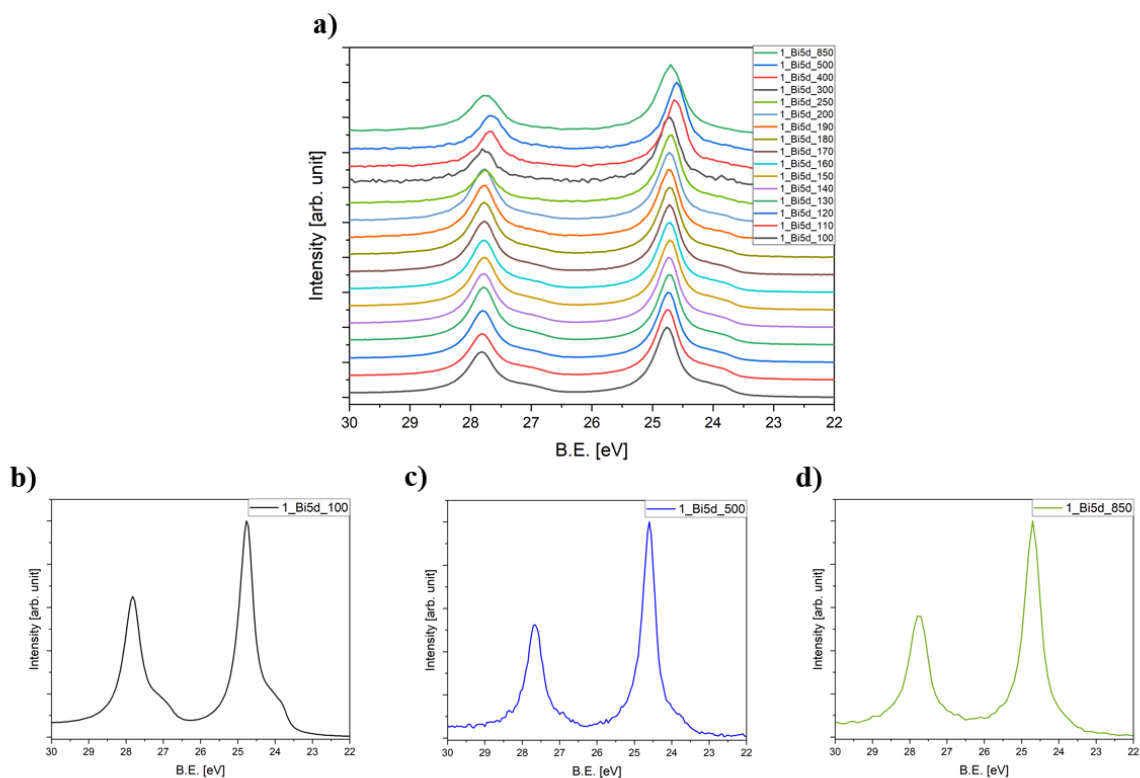


Figure 44 XPS spectra of the Bi5d core level were collected for a summary of 1 Å Fe deposited on the surface of Bi₂Te₃, in a photon energy range of 100 eV to 850 eV.

To complete the XPS data analysis, the core level of Bi must be examined. It has already been established that the surface decoration process with Fe atoms has induced several effects, such as the absorption of Fe atoms into the structure and chemical reactions on the surface, leading to the formation of the FeTe phase. Figure 44 presents the data for the Bi5d core level. Compared to the pristine material, it is evident that for excitation energies ranging from 100 eV to 500 eV, a multi-component structure of the core level is observed. The main Bi5d_{5/2} peak is located at 24.72 eV (Appendix 1), with an energy shift of approximately 350 meV towards higher binding energies relative to the data collected for pristine Bi₂Te₃. The similar behavior as for the Te4d core level where energy shift towards lower binding energies is also detected for energies above 400 eV, with the peak positioned at 24.60 eV at 500 eV. The behavior of the energy shift for Te4d and Bi5d is consistent within the same energy range. It is important to note that at an excitation energy of 850 eV, the metallic component of the Bi5d spectra is not observed. This absence indicates that the metallic Bi is confined to the very surface of the Bi₂Te₃.

The additional component in the Bi5d spectra is observed at a binding energy of 24.12 eV and can be attributed to the metallic component of Bi¹⁴. This can be explained by the fact that Fe

can substitute Bi (Fe_{Bi}) in the Bi_2Te_3 lattice⁶². According to DFT calculations and STM studies⁶², Fe_{Bi} is identified as the lowest-energy-defect configuration, compared to Fe substitution at the Te site. The Fe_{Bi} configuration can be observed when deposition occurs at temperatures that are not low (in case of my studies the deposition took place at RT). The potential influence of the high-intensity photon flux during the measurements must also be considered, as it could drive chemical processes on the material's surface by locally heating the illuminated sample spot. However, no significant evolution of the Bi5d or Te4d core levels was observed during the XPS measurements, which suggests that the substitution Fe_{Bi} is a possible explanation for the phenomena observed in the XPS data presented here. Additionally, the data indicate that the concentration of metallic Bi is close to the surface, covering the Bi_2Te_3 material, which is sort of rich in the FeTe phase. It is also worth noting that the activation energy for the Fe-Te reaction is lower than for the Bi-Fe reaction, further supporting the likelihood of appearance of Fe-Te bonding in this system.

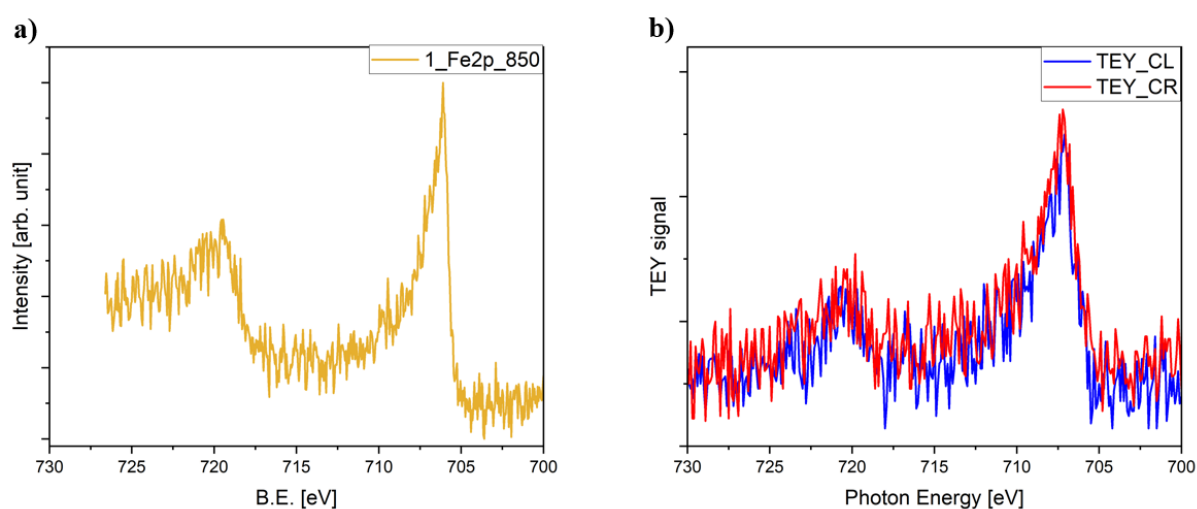


Figure 45 The XPS and XAS spectra collected for Bi_2Te_3 capped with 1 Å of Fe. The Fe2p core level was measured using XPS at an excitation energy of 850 eV, as shown in a). In b), the XAS spectra of the Fe L-edge are presented, measured using right- and left-circularly polarized light (red and blue, respectively). XAS data were normalized to the mirror current to get the counts (beamline diagnostic device).

To conclude the discussion of the XPS data, the spectra of the Fe2p core level are presented in Figure 45 a). The maximum of Fe2p_{3/2} peak is observed at a binding energy of 706.2 eV, which indicates that the Fe is in a metallic state. This observation closely aligns with XPS data measured for FeTe films¹¹⁵. One of the primary objectives of depositing Fe on the surface of Bi_2Te_3 was to introduce magnetic interactions. Figure 45 b) shows an attempt to measure this magnetic behavior in the Fe L-edge region using XAS (TEY mode) with circularly polarized

light (both left and right). Unfortunately, no differences in the peak intensity was observed, which suggests that the deposition of approximately 1 Å of Fe is insufficient to induce magnetic order in the constructed junction.

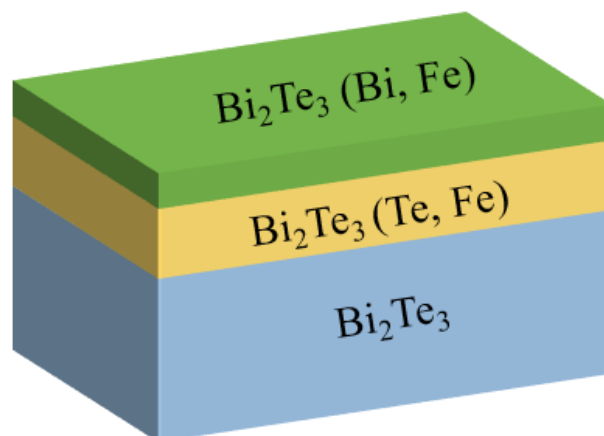


Figure 46 The illustrative proposition of the Fe atoms deposition influence at the Bi_2Te_3 surface structure.

The proposed illustration Figure 46 of the influence of Fe atom deposition on the Bi_2Te_3 surface structure suggests the existence of three distinct regions, as indicated by XPS data:

- surface region (Green): This is where metallic Bi has formed, likely due to the substitution of Bi by Fe atoms during deposition.
- middle surface region (Yellow): In this area, the formation of the FeTe phase is possible, indicating a chemical reaction between Fe and Te atoms near the surface.
- Bottom region (Blue): This region remains largely untouched, preserving the original Bi_2Te_3 structure.

These findings highlight the stratified nature of the surface modification induced by Fe deposition.

4.2.2 ARPES and CD-ARPES studies

The very first experiment conducted during my research on the Bi_2Te_3 system was ARPES at the URANOS beamline. The measurements for the pristine material were demonstrated in one of the previous sections. Here, the ARPES data for the Bi_2Te_3 single crystal capped with Fe atoms will be presented. In this first experiment, it was decided that the deposition process

would occur in four steps: the first step involved 0.2 Å, followed by 0.5 Å, then 0.8 Å, and finally, a total of 1 Å of Fe was deposited on the surface of the topological insulator. Initially, the plan was to evaporate approximately 2 Å of Fe (around 1 monolayer), but during the ARPES experiment, it became apparent that this approach would not successfully open the gap. Additionally, CD-ARPES measurements were carried out using photon energies of 50 eV and 55 eV. These energies were chosen based on the expected position of the Fe3p peak, which is located around a binding energy of 53 eV. The influence of Fe deposition on the CD signal was measured for the selected systems. Unfortunately, due to technical issues related to both the sample and the beamline, some data from this ARPES and CD-ARPES experiment were not collected properly, making accurate analysis impossible. Consequently, only a portion of the collected data will be presented in this section.

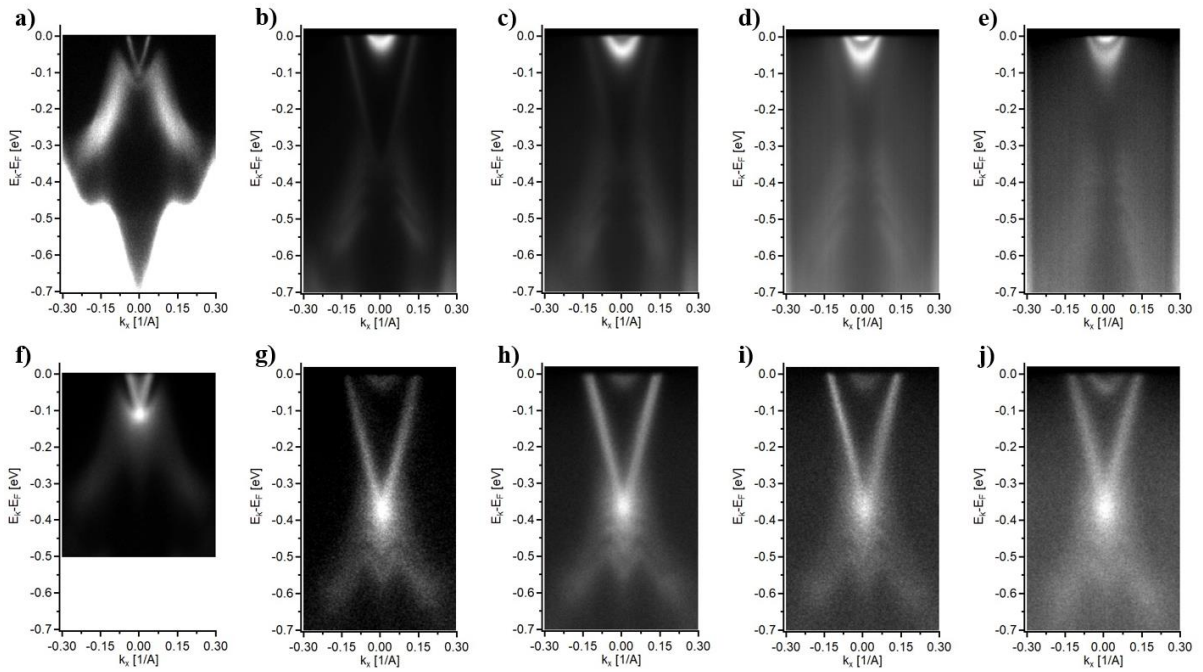


Figure 47 ARPES data were collected using a-e) 20 eV photons and f-j) 55 eV photons at 40 K to observe the evolution of the electronic band structure upon the deposition of Fe atoms on the surface of Bi_2Te_3 . Picture a) and f) represent the spectra for the pristine material, serving as references. Picture b) and g) show data after the deposition of 0.2 Å of Fe, c) and h) after 0.5 Å of Fe, d) and i) after 0.8 Å of Fe, and finally e) and j) after 1 Å of Fe on the surface.

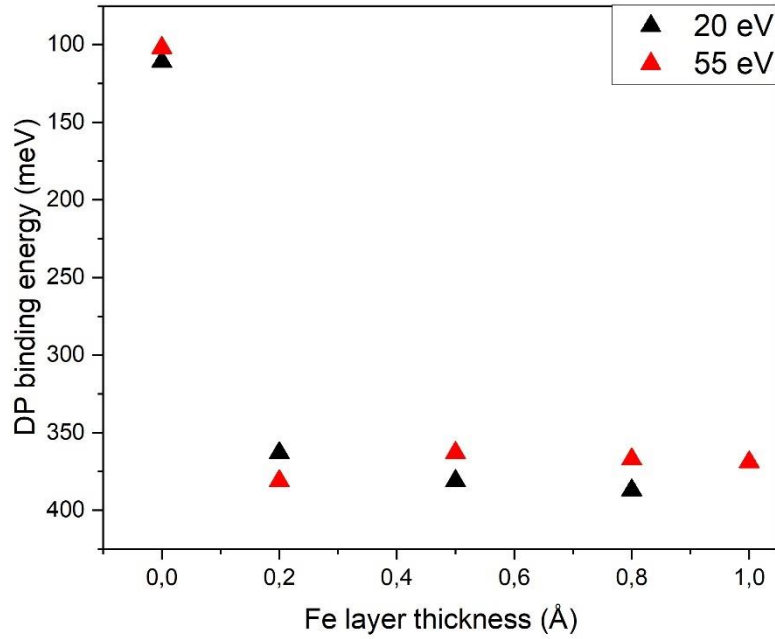


Figure 48 The black (20 eV photons) and red (55 eV photons) triangles in this figure highlight the observed shift of the Dirac point in the electronic structure of Bi_2Te_3 under Fe capping. These markers clearly indicate the extent of the energy shift, providing a visual representation of the band bending effect as Fe atoms are deposited onto the surface of the topological insulator.

The main findings related to the ARPES data are presented in Figure 47, where the evolution of the electronic structure is observed under the deposition of Fe atoms on Bi_2Te_3 . A clear energy shift, indicative of a downward band bending effect, is evident in both the 20 eV and 55 eV data series. Initially, the Dirac point is positioned at approximately 100 meV below the Fermi level in the pristine material. By tracking the position of the Dirac point across the energy scale, precise information about the extent of band bending occurring at the material's surface is obtained, Figure 48. The position of the Dirac point was observed to be approximately 360 meV and 375 meV below the Fermi level for the first deposition, using 20 eV and 55 eV photon energies, respectively. Subsequent depositions exhibited a steady downward trend for 20 eV photons, revealing the conduction band minima, CBM1 and CBM2, in the later deposition steps, with the Dirac point eventually reaching around 380 meV. However, analyzing the energy position of the Dirac point is challenging with 20 eV photons because the intensity of this point is the same as rest of the VB. In case of 55 eV photons, the Dirac point is more distinctly visible, showing higher intensity compared to the rest of the electronic structure within the VB. The existence of CBM1 and CBM2 upon the deposition of Fe indicates the formation of a 2DEG near the surface¹¹⁶, driven by the junction formation at the top of Bi_2Te_3 . The existence of the

2DEG should be expected when downward band bending occurs in a narrow-gap semiconductor, particularly if the shift in the chemical potential approaches the CBM. This shift can lead to the creation of quantum wells that trap electrons near the surface. In conventional semiconductors, the 2DEG is typically degenerate, but due to the very strong SOC in Bi₂Te₃, the bands within the CB are also quantized.

The band bending effect has been mentioned several times throughout this thesis, yet a detailed theoretical explanation is still needed to fully understand why bands bend when a connection between metal and semiconductor occurs. There are several types of contacts that can induce band bending, such as ferroelectric/semiconductor, magnet/semiconductor, or semiconductor/semiconductor junctions. In the case of a metal making contact with a semiconductor (forming a Schottky junction or Schottky contact), electrons begin to migrate from one material to the other - specifically, from the material with a lower work function to the one with a higher work function. This migration continues until an electric field develops that halts further electron transport. This process can be described using two fundamental relationships. The first relationship links the electron density to the potential within the materials through the Boltzmann distribution

$$n(x) = n_0 e^{\frac{q\phi(x)}{k_B T}} \quad 4.4$$

where $n(x)$ is the electron density in the function of position x , n_0 is the bulk electron density, q is the electron charge and $\phi(x)$ is the local electrostatic potential.

The second relationship is the Poisson equation which relates the spatial distribution of the electric potential $\phi(x)$ with the charge density $\rho(x)$ in material

$$\frac{d^2\phi(x)}{dx^2} = -\frac{\rho(x)}{\epsilon} \quad 4.5$$

Where ϵ is the permittivity of the material. The Poisson equation give information about the potential change near the junction where band bending occurs. Both of these equations provides description about how the distribution of the electron within the interface leads development of the electric field which driven the band bending effect in the semiconductors.

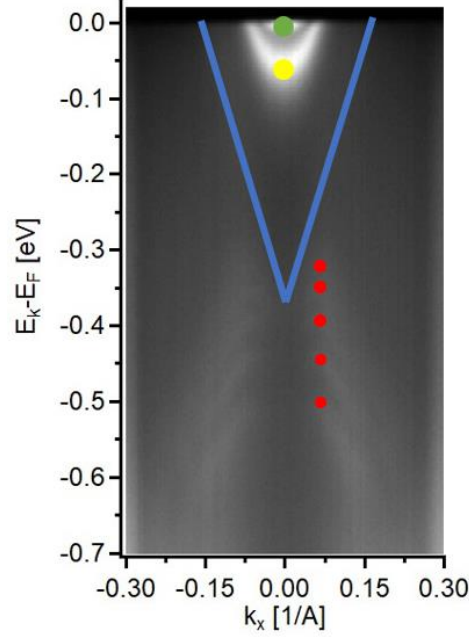


Figure 49 ARPES data collected for Bi_2Te_3 capped with 0.8 Å of Fe. The blue lines indicate the surface states, the yellow dot marks CBM1, and the green dot marks CBM2. The red dots indicate the 5 split bands in the M-shape VB.

Additionally, the band bending effect can drive other phenomena, such as the existence of quantum well states within the VB (and CB). These quantum well states arise when the band bending creates a potential well that can confine charge carriers, leading to discrete energy levels, E_n , within the valence or conduction band, Figure 49, and can be express as

$$E_n = \left(\frac{3\pi}{2} \hbar q F \right)^{2/3} \left(\frac{n - \frac{1}{4}}{m^*} \right)^{2/3} \quad 4.6$$

where F is the electric field induce by band bending and n is the quantum number.

In the Bi_2Te_3 system decorated with a transition metal, such as Fe, the formation of a metal-semiconductor junction is expected, where the previously discussed band bending and quantum confinement effects driven by band bending can occur. These effects have already been observed in other systems, such as Bi_2Se_3 ^{54,65,101,103,104,116,117}, which is a common material where band bending is introduced by dopants or surface decoration. In Bi_2Te_3 , quantum well states have also been introduced through non-magnetic decoration⁵³. It is anticipated that perturbations to the electrostatic potential-such as those induced by Fe deposition on the surface-will result in band bending. Along with the large potential step at the vacuum/material interface, this creates a quantum well for electrons, potentially leading to the splitting of the VB and CB into subbands⁵⁴, as observed in Figure 47.

However, for such band splitting to occur, certain conditions must be met, such as the band bending effect being greater than the width of the VB itself. While this is relatively easy to achieve in Bi_2Se_3 , it is more debatable in Bi_2Te_3 . In the case of my system, considering all parameters, the final band bending is estimated to be in the range of 320–330 meV (the cause of the band bending is twofold: residual gas absorption on the surface and the illumination with UV or soft X-rays run the first band bending which occurs a few seconds after illumination and the second related to Fe deposition). The M-shaped VB in the Γ -K direction of Bi_2Te_3 is approximately 340–350 meV wide. Therefore, it is possible that this condition is not fully met in these studies.

Another possible explanation for the existence of splitting bands within the VB and CB can be discussed in the context of vdW gaps and their expansion when adatoms occupy these spaces. The expansion of vdW gaps can lead to the emergence of additional bands corresponding to different vdW spacings^{46,86} within the studied system. I can expect that this behavior may also drive the splitting process in my system.

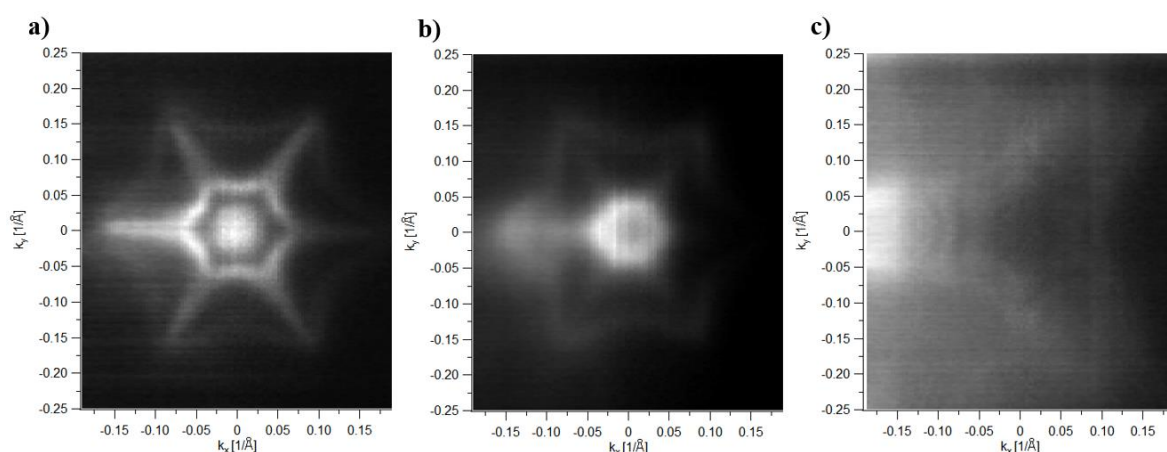


Figure 50 ARPES map collected, for Bi_2Te_3 covered with 0.5 \AA of Fe, using 20 eV photons. In panel a), the Fermi level is shown near 0.0 eV binding energy, with two bands appearing near the Γ point identified as CBM1 and CBM2. The outermost structures represent the surface states. b) presents a cut near CBM1, and c) shows a cut near the Dirac point, where the M-shaped subbands are visualized.

We must return now to the primary objective of this study, which is the potential opening of a gap between the VB and the surface states. Both results, for 20 eV and 55 eV, show that gap opening did not occur as a result of Fe atom deposition on the surface of the topological insulator, Figure 47. This outcome was somewhat expected, as previous XAS studies indicated that the Fe2p state did not exhibit magnetic properties in this system. However, it is notable that

the surface states for the 55 eV energy remain clearly visible throughout the entire deposition process, whereas for 20 eV photons, these states diminish as the Fe atom coverage increases.

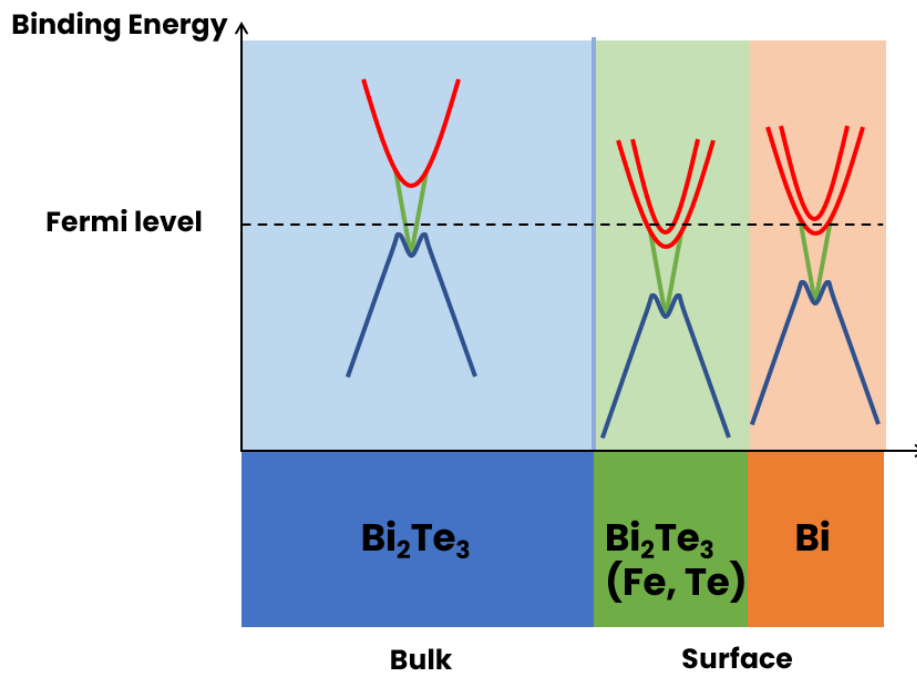


Figure 51 Illustrative representation of the band bending scenario in Bi_2Te_3 driven by the deposition of a transition metal (Fe in this case) on the surface of the TI. Based on the ARPES and XPS data, the surface can be divided into two regions: one rich in metallic Bi and another where the FeTe phase occurs. Analyzing the energy-dependent ARPES spectra (20 eV and 55 eV) alongside the IMFP curve, it can be concluded that within the junction, band bending is slightly stronger in the FeTe region compared to the very surface.

One possible explanation for this is that in the case of measurements taken with 20 eV photons, the band bending scenario is stronger, and it is well-known that intense band bending can lead to the suppression of surface states. Another explanation, which has been a recurring theme throughout this work, involves the probing depth associated with the photon energy. If we consider the IMFP curve, it can be assumed that the probing depth for 20 eV photons is greater than that for 55 eV photons, where the probing depth is at its minimum on the curve. This suggests that the surface states in this system are strongly localized at the surface, and that Fe atoms may penetrate the material, reaching deeper layers either in the form of compounds or as additional atoms occupying the vdW gaps, Figure 51.

As shown in Figure 50, the ARPES 2D maps were also taken for the VB region. The main feature observed in these maps is the characteristic hexagonal shape of the bands mapped near the Fermi surface. Hexagonal warping of the Fermi surface occurs due to the interplay between

the crystal symmetry and the spin-orbit interaction, leading to an anisotropic (non-circular) Fermi surface. This effect can be observed in the M-shaped VB, surface states, and CB.

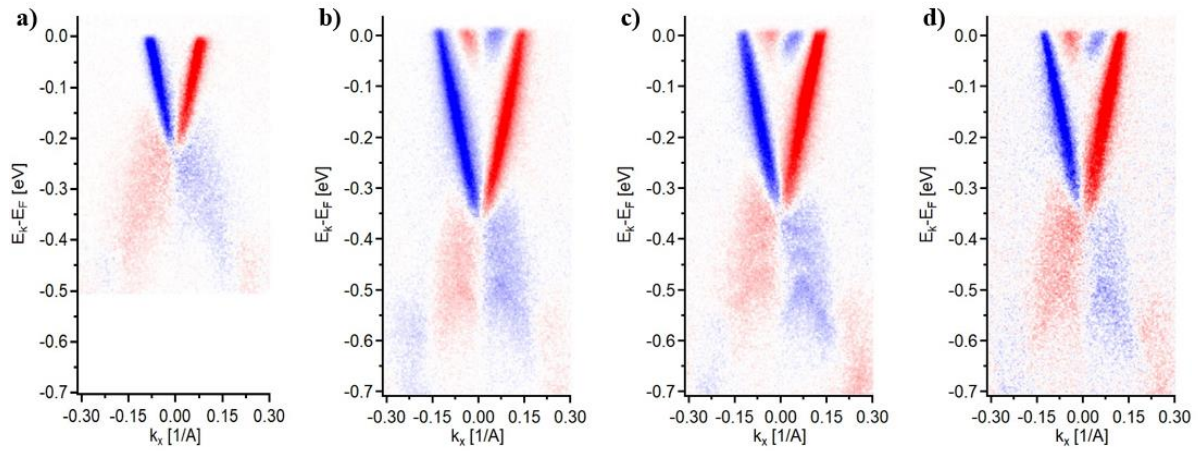


Figure 52 CD-ARPES data collected at 55 eV for Bi_2Te_3 under the deposition of Fe onto the surface show the evolution of the electronic structure. In a) the pristine sample is measured, serving as the reference. b) presents data after the deposition of 0.2 Å of Fe, revealing initial changes in the surface states. c) shows the data for 0.5 Å of Fe and d) displays the data for 0.8 Å of Fe.

To conclude the ARPES results for the Fe/ Bi_2Te_3 system, the CD-ARPES measurements must be discussed. For the pristine Bi_2Te_3 , the CD-ARPES data were consistent with previous studies, showing no unexpected results. The goal of this research was to experimentally observe a change in the sign of the CD signal, indicative of OAM in the electronic structure near the Fermi level, due to the influence of magnetic Fe. Unfortunately, or perhaps fortuitously, these studies revealed that the OAM response remains resistant to the chemical and structural changes introduced by the Fe deposition on the Bi_2Te_3 surface as shown in Figure 52. One of the interesting results is that the CB also exhibits differences in the CD measurements. This

suggests that strong SOC leads to significant spin polarization of the electrons within these quantized bands.

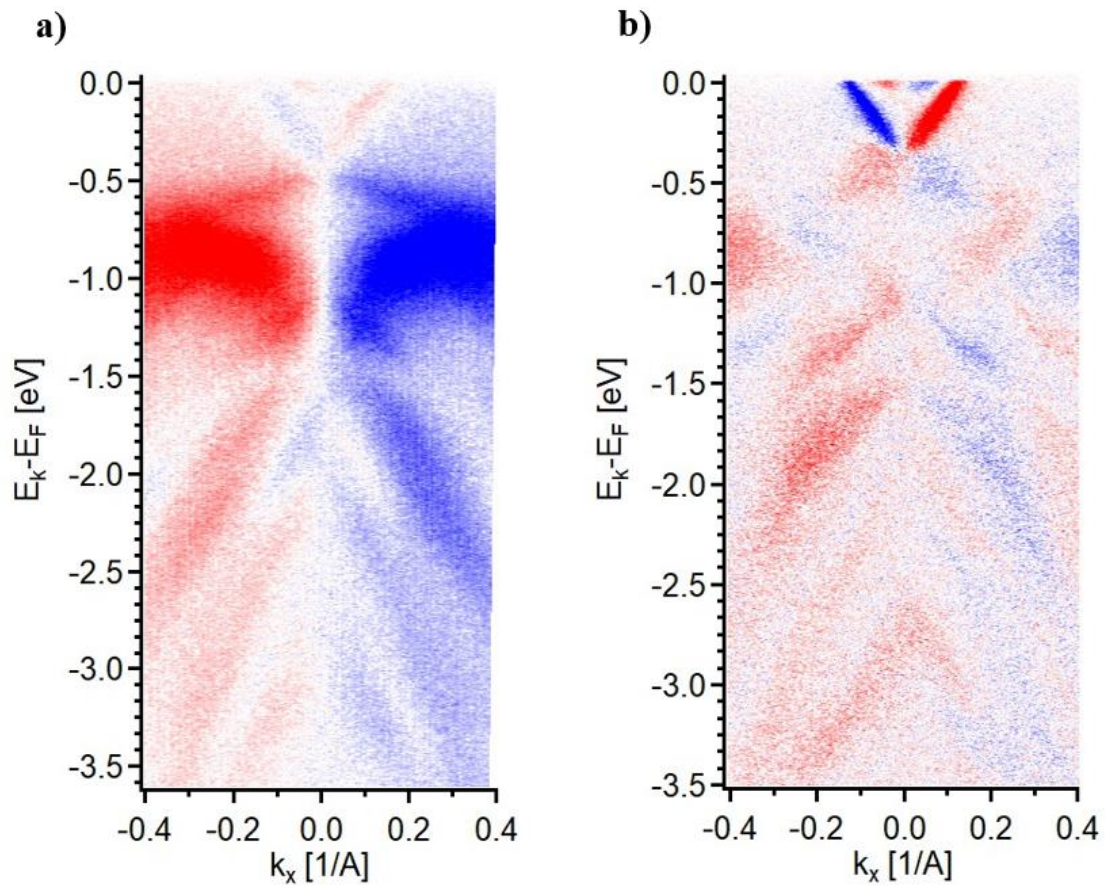


Figure 53 CD-ARPES data for the VB wide binding energy range measured a) for 51 eV and b) 55 eV.

No signal changes was observed for different excitation energies within the Fe3p core level range (from 50 eV to 55 eV) as shown in Figure 53. Combining data measured for the pristine material and the system with Fe it can be clearly see that CD sign is mostly related for different excitation energies. In this studies it is shown that this changes occurs in several region within photon range from 50 to 140 eV.

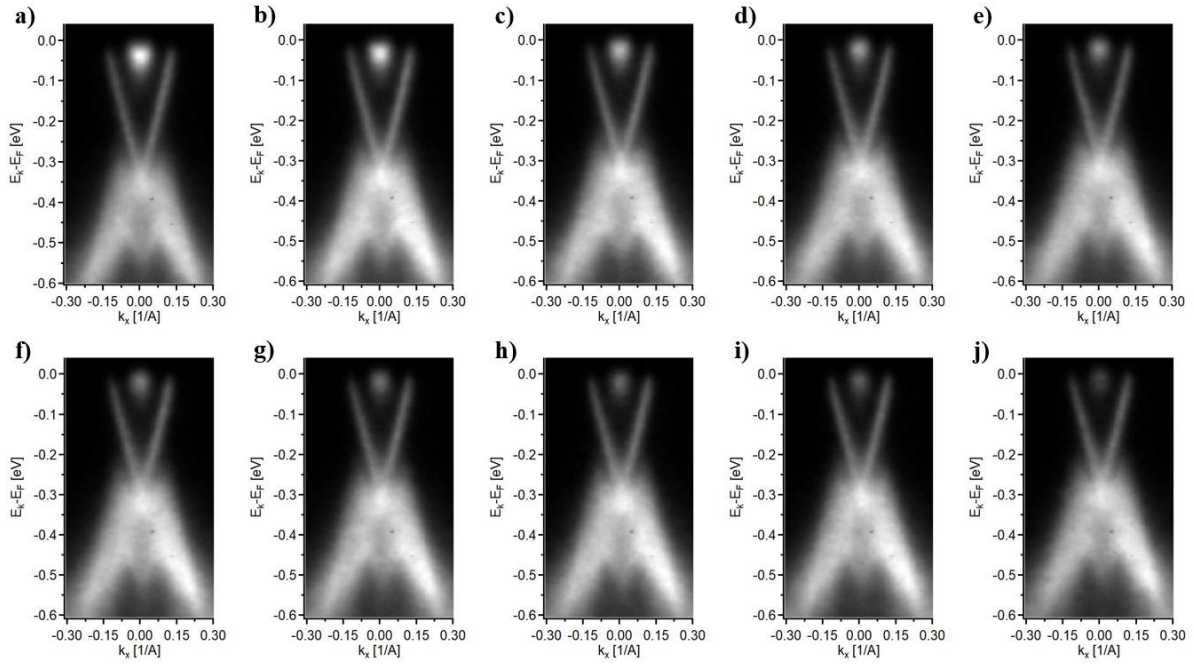


Figure 54 ARPES data collected at 120 eV for Bi_2Te_3 under the deposition of 0.2 \AA Fe. The clear evolution of the band structure occurs during the illumination of the surface and the upward shift in the chemical potential is observed. In a) spectra is taken first after few hours not illuminating the sample surface with the x-rays. From b) to j) spectra were collected from the same spot every two minutes.

The evolution of the electronic structure under x-ray illumination was presented and discussed for pristine Bi_2Te_3 in the earlier stages of this thesis. It was shown that, following the surface preparation process, the chemical potential shifts within just a few minutes, accompanied by a downward band shift that positions the Dirac point approximately 50 meV further below the Fermi level. After this initial shift, no further evolution was observed over the course of several hours.

In contrast, Figure 54 presents the electronic structure evolution under illumination with 120 eV photons for Bi_2Te_3 capped with Fe. In this case, the surface of the sample was not illuminated for approximately three hours. After that time the spectra in Figure 54 were taken. Each spectrum, starting from b) was taken every two minutes under consistent experimental parameters. Over the course of about 20 minutes, an upward shift in the chemical potential is observed, covering the electronic structure. This behavior is opposite to the effect previously reported in this thesis for pristine Bi_2Te_3 .

A possible explanation for this process is that, after Fe deposition, the vdW gaps near the surface become occupied by Fe adatoms, preventing the migration of gas adsorbates into these regions of the material. According to Figure 33, this upward band shift may occur when residual gas

molecules are ionized and subsequently desorbed from the surface. After 20 minutes of illumination, the Fe/Bi₂Te₃ system appears to stabilize, with a 50 meV upward shift of the chemical potential. These considerations are an attempt to explain the observed effect based on the data presented within this thesis.

4.3 Bi₂Te₃/Co system

During the research, an opportunity arose to repeat some of the experiments using a different transition metal. Co was chosen due to its similar properties and technical considerations. Two brief ARPES and XPS experiments were conducted on the PHELIX and URANOS beamlines. Cobalt has one more electron than Fe in its valence shell and is characterized by a lower magnetic moment and a higher Curie temperature compared to Fe. The experimental plan closely mirrored the one previously executed for Fe. Although prior studies have explored the use of Co as a potential dopant in Bi₂Te₃^{67,118} and Bi₂Se₃^{119–121} there is relatively little published data on Co/TI systems.

The experimental plan involving Co deposition on top of a Bi₂Te₃ single crystal was straightforward. The evaporation process was carried out under UHV conditions using a PREVAC-type EBV (deposition from the wire). In the URANOS experiment, the EBV was attached to the preparation chamber as auxiliary equipment, while in the PHELIX experiment, the Co evaporator was connected to the MBE system as standard equipment. In both cases, the deposition rate was calibrated using a quartz crystal microbalance. For the XPS experiment, the deposition rate was set at 0.3 Å/min, and the Co was deposited onto the Bi₂Te₃ material in three steps - 0.3 Å, 0.6 Å, and 1 Å - at room temperature. For the ARPES experiment on the URANOS beamline, the deposition was performed in four steps - 0.2 Å, 0.4 Å, 0.6 Å, and 1 Å - of Co onto the single crystal. In case of the XPS experiment, after each deposition process the ARPES scan was performed to check the quality of the surface, Appendix 2. It was expected when the surface states are visible the experiment can be carried on.

4.3.1 XPS studies

As previously mentioned, the three-step deposition process was carried out to achieve a final Co coverage of 1 Å on the surface of the Bi₂Te₃ single crystal. The evolution of the electronic structure during deposition was monitored using ARPES, CD-ARPES, and XPS. The XPS studies were conducted in the same manner as for the Fe system. Unfortunately, there was

not enough time to repeat all the steps as thoroughly as in the Fe case. However, the quantity and quality of the data obtained are sufficient to briefly discuss the results and draw conclusions.

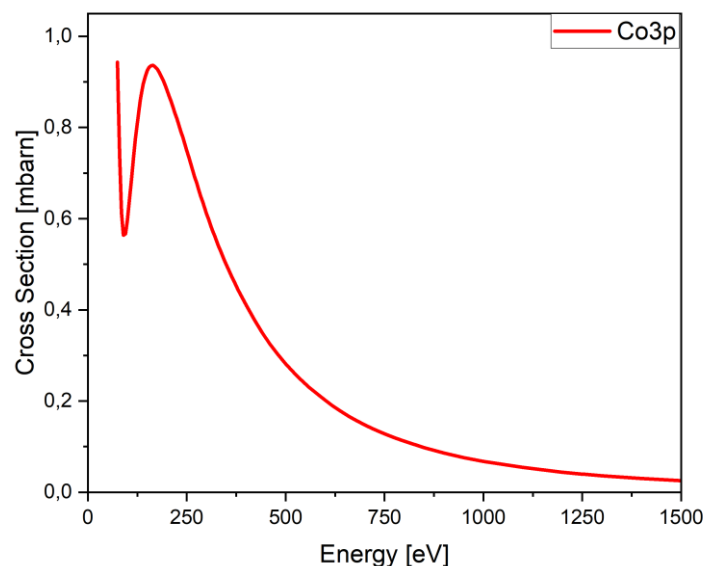


Figure 55 Photoionization cross sections vs photon energy calculated^{108,109} for Co3p core level.

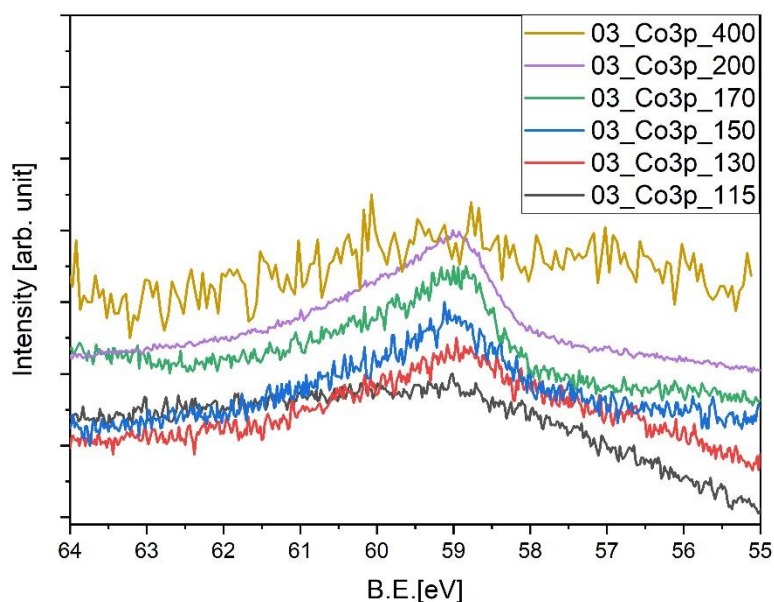


Figure 56 XPS data for the Co3p core level. The spectra shown here were measured from the same spot after the deposition of 0.3 Å of Co on the Bi₂Te₃ surface.

XPS depth profiling was performed. Similar to the Fe case, the cross-section parameter requires careful consideration. The Co3p core level was selected for detailed study using seven different excitation energies, ranging from 115 eV to 1000 eV. Before analyzing the data presented in

Figure 49, the photoionization cross-section of Co3p is discussed. The behavior is very similar to that of Fe3p, and the analysis of the Co3p core level intensity was conducted in the same manner as for Fe. The maximum of the Co3p cross section is placed in the energy range from 150 eV to 180 eV and for energy of 115 eV the value is 0.73 when for 200 eV is 0.88.

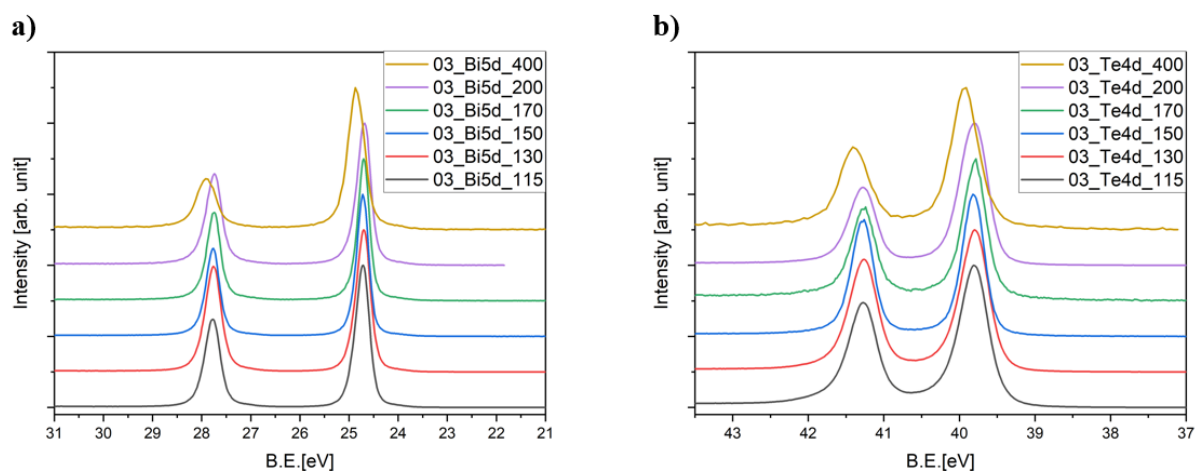


Figure 57 XPS spectra of the Bi5d and Te4d core levels were collected for a 0.3 Å Co deposited on the surface of Bi₂Te₃, in a photon energy range of 115 eV to 400 eV.

As shown in Figure 56, the Co3p core level was measured using a variety of excitation energies to obtain information about the chemical composition of the surface with 0.3 Å Co decoration. Analyzing these results, might draw the same conclusion as for Fe, suggesting that a migration process could be occurring in this case as well. Notably, the intensity of the Co3p core level at low Co coverage is higher compared to the low coverage of Fe atoms. However, this observation does not impact the Bi5d and Te4d core levels, as shown for 0.3 Å Co in Figure 57. The asymmetry in the Te4d core level start to be observed for the lowest excitation energies, but no additional components corresponding to metallic Bi are detected in the Bi5d core level either. These results are also consistent with those observed for the Fe system.

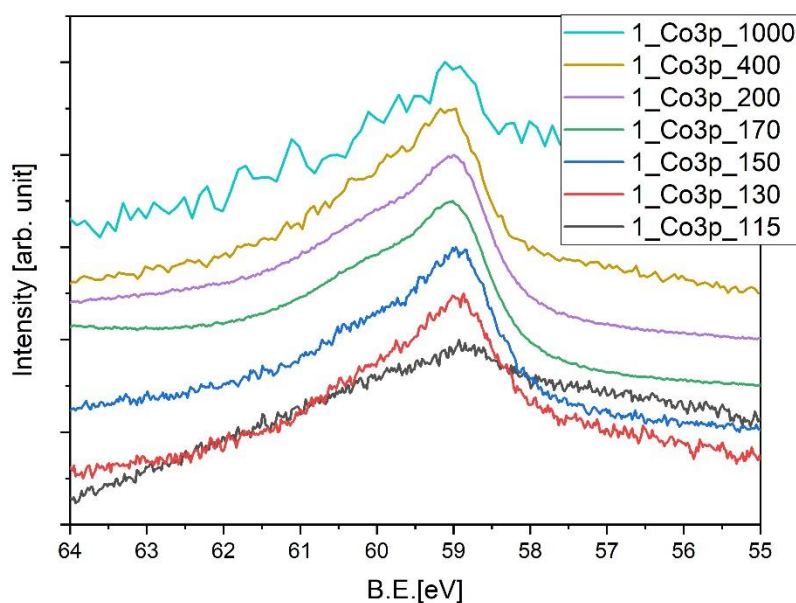


Figure 58 XPS data for the Co3p core level. The spectra shown here were measured from the same spot after the deposition of 1 Å of Co on the Bi₂Te₃ surface. The photon energy range was extended up to 1000 eV.

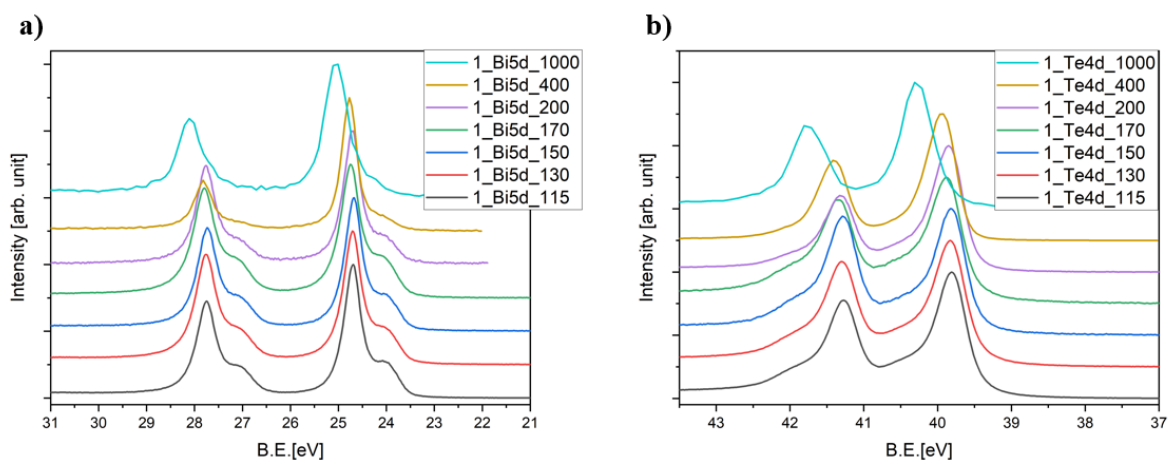


Figure 59 XPS spectra of the Bi5d and Te4d core levels were collected for a 1 Å Co deposited on the surface of Bi₂Te₃, in a photon energy range of 115 eV to 1000 eV.

The next deposition steps were carried out, and the corresponding spectra for Co3p, Bi5d, and Te4d were recorded. As shown in Figure 58 and Figure 59, the evolution of the electronic structure is significant, and features in the core levels that were barely detectable at 0.3 Å Co coverage are now clearly observed. Analyzing the Co3p core level, it is evident that as the photon energy increases, the intensity of the core level becomes higher and is detectable even at the highest energy of 1000 eV. When considering the same conditions and analytical parameters used for Fe, it can be stated that Co adatoms migrate into the Bi₂Te₃ structure, either

as adatoms or as substituent atoms in the lattice, forming an additional phase at the surface of the TI. To confirm this, an analysis of the Te and Bi core levels is necessary.

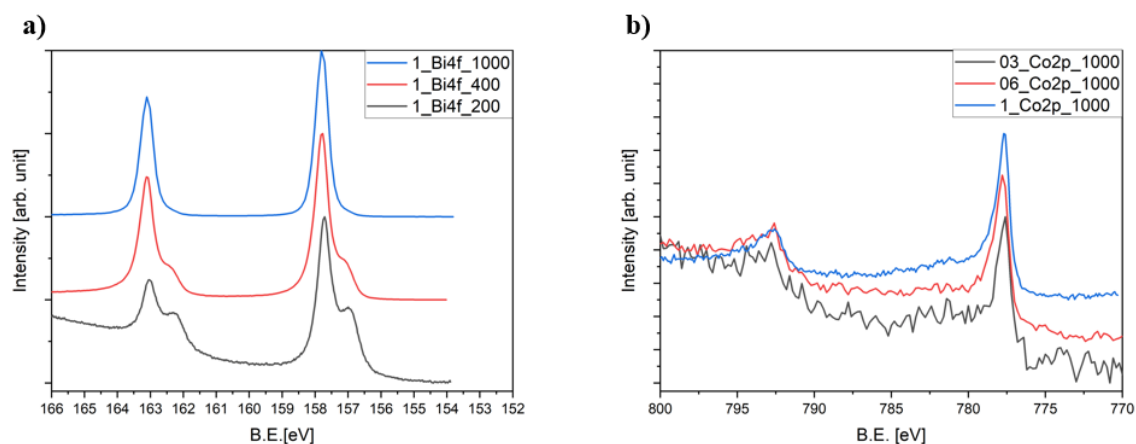


Figure 60 XPS spectra of the Bi4f core level are presented in a) for the Co total coverage of 1 Å, in a photon energy range of 115 eV to 1000 eV. In b) Co2p core level after subsequent depositions.

As Figure 59 presents, there are clear signs of a metallic bismuth component (binding energy of 24.0 eV) in the Bi5d core level, for low excitation energies which gradually diminishes as the energy increases. A strong asymmetry is detected in the Te4d core level. This additional phase likely arises from the migration of Co adatoms and the substitution of Bi atoms in the lattice by these adatoms. Although there is limited published data on this topic, the analysis of the multicomponent Te4d spectra indicates that the additional doublet component is shifted toward higher binding energies by 550 meV from the original Bi₂Te₃ peaks. This shift may be associated with the formation of a CoTe phase, where the higher binding energy shift in Co could be related to bonding with another metal¹²². Additional XPS data are presented in Figure 60. The analysis of the Bi4f core level confirms the presence of a metallic bismuth component at low excitation energies, which had been previously associated with a shallow probing depth compared to higher photon energies. According to the XPS data presented here, it can be assumed that the surface modification processes are very similar to those observed in the case of Fe deposition, where a metallic component of Bi was detected at the surface, and an additional phase, in this case, CoTe, likely formed.

4.3.2 ARPES and CD-ARPES studies

At the URANOS beamline, a full commitment to the ARPES experiment was made. The measurements were conducted at 100 K using photon energies of 20 eV and 55 eV, as shown in Figure 61 below. It is important to note that by this stage, the sample quality had deteriorated

compared to the beginning of the project. The repeated exfoliations, both in air and UHV, introduced significant surface roughness, which was visible to the naked eye. Despite this, it was still possible to locate a high-quality spot after exfoliation and perform the ARPES experiment.

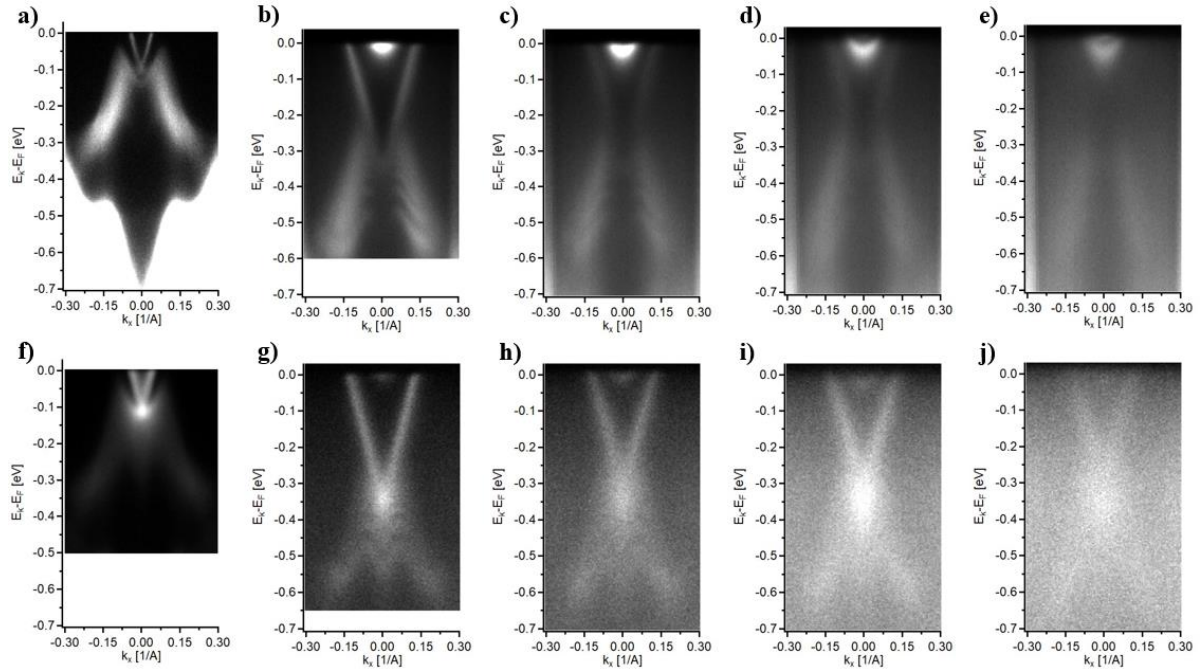


Figure 61 ARPES data were collected using a-e) 20 eV photons and f-j) 55 eV photons at 100 K to observe the evolution of the electronic band structure upon the deposition of Co atoms on the surface of Bi_2Te_3 . Picture a) and f) represent the spectra for the pristine material, serving as references. Picture b) and g) show data after the deposition of 0.2 Å of Co, c) and h) after 0.4 Å of Co, d) and i) after 0.6 Å of Co, and finally e) and j) after 1 Å of Co on the surface.

The data presented in Figure 61 are comparable to those collected for the Fe system. Band bending is observed, and according to results shown in Figure 61, the magnitude of the band bending is approximately 280 meV (considering residual gas absorption and X-ray effects on the material's surface). This value is lower than that observed for Fe, yet quantized subbands still exist in the modified material. This observation could contribute to the discussion on whether band bending must be larger than the valence band for quantization to occur. With further deposition, surface states begin to diminish for 20 eV photon energy, and quantized conduction band states become apparent (2DEG), similar to the Fe case. For 55 eV, surface states remain visible up to 1 Å of Co deposition, though the data quality is poorer which can indicate that Co adatoms could start occupied the surface of the material.

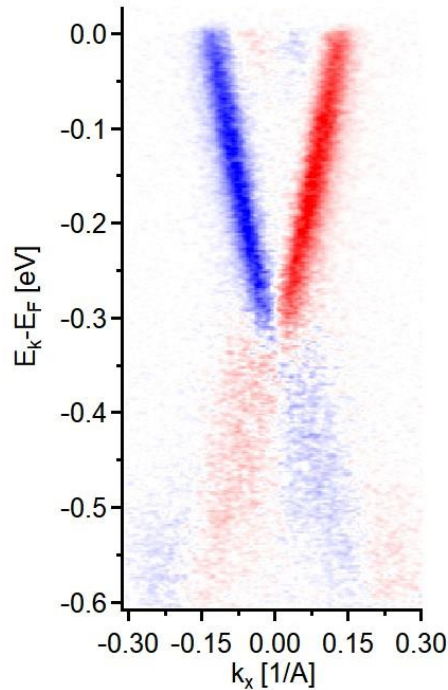


Figure 62 CD-ARPES data for 55 eV photon energy with 0.6 Å of Co deposition on Bi₂Te₃.

Finally, CD-ARPES measurements were conducted, with an example shown in Figure 62. The CD signal did not exhibit a change in sign, similar to the results observed for Fe deposition at an energy of 55 eV. It is understood that the photon energy of 55 eV may not be optimal for probing Co, as the Co3p core level is deeper within the electronic structure compared to Fe. Despite this, the measurements were performed, and no significant deviations from the results obtained with Fe were observed. This consistency suggests that the influence of Co on the CD signal, at this photon energy, is comparable to that of Fe.

However, to conclude the experimental section of this dissertation, I would like to highlight one intriguing result observed during the experiments with Co, as shown in Figure 63. The ARPES spectrum was collected at an energy of 120 eV for Bi₂Te₃ covered with 0.3 Å of Co. Upon analyzing this result, it appears that there is only one surface state, referred to as a chiral surface state, which is typically associated with the QAHE. This effect can occur in TIs when a magnetic material induces magnetic order to the system, thereby affecting the electronic structure through the proximity effect. Unfortunately, this particular result was obtained during a night shift, and the analysis was completed after the entire experiment was ended. There was an attempt to replicate this observation, but this structure was not detected in subsequent measurements.

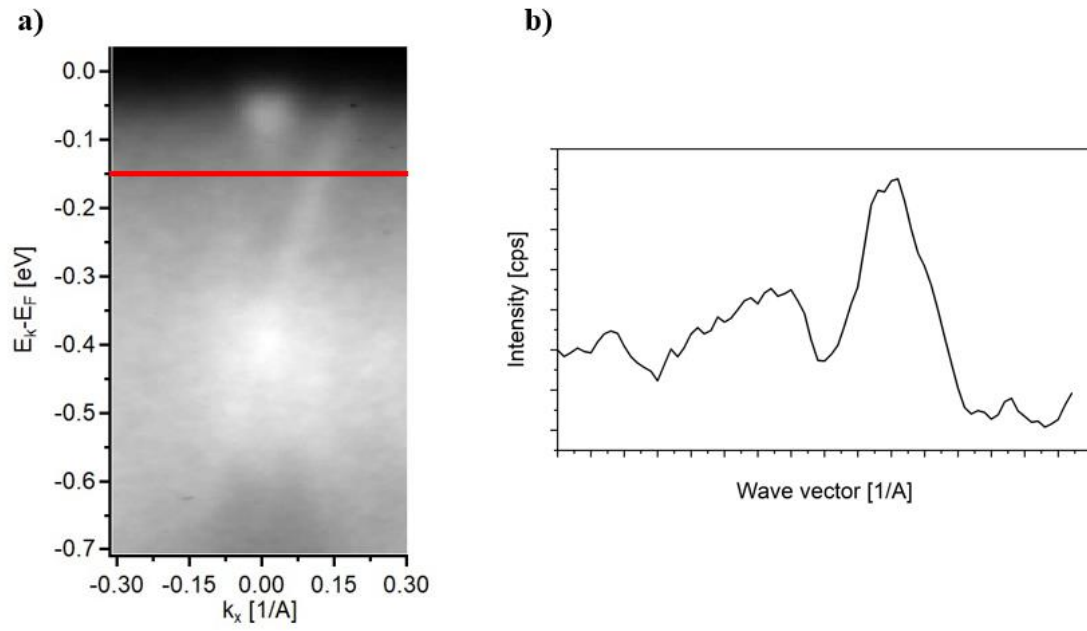


Figure 63 a) ARPES data collected with the horizontal polarized light for the energy of 120 eV for the 0.3 Å Co on the Bi_2Te_3 . In b) is presents the intensity profile within the red line mark in the ARPES spectra.

Chapter 5 Summary and perspectives

Final Chapter concludes the thesis with a summary and future perspectives. Section 5.1 recaps the key findings on the electronic structure and magnetic properties of Bi_2Te_3 covered with Fe and Co layers. Section 5.2 explores potential future directions for research, suggesting how the insights gained could be applied to further investigations and practical applications of magnetic topological insulators.

5.1 Summary

In my research, I focused on studying the electronic structure and magnetic properties of the three-dimensional topological insulator Bi_2Te_3 , with transition metals Fe and Co deposited on its surface using MBE. The goal was to investigate how the deposition of these transition metals affected the surface states, electronic structure, and magnetic properties of the resulting heterostructures. The research involved a reference Bi_2Te_3 crystal and two subsystems (one with Fe and the other with Co), where varying thicknesses of the respective transition metals, ranging from 0.2 Å to 1 Å, were deposited onto the Bi_2Te_3 crystal surface. Surface-sensitive experimental techniques utilizing synchrotron radiation, including ARPES, XPS, XAS, and CD-ARPES, were employed.

The ARPES data played a crucial role in this research, revealing significant differences in the electronic structure between the pristine and the metal-capped Bi_2Te_3 systems. The study showed that surface modification through low coverage with transition metals led to the emergence of quantum well states and n-type band bending, which had not been reported previously. In the Fe system, band bending reached as high as 375 meV, unveiling quantized conduction bands (also reported for Co). However, detailed experiments with the pristine material also revealed that the influence of the synchrotron radiation and processes such as absorption of residual gases can cause surface and structural modifications, leading to band bending and band splitting.

One of the primary goals of this thesis was to observe the opening of a band gap, which was not achieved. This suggests that the submonolayer interface formed by Fe and Co does not exhibit the expected magnetic properties. Nevertheless, in the case of Fe, magnetic properties were not observed in the XAS data. Additionally, at deposition levels of 1 Å, the surface states began to vanish (surface states were observed for 0.2 to 0.8 Å coverage), likely due to the increasing structural disorder after deposition.

To expand the ARPES studies of Bi_2Te_3 , CD-ARPES data were also collected. It was demonstrated that the CD signal within the VB did not change its sign with increasing amounts of deposited transition metals, particularly Fe. The CD signal near the $\text{Fe}3p$ transition showed no sign change, which was a key focus of this research. Further discussion of the CD-ARPES data, particularly regarding OAM probing, would require more complex models of photoemission that were not explored in this thesis.

XPS studies provided information on the chemical composition of the Bi_2Te_3 surface and interlayer stability, both with and without modification. The measurements revealed the presence of three chemically distinct regions on the surface after Fe and Co deposition. The results indicated the existence of iron-telluride and cobalt-telluride compounds, as well as a Bi-rich region at the top of the formed interfaces. Concluding the XPS research, we found that deep-profiling using synchrotron radiation is a powerful tool for investigating changes in the electronic structure at phase boundaries or manufactured interfaces.

Despite the tremendous advantages of synchrotron radiation in electronic structure studies - such as tunable photon energies, high energy resolution, high photon flux, and small beam spots - the results of my investigation reveal several challenges to consider when probing photoelectrons. One of the main issues is radiation damage due to the high photon flux, which can modify the electronic structure within the first few seconds or minutes of exposure. Additionally, surface adsorption of residual gas molecules can lead to chemical modifications. Theoretical experiment preparation, such as understanding the IMFP curve and photoionization cross-section parameters for specific elements, also plays a crucial role in the use of synchrotron radiation. Furthermore, technical limitations, such as the transmission functions of photoelectron analyzers, may not be well-suited for a wide range of excitation energies.

Ultimately, while synchrotron radiation offers numerous benefits for studying electronic structure and magnetic properties, data collection and analysis remain challenging. A great deal of care must be taken when interpreting the synchrotron results. I believe that this thesis sheds light on some of the challenges encountered during synchrotron experiments and offers potential solutions for addressing them.

5.2 Perspectives

Although this study has focused on the well-known topological material Bi_2Te_3 , much remains to be done to fully understand interface formation and the resulting changes in the electronic structure. Based on my experience during the experimental phase of this thesis, I have come to

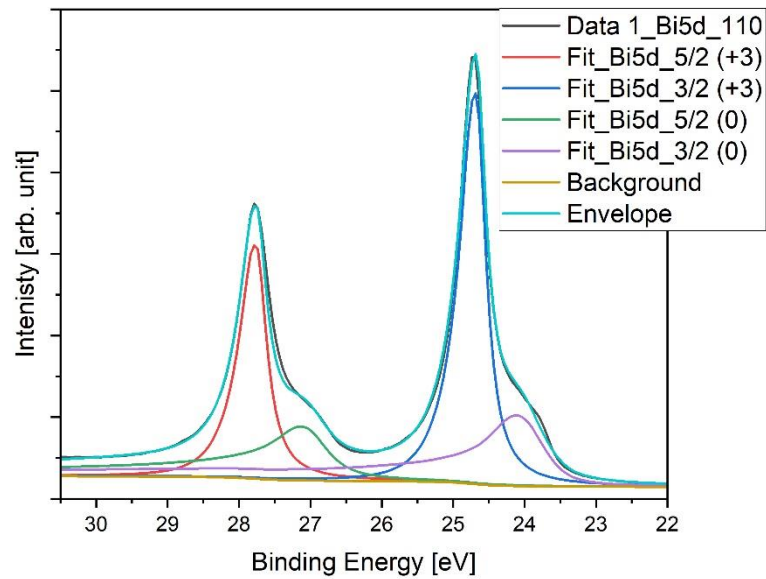
realize that proper theoretical calculations should be performed prior to experimental work. Band structure calculations, through methods like DFT, are becoming increasingly accessible even to experimentalists and are essential for band structure studies. This is particularly important in synchrotron research, where high energy resolution spectra can be obtained, enabling more detailed analysis.

One significant limitation of this thesis is the lack of diffraction data, such as LEED measurements, taken before and after the deposition processes. LEED data could have greatly enhanced our understanding of surface structure and morphology providing additional insights into surface quality during interface formation.

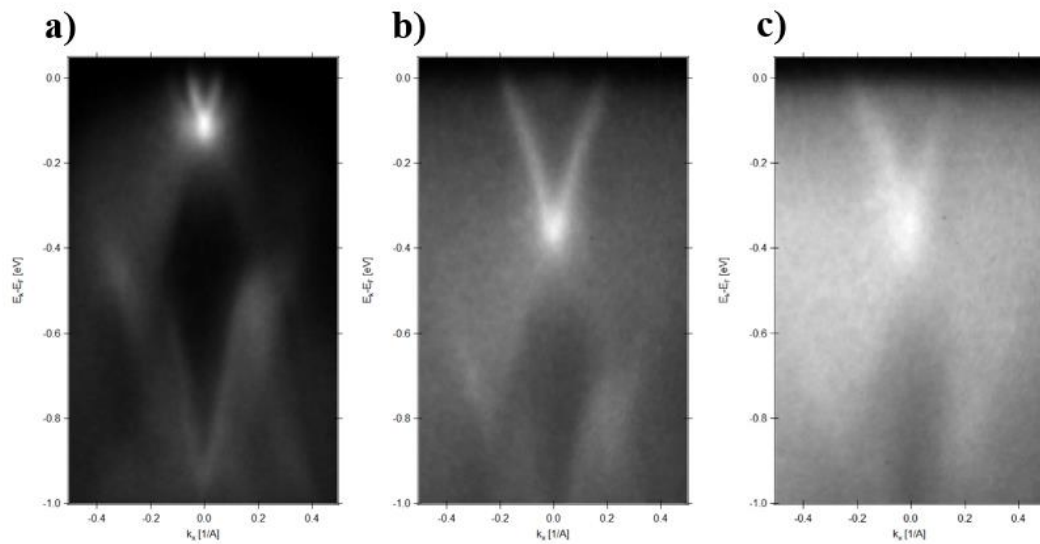
Moreover, deposition parameters such as deposition rate, substrate temperature, and UHV conditions during the process should be carefully optimized to ensure the highest possible interface quality. Maintaining ultra-pure vacuum conditions during the preparation process and ideal selection of the conditions for the formation of the interface could allow for a thicker growth of the transition metal layer and the potential formation of a monolayer on the surface of the topological insulator, which could ultimately exhibit magnetic properties. With the optimization of heterostructure growth and further studies probing its electronic structure, investigations into other properties of magnetic topological insulators using various measurement techniques can subsequently be pursued.

Despite these considerations, Bi_2Te_3 remains a promising material for future advanced electronic, spintronic, and orbitronic applications due to position of the Dirac point near the Fermi level, ease of surface preparation, and excellent thermoelectric properties.

Appendix



Appendix 1 XPS data collected for Bi_2Te_3 capped with 1 Å of Fe fitted with Gaussian-Lorentz conjugation (+3) and Doniach – Sunjić (0). The position of the metallic component (0) for Bi5d 5/2 is 24.72 eV (Binding Energy).



Appendix 2 ARPES data collected with 50 eV photons for Bi_2Te_3 capped with Co, a) pristine, b) 0.3 Å of Co and c) 0.6 Å of Co.

List of figures

- Figure 1 The SOLARIS mug and the Krakow pretzel are topologically indistinguishable because they share the same genus value of 1 (number of holes) and can be smoothly transformed into each other. In contrast, the German pretzel has a genus value of 3, making it topologically distinct, meaning that neither the mug nor the Krakow pretzel can be smoothly transformed into the German pretzel in a topological sense. 5
- Figure 2 A simple illustrative presentation of the phenomena driving topological insulators and the existence of surface states. In a trivial insulator, parabolic conduction and valence bands (p-type) are distinguishable a), with the Fermi level located in the gap between these two bands. In materials with a high atomic number Z , the bands near high-symmetry points, such as Γ , can cross (b) in the absence of spin-orbit coupling (SOC). When SOC is present, this band crossing becomes unstable, leading to the opening of a gap, resulting in a non-trivial insulator with inversion symmetry, where the chemical potential is situated in the gap c). In d), the transition between a non-trivial insulator (left) and a trivial insulator (right, vacuum) is depicted. At the trivial-non-trivial interface, the transition is not smooth (different Chern number), necessitating the closure of the gap, which leads to the existence of surface states at the surface of the material, as shown in d). 11
- Figure 3 Layered CdTe/HgTe/CdTe quantum-well structures a). Longitudinal resistance of various quantum-well structures as a function of the gate voltage measured in zero magnetic field at 30 mK b). Structures show quantized conductance of $2e^2h$, giving evidence for the 2D TI phase^{17,18}. 12
- Figure 4 ARPES measurement of the topological gapless surface states in bulk insulating $\text{Bi}_{0.9}\text{Sb}_{0.1}$ ²⁰. 13
- Figure 5 Bi_2Se_3 surface states, ARPES data collected for Γ -M a) and Γ -K b) direction along the BZ²⁹. 14
- Figure 6 Bi-Te phase diagram^{41,42}. 16
- Figure 7 Bi_2Te_3 crystal structure. a) hexagonal unit cell⁴³, b) the Brillouin zone of the rhombohedral cell⁴⁴ and c) is the Bi_2Te_3 2D Brillouin zone. 17
- Figure 8 Bi_2Te_3 , DFT (LDA), band structure calculation for a) bulk and b) slab. Red and blue lines indicates calculation with and without SOC, respectively⁴⁷. 18
- Figure 9 ARPES spectra collected for single crystal Bi_2Te_3 with excitation energy of 55 eV. a) to d) is the surface states behavior under deposition of Fe. 19
- Figure 10 Circular dichroism effect measured for Bi_2Te_3 with ARPES. ARPES data a - d) show sign change of the effect with energy range from 21 to 100 eV. e) is the plot of the circular dichroism sign for different excitation energies. 21
- Figure 11 Illustrative example of a standard MBE chamber with two types of material sources in a). b) presenting the thermal deposition process. The deposition is carried out in a UHV environment.

The material is heated by e.g. resistive heating, and the evaporated material is directed onto the substrate.....	23
Figure 12 Illustrative example of atomic processes that drive film growth during thermal deposition onto a solid substrate ⁷¹	25
Figure 13 The mechanical exfoliation process using scotch tape: The tape is applied to the material's surface, a), and then, with applied force, it is peeled off, b). This removes a few layers of the sample, revealing a fresh surface.....	27
Figure 14 a) LEED standard setup and b) LEED pattern recorded from the clean Mo(110) surface ⁷² .	28
Figure 15 Relationship between the energy levels in the solid and the electron energy distribution produced by photons with energy $h\nu$	30
Figure 16 Scheme of the direct (vertical) transition between the initial and final states in the reduced zone ⁷⁷	33
Figure 17 Universal curve for inelastic mean free path of electrons ^{71,78}	34
Figure 18 Hemispherical electron analyzer and the working principle of the standard ARPES.....	36
Figure 19 Standard XAS measurement setup a) and b) is a typical XAS spectrum with highlighted the near-edge structure (XANES) and extended absorption fine structure (EXAFS) ⁷⁹	38
Figure 20 Radiation beam emission from the magnetic insertion device such as wigglers or undulators ⁸¹	46
Figure 21 Omicron flag style holder compatible with the PHELIX and URANOS systems. Bi ₂ Te ₃ single crystal is placed in the middle of the holder and attached by the UHV glue.....	49
Figure 22 LEED pattern measured for pristine Bi ₂ Te ₃ at the electron energy of 69 eV. The double bright spots can implicate that the surface of the TI absorb the residual gas molecules and the superstructure could form at the very top of Bi ₂ Te ₃	51
Figure 23 XPS survey measurement of the Bi ₂ Te ₃ single crystal taken for photon energy of 850 eV.	53
Figure 24 XPS data collected for Bi ₂ Te ₃ . a) Bi5d and b) Te4d core levels analysis.....	54
Figure 25 XPS spectra of Te4d and Bi5d were collected for various photon energies: a-d) Te4d core levels for 115 eV, 150 eV, 400 eV, and 850 eV, respectively; e-h) Bi5d core levels for 115 eV, 150 eV, 400 eV, and 850 eV, respectively.....	55
Figure 26 A photon energy of 850 eV provides access to deeper core levels of Te and Bi: a) Te3d, b) Bi4d, and c) Bi4f.....	56
Figure 27 XPS data for C1s and O1s core levels for a pristine single crystal of Bi ₂ Te ₃ were collected at 850 eV. The data presented in a) show the C1s core level after illuminating the sample surface for several minutes following sample preparation in the UHV. Spectrum b) shows the intensity of the C1s after approximately 12 hours of illumination. Spectrum c) shows the O1s, which does not change after several hours of exposure to X-rays.....	57
Figure 28 IMFP calculated ⁸⁸ for few elements included a) Fe and b) Bi.	59

Figure 29 ARPES data collect with 20 eV photon energy in the Γ -K direction for wide binding energy range to illustrate a large VB area a). b) presents a band structure near the fermi level with the visible surface states in the range of 100 meV below Fermi level. Data were collected at 40 K. 61

Figure 30 a) Represents the calculated bulk conduction band (BCB) and bulk valence band (BVB) dispersions along high-symmetry directions of the surface Brillouin zone for Bi_2Te_3 ³². b) Shows the Bi_2Te_3 spectra collected using 55 eV photons..... 63

Figure 31 ARPES data collected for pristine Bi_2Te_3 . Spectra a) and c) represent the electronic structure near the Fermi level measured within the first few hours after the initial illumination of the sample surface with photon energies of 20 eV and 55 eV, respectively. Spectra b) and d) show the same data collected after the entire set of measurements was completed overnight. The "aging" process is evident, as the position of the Dirac point shifts towards higher binding energies. 64

Figure 32 Illustrative representation of the band bending scenario in Bi_2Te_3 driven by residual gas (RG) adatom surface decoration (and absorption) and the influence of radiation. The chemical potential is positioned near the Dirac point in the bulk, and when an interface is created at the surface, the bands shift downward (n-type doping), placing the Fermi level near the CBM..... 65

Figure 33 An illustrative explain proposition of the "aging" effect after exposure to residual gases and the UV light (27 eV) is demonstrated using the TI BiSbTeSe_2 from⁹³. In the first step, the sample is cleaved in UHV and can be considered pristine. Within a few seconds of exposure to UHV, residual gas molecules begin to cover the freshly cleaved surface. In the third step, the first photons reach the sample surface, and measurements starts. At this point, a downward band bending scenario begins as photodissociation of molecules starts to occur. The electronic structure shifts towards lower binding energies, which can lead to the unrevailing of the CBM. Eventually (4th stage), most of the molecules become ionized, and maximum band bending is achieved. In the final stage, desorption of the ionized adatoms can occur, leading to upward band bending and partial restoration of the original band structure. 66

Figure 34 CD-ARPES data collected for a Bi_2Te_3 single crystal. In (a) and (c), ARPES spectra are shown for horizontally polarized light with photon energies of 50 eV and 55 eV, respectively, in the Γ -K direction. The corresponding CD signals are presented in (b) for 50 eV and (d) for 55 eV light. Presented data were collect at the URANOS beamline at 40 K. 68

Figure 35 CD-ARPES data were collected for a Bi_2Te_3 single crystal for wide photon energy range up to 180 eV at the PHELIX beamline at 80 K. Spectra a) was measured for 55 eV, b) for 115 eV and c) for 180 eV. 69

Figure 36 CD-ARPES measurements were performed on pristine Bi_2Te_3 for various photon energies: a) 50 eV, b) 80 eV, c) 95 eV, d) 100 eV, e) 115 eV, f) 120 eV, g) 130 eV, and h) 140 eV. The variation in the CD signal's sign with changes in excitation energy was studied across different energy ranges and was reported in⁶⁹. 70

Figure 37 XPS survey spectra were collected with photon energy of 850 eV and temperature of 40 K.
(a) The spectra were measured for 0.2 Å of Fe on top of Bi₂Te₃, and (b) for 0.5 Å of Fe. 72

Figure 38 XPS survey spectra were collected at 850 eV for 1 Å of Fe atoms on Bi₂Te₃. The red markers indicate the positions of the Fe 2p and Fe 3p core levels, which are the main points of further analysis. 74

Figure 39 XPS data for the Fe3p core level. The spectra shown here were measured from the same spot after the deposition of 0.2 Å of Fe on the Bi₂Te₃ surface. The use of a wide photon energy range allows for variation in probing depth, providing detailed information about the chemical composition of the produced interface..... 75

Figure 40 Photoionization cross sections vs photon energy calculated^{108,109} for Fe3p core level. 76

Figure 41 XPS data for the Fe3p core level. The spectra shown here were measured from the same spot after the deposition of 1 Å of Fe on the Bi₂Te₃ surface. 78

Figure 42 a) XPS spectra of the Te4d core level were collected across a photon energy range of 100 eV to 850 eV. The observed asymmetric shape of the core level peaks b-d) suggests that Te forms additional phases during the sample preparation and measurement processes..... 79

Figure 43 XPS spectra of the Te4d core level were collected for a 0.2 Å Fe deposited on the surface of Bi₂Te₃, in a photon energy range of 115 eV to 850 eV. 80

Figure 44 XPS spectra of the Bi5d core level were collected for a summary of 1 Å Fe deposited on the surface of Bi₂Te₃, in a photon energy range of 100 eV to 850 eV. 81

Figure 45 The XPS and XAS spectra collected for Bi₂Te₃ capped with 1 Å of Fe. The Fe2p core level was measured using XPS at an excitation energy of 850 eV, as shown in a). In b), the XAS spectra of the Fe L-edge are presented, measured using right- and left-circularly polarized light (red and blue, respectively). XAS data were normalized to the mirror current to get the counts (beamline diagnostic device). 82

Figure 46 The illustrative proposition of the Fe atoms deposition influence at the Bi₂Te₃ surface structure. 83

Figure 47 ARPES data were collected using a-e) 20 eV photons and f-j) 55 eV photons at 40 K to observe the evolution of the electronic band structure upon the deposition of Fe atoms on the surface of Bi₂Te₃. Picture a) and f) represent the spectra for the pristine material, serving as references. Picture b) and g) show data after the deposition of 0.2 Å of Fe, c) and h) after 0.5 Å of Fe, d) and i) after 0.8 Å of Fe, and finally e) and j) after 1 Å of Fe on the surface. 84

Figure 48 The black (20 eV photons) and red (55 eV photons) triangles in this figure highlight the observed shift of the Dirac point in the electronic structure of Bi₂Te₃ under Fe capping. These markers clearly indicate the extent of the energy shift, providing a visual representation of the band bending effect as Fe atoms are deposited onto the surface of the topological insulator. 85

Figure 49 ARPES data collected for Bi_2Te_3 capped with 0.8 Å of Fe. The blue lines indicate the surface states, the yellow dot marks CBM1, and the green dot marks CBM2. The red dots indicate the 5 split bands in the M-shape VB..... 87

Figure 50 ARPES map collected, for Bi_2Te_3 covered with 0.5 Å of Fe, using 20 eV photons. In panel a), the Fermi level is shown near 0.0 eV binding energy, with two bands appearing near the Γ point identified as CBM1 and CBM2. The outermost structures represent the surface states. b) presents a cut near CBM1, and c) shows a cut near the Dirac point, where the M-shaped subbands are visualized..... 88

Figure 51 Illustrative representation of the band bending scenario in Bi_2Te_3 driven by the deposition of a transition metal (Fe in this case) on the surface of the TI. Based on the ARPES and XPS data, the surface can be divided into two regions: one rich in metallic Bi and another where the FeTe phase occurs. Analyzing the energy-dependent ARPES spectra (20 eV and 55 eV) alongside the IMFP curve, it can be concluded that within the junction, band bending is slightly stronger in the FeTe region compared to the very surface..... 89

Figure 52 CD-ARPES data collected at 55 eV for Bi_2Te_3 under the deposition of Fe onto the surface show the evolution of the electronic structure. In a) the pristine sample is measured, serving as the reference. b) presents data after the deposition of 0.2 Å of Fe, revealing initial changes in the surface states. c) shows the data for 0.5 Å of Fe and d) displays the data for 0.8 Å of Fe. 90

Figure 53 CD-ARPES data for the VB wide binding energy range measured a) for 51 eV and b) 55 eV. 91

Figure 54 ARPES data collected at 120 eV for Bi_2Te_3 under the deposition of 0.2 Å Fe. The clear evolution of the band structure occurs during the illumination of the surface and the upward shift in the chemical potential is observed. In a) spectra is taken first after few hours not illuminating the sample surface with the x-rays. From b) to j) spectra were collected from the same spot every two minutes..... 92

Figure 55 Photoionization cross sections vs photon energy calculated^{108,109} for Co3p core level..... 94

Figure 56 XPS data for the Co3p core level. The spectra shown here were measured from the same spot after the deposition of 0.3 Å of Co on the Bi_2Te_3 surface..... 94

Figure 57 XPS spectra of the Bi5d and Te4d core levels were collected for a 0.3 Å Co deposited on the surface of Bi_2Te_3 , in a photon energy range of 115 eV to 400 eV..... 95

Figure 58 XPS data for the Co3p core level. The spectra shown here were measured from the same spot after the deposition of 1 Å of Co on the Bi_2Te_3 surface. The photon energy range was extend up to 1000 eV. 96

Figure 59 XPS spectra of the Bi5d and Te4d core levels were collected for a 1 Å Co deposited on the surface of Bi_2Te_3 , in a photon energy range of 115 eV to 1000 eV..... 96

Figure 60 XPS spectra of the Bi4f core level are presented in a) for the Co total coverage of 1 Å, in a photon energy range of 115 eV to 1000 eV. In b) Co2p core level after subsequent depositions. 97

Figure 61 ARPES data were collected using a-e) 20 eV photons and f-j) 55 eV photons at 100 K to observe the evolution of the electronic band structure upon the deposition of Co atoms on the surface of Bi₂Te₃. Picture a) and f) represent the spectra for the pristine material, serving as references. Picture b) and g) show data after the deposition of 0.2 Å of Co, c) and h) after 0.4 Å of Co, d) and i) after 0.6 Å of Co, and finally e) and j) after 1 Å of Co on the surface. 98

Figure 62 CD-ARPES data for 55 eV photon energy with 0.6 Å of Co deposition on Bi₂Te₃..... 99

Figure 63 a) ARPES data collected with the horizontal polarized light for the energy of 120 eV for the 0.3 Å Co on the Bi₂Te₃. In b) is presents the intensity profile within the red line mark in the ARPES spectra. 100

Bibliography

1. Kosterlitz, J. M., D. Haldane, & D. J. Thouless. Topological phase transitions and topological phases of matter.
2. Haldane, F. D. M. Model for a Quantum Hall Effect without Landau Levels: Condensed-Matter Realization of the ‘Parity Anomaly’. *Phys. Rev. Lett.* **61**, 2015–2018 (1988).
3. The theory of electronic semi-conductors. *Proc. R. Soc. Lond. A* **133**, 458–491 (1931).
4. Hoddson, L., Baym, G. & Eckert, M. The development of the quantum-mechanical electron theory of metals: 1928—1933. *Rev. Mod. Phys.* **59**, 287–327 (1987).
5. Klitzing, K. V., Dorda, G. & Pepper, M. New Method for High-Accuracy Determination of the Fine-Structure Constant Based on Quantized Hall Resistance. *Phys. Rev. Lett.* **45**, 494–497 (1980).
6. Thouless, D. J., Kohmoto, M., Nightingale, M. P. & Den Nijs, M. Quantized Hall Conductance in a Two-Dimensional Periodic Potential. *Phys. Rev. Lett.* **49**, 405–408 (1982).
7. Novoselov, K. S. *et al.* Two-dimensional gas of massless Dirac fermions in graphene. *Nature* **438**, 197–200 (2005).
8. Halperin, B. I. Quantized Hall conductance, current-carrying edge states, and the existence of extended states in a two-dimensional disordered potential. *Phys. Rev. B* **25**, 2185–2190 (1982).
9. Kane, C. L. & Mele, E. J. Quantum Spin Hall Effect in Graphene. *Phys. Rev. Lett.* **95**, 226801 (2005).
10. Kane, C. L. & Mele, E. J. Z₂ Topological Order and the Quantum Spin Hall Effect. *Phys. Rev. Lett.* **95**, 146802 (2005).
11. Fu, L., Kane, C. L. & Mele, E. J. Topological Insulators in Three Dimensions. *Phys. Rev. Lett.* **98**, 106803 (2007).

12. Moore, J. E. & Balents, L. Topological invariants of time-reversal-invariant band structures. *Phys. Rev. B* **75**, 121306 (2007).
13. Roy, R. Topological phases and the quantum spin Hall effect in three dimensions. *Phys. Rev. B* **79**, 195322 (2009).
14. Volkov, B. A. & Pankratov, O. A. Inverted contact in semiconductors—a new inhomogeneous structure with a two-dimensional gas of zero-mass electrons. *Sov. Phys. Usp.* **29**, 579–581 (1986).
15. Fu, L. & Kane, C. L. Topological insulators with inversion symmetry. *Phys. Rev. B* **76**, 045302 (2007).
16. Bernevig, B. A., Hughes, T. L. & Zhang, S.-C. Quantum Spin Hall Effect and Topological Phase Transition in HgTe Quantum Wells. *Science* **314**, 1757–1761 (2006).
17. König, M. *et al.* Quantum Spin Hall Insulator State in HgTe Quantum Wells. *Science* **318**, 766–770 (2007).
18. Cayssol, J. & Fuchs, J. N. Topological and geometrical aspects of band theory. *J. Phys. Mater.* **4**, 034007 (2021).
19. Altland, A. & Zirnbauer, M. R. Nonstandard symmetry classes in mesoscopic normal-superconducting hybrid structures. *Phys. Rev. B* **55**, 1142–1161 (1997).
20. Hsieh, D. *et al.* A topological Dirac insulator in a quantum spin Hall phase. *Nature* **452**, 970–974 (2008).
21. Hsieh, D. *et al.* Observation of Unconventional Quantum Spin Textures in Topological Insulators. *Science* **323**, 919–922 (2009).
22. Hasan, M. Z. & Kane, C. L. *Colloquium* : Topological insulators. *Rev. Mod. Phys.* **82**, 3045–3067 (2010).
23. Moore, J. E. The birth of topological insulators. *Nature* **464**, 194–198 (2010).
24. Moore, J. The next generation. *Nature Phys* **5**, 378–380 (2009).

25. Zhang, H. *et al.* Topological insulators in Bi₂Se₃, Bi₂Te₃ and Sb₂Te₃ with a single Dirac cone on the surface. *Nature Phys* **5**, 438–442 (2009).
26. Hsieh, D. *et al.* A tunable topological insulator in the spin helical Dirac transport regime. *Nature* **460**, 1101–1105 (2009).
27. Park, S. R. *et al.* Quasiparticle scattering and the protected nature of the topological states in a parent topological insulator Bi₂Se₃. *Phys. Rev. B* **81**, 041405 (2010).
28. Hor, Y. S. *et al.* p -type Bi₂Se₃ for topological insulator and low-temperature thermoelectric applications. *Phys. Rev. B* **79**, 195208 (2009).
29. Xia, Y. *et al.* Observation of a large-gap topological-insulator class with a single Dirac cone on the surface. *Nature Phys* **5**, 398–402 (2009).
30. Ando, Y. Topological Insulator Materials. *J. Phys. Soc. Jpn.* **82**, 102001 (2013).
31. Knez, I., Du, R.-R. & Sullivan, G. Evidence for Helical Edge Modes in Inverted InAs / GaSb Quantum Wells. *Phys. Rev. Lett.* **107**, 136603 (2011).
32. Chen, Y. L. *et al.* Experimental Realization of a Three-Dimensional Topological Insulator, Bi₂Te₃. *Science* **325**, 178–181 (2009).
33. Jiang, Y. *et al.* Landau Quantization and the Thickness Limit of Topological Insulator Thin Films of Sb₂Te₃. *Phys. Rev. Lett.* **108**, 016401 (2012).
34. Zhang, J. *et al.* Band structure engineering in (Bi_{1-x}Sb_x)₂Te₃ ternary topological insulators. *Nat Commun* **2**, 574 (2011).
35. Ji, H. *et al.* Bi₂Te_{1.6}S_{1.4}: A topological insulator in the tetradymite family. *Phys. Rev. B* **85**, 201103 (2012).
36. Souma, S. *et al.* Topological Surface States in Lead-Based Ternary Telluride Pb (Bi_{1-x} Sb_x)₂Te₄. *Phys. Rev. Lett.* **108**, 116801 (2012).
37. Tanaka, Y. *et al.* Experimental realization of a topological crystalline insulator in SnTe. *Nature Phys* **8**, 800–803 (2012).

38. Xu, S.-Y. *et al.* Observation of a topological crystalline insulator phase and topological phase transition in $\text{Pb}_{1-x}\text{Sn}_x\text{Te}$. *Nat Commun* **3**, 1192 (2012).
39. Greenaway, D. L. & Harbeke, G. Band structure of bismuth telluride, bismuth selenide and their respective alloys. *Journal of Physics and Chemistry of Solids* **26**, 1585–1604 (1965).
40. Yang, L., Chen, Z., Dargusch, M. S. & Zou, J. High Performance Thermoelectric Materials: Progress and Their Applications. *Advanced Energy Materials* **8**, 1701797 (2018).
41. H. Okamoto, L. E. Tanner. Bi-Te (bismuth-tellurium), Binary Alloy Phase Diagrams. 1, 1990, 800-801.
42. Mao, C. *et al.* Experimental reinvestigation and thermodynamic description of Bi-Te binary system. *Calphad* **60**, 81–89 (2018).
43. Hatta, S., Obayashi, K., Okuyama, H. & Aruga, T. Metallic conduction through van der Waals interfaces in ultrathin Bi_2Te_3 films. *Sci Rep* **11**, 5742 (2021).
44. Fang, T. *et al.* Complex Band Structures and Lattice Dynamics of Bi_2Te_3 -Based Compounds and Solid Solutions. *Adv. Funct. Mater.* **29**, 1900677 (2019).
45. Youn, S. J. & Freeman, A. J. First-principles electronic structure and its relation to thermoelectric properties of Bi_2Te_3 . *Phys. Rev. B* **63**, 085112 (2001).
46. Vergniory, M. G., Menshchikova, T. V., Ereemeev, S. V. & Chulkov, E. V. Ab initio study of 2DEG at the surface of topological insulator Bi_2Te_3 . *Jetp Lett.* **95**, 213–218 (2012).
47. Krishnamoorthy, H. N. S. *et al.* Infrared dielectric metamaterials from high refractive index chalcogenides. *Nat Commun* **11**, 1692 (2020).
48. Zhang, J.-M. *et al.* Stability, electronic, and magnetic properties of the magnetically doped topological insulators Bi_2Se_3 , Bi_2Te_3 , and Sb_2Te_3 . *Phys. Rev. B* **88**, 235131 (2013).

49. Chen, T. *et al.* Topological transport and atomic tunnelling–clustering dynamics for aged Cu-doped Bi₂Te₃ crystals. *Nat Commun* **5**, 5022 (2014).
50. Park, Y. H. *et al.* Detection and Control of the Effective Magnetic Field in a Ca-Doped Bi₂Se₃ Topological Insulator. *Adv Elect Materials* **8**, 2101075 (2022).
51. Chen, B. *et al.* Intrinsic magnetic topological insulator phases in the Sb doped MnBi₂Te₄ bulks and thin flakes. *Nat Commun* **10**, 4469 (2019).
52. Scipioni, K. L. *et al.* Role of defects in the carrier-tunable topological-insulator (Bi_{1-x}Sb_x)₂Te₃ thin films. *Phys. Rev. B* **97**, 125150 (2018).
53. Chen, C. *et al.* Robustness of topological order and formation of quantum well states in topological insulators exposed to ambient environment. *Proc. Natl. Acad. Sci. U.S.A.* **109**, 3694–3698 (2012).
54. Bianchi, M., Hatch, R. C., Mi, J., Iversen, B. B. & Hofmann, P. Simultaneous Quantization of Bulk Conduction and Valence States through Adsorption of Nonmagnetic Impurities on Bi₂Se₃. *Phys. Rev. Lett.* **107**, 086802 (2011).
55. Hor, Y. S. *et al.* Development of ferromagnetism in the doped topological insulator Bi_{2-x}Mn_xTe₃. *Phys. Rev. B* **81**, 195203 (2010).
56. Tarasenko, R. *et al.* Magnetic and structural properties of Mn-doped Bi₂Se₃ topological insulators. *Physica B: Condensed Matter* **481**, 262–267 (2016).
57. Ye, M. *et al.* Carrier-mediated ferromagnetism in the magnetic topological insulator Cr-doped (Sb,Bi)₂Te₃. *Nat Commun* **6**, 8913 (2015).
58. Kou, X. *et al.* Interplay between Different Magnetisms in Cr-Doped Topological Insulators. *ACS Nano* **7**, 9205–9212 (2013).
59. Sessi, P. *et al.* Dual nature of magnetic dopants and competing trends in topological insulators. *Nat Commun* **7**, 12027 (2016).

60. Arévalo-López, E. P. *et al.* Effect of Fe on Bi₂Te₃: Structure, magnetic properties, and XPS valence band. *Journal of Alloys and Compounds* **899**, 163297 (2022).
61. Leedahl, B. *et al.* Bulk vs. Surface Structure of 3d Metal Impurities in Topological Insulator Bi₂Te₃. *Sci Rep* **7**, 5758 (2017).
62. West, D. *et al.* Identification of magnetic dopants on the surfaces of topological insulators: Experiment and theory for Fe on Bi₂Te₃ (111). *Phys. Rev. B* **85**, 081305 (2012).
63. Weis, M. *et al.* Hot-carrier and optical-phonon ultrafast dynamics in the topological insulator Bi₂Te₃ upon iron deposition on its surface. *Phys. Rev. B* **104**, 245110 (2021).
64. Scholz, M. R. *et al.* Intact Dirac cone of Bi₂Te₃ covered with a monolayer Fe. *Physica Rapid Research Ltrs* **7**, 139–141 (2013).
65. Scholz, M. R. *et al.* Tolerance of Topological Surface States towards Magnetic Moments: Fe on Bi₂Se₃. *Phys. Rev. Lett.* **108**, 256810 (2012).
66. Jo, N. H. *et al.* Tuning of magnetic and transport properties in Bi₂Te₃ by divalent Fe doping. *Phys. Rev. B* **87**, 201105 (2013).
67. Makarova, T. P. *et al.* Impact of Co Atoms on the Electronic Structure of Bi₂Te₃ and MnBi₂Te₄ Topological Insulators. *J. Exp. Theor. Phys.* **134**, 607–614 (2022).
68. Shelford, L. R. *et al.* Electronic structure of Fe and Co magnetic adatoms on Bi₂Te₃ surfaces. *Phys. Rev. B* **86**, 081304 (2012).
69. Scholz, M. R. *et al.* Reversal of the Circular Dichroism in Angle-Resolved Photoemission from Bi₂Te₃. *Phys. Rev. Lett.* **110**, 216801 (2013).
70. Xu, C.-Z. *et al.* Photoemission Circular Dichroism and Spin Polarization of the Topological Surface States in Ultrathin Bi₂Te₃ Films. *Phys. Rev. Lett.* **115**, 016801 (2015).
71. Lüth, H. *Solid Surfaces, Interfaces and Thin Films.* (Springer Berlin Heidelberg, Berlin, Heidelberg, 2010). doi:10.1007/978-3-642-13592-7.

72. <https://www.maths.tcd.ie/~bmurphy/thesis/thesisse2.html>.
73. Hertz, H. Ueber einen Einfluss des ultravioletten Lichtes auf die electriche Entladung. *Annalen der Physik* **267**, 983–1000 (1887).
74. Einstein, Albert. On a heuristic point of view about the creation and conversion of light. *Annalen der Physik*, 132–148 (1905).
75. Nordling, C., Sokolowski, E. & Siegbahn, K. Precision Method for Obtaining Absolute Values of Atomic Binding Energies. *Phys. Rev.* **105**, 1676–1677 (1957).
76. Berglund, C. N. & Spicer, W. E. Photoemission Studies of Copper and Silver: Theory. *Phys. Rev.* **136**, A1030–A1044 (1964).
77. Łukasz Pluciński. Photoelectron Spectroscopy.
78. Seah, M. P. & Dench, W. A. Quantitative electron spectroscopy of surfaces: A standard data base for electron inelastic mean free paths in solids. *Surface & Interface Analysis* **1**, 2–11 (1979).
79. X-ray Absorption Spectroscopy (XAS), <https://sigray.com/x-ray-absorption-spectroscopy/>.
80. Elder, F. R., Gurewitsch, A. M., Langmuir, R. V. & Pollock, H. C. Radiation from Electrons in a Synchrotron. *Phys. Rev.* **71**, 829–830 (1947).
81. *Synchrotron Radiation: Basics, Methods and Applications*. (Springer Berlin Heidelberg, Berlin, Heidelberg, 2015). doi:10.1007/978-3-642-55315-8.
82. Szlachetko, J. *et al.* Correction to: SOLARIS National Synchrotron Radiation Centre in Krakow, Poland. *The European Physical Journal Plus* **138**, 595 (2023).
83. Fadley, C. S. X-ray photoelectron spectroscopy: Progress and perspectives. *Journal of Electron Spectroscopy and Related Phenomena* **178–179**, 2–32 (2010).
84. Shallenberger, J. R., Smyth, C. M., Addou, R. & Wallace, R. M. 2D bismuth telluride analyzed by XPS. *Surface Science Spectra* **26**, 024011 (2019).

85. Krumrain, J. *et al.* MBE growth optimization of topological insulator Bi₂Te₃ films. *Journal of Crystal Growth* **324**, 115–118 (2011).
86. Ereemeev, S. V., Vergniory, M. G., Menshchikova, T. V., Shaposhnikov, A. A. & Chulkov, E. V. The effect of van der Waal's gap expansions on the surface electronic structure of layered topological insulators. *New J. Phys.* **14**, 113030 (2012).
87. Powell, C. J. Practical guide for inelastic mean free paths, effective attenuation lengths, mean escape depths, and information depths in x-ray photoelectron spectroscopy. *Journal of Vacuum Science & Technology A: Vacuum, Surfaces, and Films* **38**, 023209 (2020).
88. Shinotsuka, H., Tanuma, S., Powell, C. J. & Penn, D. R. Calculations of electron inelastic mean free paths. X. Data for 41 elemental solids over the 50 eV to 200 keV range with the relativistic full Penn algorithm. *Surface & Interface Analysis* **47**, 871–888 (2015).
89. Wang, G. *et al.* Topological Insulator Thin Films of Bi₂Te₃ with Controlled Electronic Structure. *Advanced Materials* **23**, 2929–2932 (2011).
90. Plucinski, L. *et al.* Robust surface electronic properties of topological insulators: Bi₂Te₃ films grown by molecular beam epitaxy. *Appl. Phys. Lett.* **98**, 222503 (2011).
91. Chuang, P.-Y. *et al.* Anti-site defect effect on the electronic structure of a Bi₂Te₃ topological insulator. *RSC Adv.* **8**, 423–428 (2018).
92. Xu, S.-Y. *et al.* Realization of an isolated Dirac node and strongly modulated Spin Texture in the topological insulator Bi₂Te₃. (2011).
93. Frantzeskakis, E. *et al.* Trigger of the Ubiquitous Surface Band Bending in 3D Topological Insulators. *Phys. Rev. X* **7**, 041041 (2017).
94. Qu, Q. *et al.* Expediting Hydrogen Evolution through Topological Surface States on Bi₂Te₃. *ACS Catal.* **10**, 2656–2666 (2020).
95. Chen, Z. *et al.* Topology-Engineered Orbital Hall Effect in Two-Dimensional Ferromagnets. *Nano Lett.* [acs.nanolett.3c05129](https://doi.org/10.1021/acs.nanolett.3c05129) (2024) doi:10.1021/acs.nanolett.3c05129.

96. Sánchez-Barriga, J. *et al.* Photoemission of Bi₂Se₃ with Circularly Polarized Light: Probe of Spin Polarization or Means for Spin Manipulation? *Phys. Rev. X* **4**, 011046 (2014).
97. Li, J. *et al.* Intrinsic magnetic topological insulators in van der Waals layered MnBi₂Te₄-family materials. *Sci. Adv.* **5**, eaaw5685 (2019).
98. Chang, C.-Z. & Li, M. Quantum anomalous Hall effect in time-reversal-symmetry breaking topological insulators. *J. Phys.: Condens. Matter* **28**, 123002 (2016).
99. Ding, L. *et al.* Crystal and magnetic structures of magnetic topological insulators MnBi₂Te₄ and MnBi₄Te₇. *Phys. Rev. B* **101**, 020412 (2020).
100. Xu, S.-Y. *et al.* Hedgehog spin texture and Berry's phase tuning in a magnetic topological insulator. *Nature Phys* **8**, 616–622 (2012).
101. Wray, L. A. *et al.* A topological insulator surface under strong Coulomb, magnetic and disorder perturbations. *Nature Phys* **7**, 32–37 (2011).
102. Chen, Y. L. *et al.* Massive Dirac Fermion on the Surface of a Magnetically Doped Topological Insulator. *Science* **329**, 659–662 (2010).
103. Bahramy, M. S. *et al.* Emergent quantum confinement at topological insulator surfaces. *Nat Commun* **3**, 1159 (2012).
104. Schlenk, T. *et al.* Controllable Magnetic Doping of the Surface State of a Topological Insulator. *Phys. Rev. Lett.* **110**, 126804 (2013).
105. Arnold, F. *et al.* Electronic structure of Fe_{1.08}Te bulk crystals and epitaxial FeTe thin films on Bi₂Te₃. *J. Phys.: Condens. Matter* **30**, 065502 (2018).
106. Shikin, A. M. *et al.* Dirac gap opening and Dirac-fermion-mediated magnetic coupling in antiferromagnetic Gd-doped topological insulators and their manipulation by synchrotron radiation. *Sci Rep* **9**, 4813 (2019).

107. Kim, H.-J. *et al.* Topological Phase Transitions Driven by Magnetic Phase Transitions in $\text{Fe}_x\text{Bi}_{2-x}\text{Te}_3$ ($0 \leq x \leq 0.1$) Single Crystals. *Phys. Rev. Lett.* **110**, 136601 (2013).
108. Yeh, J. J. & Lindau, I. Atomic subshell photoionization cross sections and asymmetry parameters: $1 \leq Z \leq 103$. *Atomic Data and Nuclear Data Tables* **32**, 1–155 (1985).
109. <https://vuo.elettra.eu/services/elements/WebElements.html>.
110. Fano, U. & Cooper, J. W. Spectral Distribution of Atomic Oscillator Strengths. *Rev. Mod. Phys.* **40**, 441–507 (1968).
111. Scofield, J. H. K - and L -shell ionization of atoms by relativistic electrons. *Phys. Rev. A* **18**, 963–970 (1978).
112. Sánchez-Barriga, J. *et al.* Observation of hidden atomic order at the interface between Fe and topological insulator Bi_2Te_3 . *Phys. Chem. Chem. Phys.* **19**, 30520–30532 (2017).
113. Tkáč, V. *et al.* Multiphase superconductivity at the interface between ultrathin FeTe islands and Bi_2Te_3 . *npj 2D Mater Appl* **8**, 52 (2024).
114. Walsh, L. A. *et al.* Interface Chemistry of Contact Metals and Ferromagnets on the Topological Insulator Bi_2Se_3 . *J. Phys. Chem. C* **121**, 23551–23563 (2017).
115. Telesca, D., Nie, Y., Budnick, J. I., Wells, B. O. & Sinkovic, B. Impact of valence states on the superconductivity of iron telluride and iron selenide films with incorporated oxygen. *Phys. Rev. B* **85**, 214517 (2012).
116. Bianchi, M. *et al.* Coexistence of the topological state and a two-dimensional electron gas on the surface of Bi_2Se_3 . *Nat Commun* **1**, 128 (2010).
117. Bianchi, M. *et al.* Robust Surface Doping of Bi_2Se_3 by Rubidium Intercalation. *ACS Nano* **6**, 7009–7015 (2012).
118. Pilidi, A., Speliotis, Th. & Litsardakis, G. Structural and magnetotransport characterization of magnetron sputtered co-doped Bi_2Te_3 thin films. *Journal of Magnetism and Magnetic Materials* **511**, 166971 (2020).

119. Irfan, B. & Chatterjee, R. Magneto-transport and Kondo effect in cobalt doped Bi₂Se₃ topological insulators. *Applied Physics Letters* **107**, 173108 (2015).
120. Li, C. H. *et al.* Electrical detection of charge-current-induced spin polarization due to spin-momentum locking in Bi₂Se₃. *Nature Nanotech* **9**, 218–224 (2014).
121. Ye, M. *et al.* Quasiparticle interference on the surface of Bi₂Se₃ induced by cobalt adatom in the absence of ferromagnetic ordering. *Phys. Rev. B* **85**, 205317 (2012).
122. Mandale, A. B., Badrinarayanan, S., Date, S. K. & Sinha, A. P. B. Photoelectron-spectroscopic study of nickel, manganese and cobalt selenides. *Journal of Electron Spectroscopy and Related Phenomena* **33**, 61–72 (1984).